MARMARA UNIVERSITY

INSTITUTE FOR GRADUATE STUDIES
IN PURE AND APPLIED SCIENCES

DEVELOPMENT OF A SENSORLESS HAPTIC TELEOPERATION SYSTEM FOR ROBOTIC MINIMALLY INVASIVE SURGERY

NURAL YILMAZ

MASTER THESIS

Department of Mechanical Engineering

Thesis Supervisor

Assist. Prof. Dr. Uğur TÜMERDEM

ISTANBUL, 2019

MARMARA UNIVERSITY
INSTITUTE FOR GRADUATE STUDIES
IN PURE AND APPLIED SCIENCES

DEVELOPMENT OF A SENSORLESS HAPTIC TELEOPERATION SYSTEM FOR ROBOTIC MINIMALLY INVASIVE SURGERY

NURAL YILMAZ

(524616017)

MASTER THESIS

Department of Mechanical Engineering

Thesis Supervisor

Assist. Prof. Dr. Uğur TÜMERDEM

ISTANBUL, 2019

MARMARA UNIVERSITY
INSTITUTE FOR GRADUATE STUDIES
IN PURE AND APPLIED SCIENCES

Nural YILMAZ, a Master of Science student of Marmara University Institute for Graduate Studies in Pure and Applied Sciences, defended her thesis entitled "Development of a Sensorless Haptic Teleoperation System for Robotic Minimally Invasive Surgery", on Jan 09, 2019 and has been found to be satisfactory by the jury members.

Jury Members

Assist.Prof. Dr. Uğur TUMERDEM (Advisor)
Marmara University .... (SIGN)..............

Assist.Prof. Dr. Sina KUSEYRİ (Jury Member)
Marmara University .... (SIGN)..............

Assist.Prof. Dr. Berke GÜR (Jury Member)
Bahçeşehir University .... (SIGN)..............

APPROVAL

Marmara University Institute for Graduate Studies in Pure and Applied Sciences Executive Committee approves that Nural YILMAZ be granted the degree of Master of Science in Department of Mechanical Engineering, Mechanical Engineering Program on 16.01.2019. (Resolution no: 2019/ 02-02

Director of the Institute
Prof. Dr. Bülent Ekici

ACKNOWLEDGEMENT

First of all, I would like to thank my family for supporting me at all times.

I would also like to thank especially my supervisor, Assist. Prof. Dr. Uğur Tümerdem for his encouragement, continuous guidance and valuable ideas. Further, I would like to thank my colleague, Merve Bazman for her timely help and motivating me during this thesis study.

Some chapters in this thesis were supported by The Scientific and Technological Research Council of Turkey and also, I would like to thank the team from Bahçeşehir University Robotics Lab with whom we worked together in the project.

Nural YILMAZ

Istanbul, January 2019

TABLE OF CONTENTS

ACKNOWLEDGEMENT i

ÖZET v

ABSTRACT vi

SYMBOLS vii

ABBREVATIONS x

LIST OF FIGURES xi

LIST OF TABLES xiv

1. INTRODUCTION 1
   - 1.1. Literature Survey 1
   - 1.2. Objectives 7

2. A 4-DOF SURGICAL FORCEPS MECHANISM 9
   - 2.1. System Overview 9
     - 2.1.1. 3-DOF Parallel Wrist Mechanism 10
     - 2.1.2. 1-DOF Gripper 11
   - 2.2. Position Kinematic Analysis 12
     - 2.2.1. Kinematic Analysis of the 3-DOF Parallel Wrist Mechanism 12
     - 2.2.2. Kinematic Analysis of the 1-DOF Gripper 19
   - 2.3. Velocity Kinematic Analysis 21

3. CONTROL SYSTEM OF A 4-DOF FORCEPS MECHANISM 22
   - 3.1. PID Controller with Disturbance Observer 23
     - 3.1.1. Conventional PID Controller 23
     - 3.1.2. Disturbance Observer 24
   - 3.2. Sliding Mode Control 27
   - 3.3. Comparison of DOBS based PID Controller and SMC with Integral Term 30

4. EXTERNAL FORCE/TORQUE ESTIMATION METHOD 32

4.1. Inverse Dynamics Calculation by Neural Networks...32

4.2. Reaction Force Observer 33

4.3. Force Estimation Experiments and Results 35

4.3.1. Free Motion 37

4.3.2. Contact Force in β axis 38

4.3.3. Validation using Force Sensor... 39

4.3.4. Tumor Detection... 40

5. FORCE ESTIMATION ALGORITHM ON A 7-DOF SURGICAL ROBOT 42

5.1. The Surgical Robot System Overview...42

5.1.1. Slave Side 42

5.1.2. Master Side 43

5.1.3. Communication System.. 44

5.2. Force Estimation Process...45

5.3. Force Estimation Algorithm 46

5.4. Force Estimation Experiments and Results 50

5.4.1. Validation of Forces and Torques in –x, –y, –z axes 50

5.4.2. Palpation Experiment inside the Phantom... 54

5.4.3. Gripping Axis 55

6. BILATERAL TELEOPERATION SYSTEMS FOR ROBOTIC SURGERY 56

6.1. Phantom Omni 56

6.1.1. Position and Velocity Kinematics 57

6.1.2. Force Estimation Algorithms 59

6.2. 4-Channel Bilateral Teleoperation System with NN based RFOB...................65

6.3. Experiments and Results...67

6.3.1. Validation using Force Sensor ... 68
6.3.2. Comparison of CTM and NNRFOB ... 70
7. CONCLUSIONS ... 73
7.1. Accomplishments and Conclusions ... 73
7.2. Future Work ... 74
REFERENCES ... 75

ÖZET

ROBOTİK MİNİMAL İNVAZİF CERRAHİ İÇİN SENSÖRSÜZ HAPTİK TELEOPERASYON SİSTEMİ GELİŞTİRİLMESİ

Minimal invazif cerrahi, hasta vücuduna küçük insizyonlardan girilerek dışarıdan kontrol edilebilen özel enstrümanlarla operasyon yapılmasıdır. Robotik minimal invazif cerrahi ise cerrahlara operasyon sırasında daha fazla hassasiyet, esneklik ve kontrol kazandırmaktadır. Bu sayede, ameliyatlar daha düşük enfeksiyon riski ve hızlı taburcu imkanı ile daha kolay bir şekilde gerçekleştirilebilmektedir. Ancak, günümüzde kullanılan cerrahi robotlarda operasyonlarda transmisyon sisteminden kaynaklı problemler yaşanmakta ve vücut içerisinde dokunma hissi cerraha iletilememektedir.

Bahsedilen problemi çözmek amacıyla Türkiye Bilimsel ve Teknolojik Araştırma Kurumu tarafından desteklenen bir proje kapsamında 1.5-2cm'lik bir delikten geçebilen, insan bileği hareketlerini yapabilen ve vücut dışarısından rijit çubuklarla kontrol edilen 3-serbestlik-dereceli paralel bilek mekanizması tasarlanmıştır. Mekanizmanın ucuna mikro motor bağlanmasıyla makas açma-kapama hareketi ile birlikte vücut içerisinde 4-serbestlik-derecesinde bir robotik forseps elde edilmiştir. Rijit transmisyon kullanıldığından forsepse etki eden kuvvetler, tez kapsamında geliştirilen kestirim metodu ile motorlarda oluşan kuvvetlerden hesaplanabilmektedir. Ayrıca, bu forsepsin 7-eksenli robot koluna monte edilmesiyle hasta içerisinde x-y-z yönlerinde yer değiştirme, pitch-yaw-roll eksenlerinde dönüş ve tutucu ekseninde açma-kapama olmak üzere 7-serbestlik-derecesine ulaşılmaktadır.

Bu tezde dinamik denklemleri bilinmeyen ve kuvvet sensörü bulunmayan herhangi bir robota dıştan etki eden kuvvet-torkların kestirimini sağlayan bir metot geliştirilmiştir. Bu metot ile forseps mekanizmasında kuvvet kestirimi ve tümör tespiti deneyleri yapılmıştır. Daha sonra, bu metot temel alınarak 7-serbestlik-dereceli cerrahi robotun kuvvet-tork ilişkileri elde edilip kuvvet kestirimi çalışmaları yapılmış ve sonuçlar her eksende sırasıyla doğrulanmıştır.

Son olarak geliştirilen kestirim metodu kullanılarak, ticari Phantom Omni robotları için teleoperasyon mimarileri tasarlanmıştır. Teleoperasyon sırasında robotlara etki eden kuvvetler, kuvvet sensörü kullanılarak doğrulanmıştır ve hassas sonuçlar ile metodun işlevselliği de kanıtlanmıştır.

ABSTRACT

DEVELOPMENT OF A SENSORLESS HAPTIC TELEOPERATION SYSTEM FOR ROBOTIC MINIMALLY INVASIVE SURGERY

Minimally invasive surgery is a medical procedure where the surgeon operates on a patient with special instruments that enter the body through small incisions. Compared with minimally invasive surgery, robotic minimally invasive surgery gives surgeons flexibility and more accurate control during operations. However, the surgical robots used today have problems due to their transmission and control systems and cannot transmit the sense of touch to the surgeon within the body.

Within the scope of a project supported by The Scientific and Technological Research Council of Turkey, a 3-degrees-of-freedom parallel wrist mechanism that is capable of mirroring human wrist motions, and that can pass through incisions of 1.5cm has been designed to solve the stated problem. By mounting a linear motor actuated gripper on the wrist, the resulting forceps has 4-degrees-of-freedom inside the body. Due to the use of rigid transmissions, the forces acting on the forceps can be calculated from the joint motors by an estimation method developed within the scope of this thesis. By mounting the mentioned forceps on a 7-axis robotic arm, 7-degree-of-freedom motion in the body with translation in x-y-z directions, rotation in pitch-yaw-roll axes and gripping is achieved.

The main contribution of this thesis is a method for force sensorless external force-torque estimation that can be implemented on any robot whose dynamic equations are not known. Force estimation and tumor detection experiments have been carried out on the developed robotic forceps using the proposed method. Then, Cartesian Space-Joint Space force transformations of the surgical robot were derived and force estimation studies were carried out on the 7-degrees-of-freedom system and the results were verified on each axis, separately.

Finally, teleoperation architectures have been designed for the commercial robot Phantom Omni using the proposed method. The forces acting on the robots during teleoperation were validated with a force sensor, and the accuracy of the proposed method has been demonstrated.

SYMBOLS

Symbol		Quantity	Unit
$L_i\left(i=1:3\right)$	:	Motor displacement of the wrist	m
α	:	Pitch axis (alpha) of the wrist	deg
β	:	Yaw axis (beta) of the wrist	deg
r	:	Thrust axis of the wrist	mm
$\theta_i\left(i=1:3\right)$	:	Link angles of the wrist	deg
$\hat{n}_P$	:	Unit vector of the top platform of the wrist	
s_i	:	sine	
c_i	:	cosine	
B	:	Center point of the base platform of the wrist	
P	:	Center point of the top platform of the wrist	
$\hat{n}_B$	:	Base platform unit vector	
${}^{B}_{P}T$	:	Transformation matrix from base to top platform	
s_d	:	Desired spindle drive position	mm
θ_g	:	Gripper angle	deg
J_1	:	Jacobian for the wrist part of the forceps	
J_2	:	Jacobian for the motor part of the forceps	
J	:	Total Jacobian of the forceps	
K_p	:	P gain of PID controller	
K_i	:	I gain of PID controller	
K_d	:	D gain of PID controller	
e	:	Position error	
$s\left(t\right)$	:	Switching function	
λ	:	Lambda gain for velocity error	
q^{ref}	:	Reference position	m, deg, rad
q	:	Actual position	
t	:	Time	s
u	:	Control input	Volt, N
τ_{dis}	:	Disturbance torque	

g_{dis}	:	Cut-off frequency in DOBS	rad/s
I^{ref}	:	Reference current	A
K_{tn}	:	Nominal force/torque constant	
M_n	:	Nominal mass	kg
$\dot{q}$	:	Joint velocity	m/s, deg/s
$\hat{\tau}_{dis}$	:	Disturbance torque estimate	Nm
$M(q)$	:	Mass matrix	
$C(q,\dot{q})$	:	Coriolis and centrifugal force vector	
$G(q)$	:	Gravity vector	
τ_{ext}	:	External torque	Nm
τ	:	Internal torque	Nm
τ_{int}	:	Interactive torque	Nm
$f(\dot{q})$	:	Friction forces	
g_{reac}	:	Cut-off frequency in RFOB	rad/s
F_r	:	Force in thrust axis	N
ω	:	Angular velocity	rad/s, deg/s
v	:	Linear velocity	m/s
R	:	Rotation matrix	
τ_{ϕ}	:	Torque in phi axis	Nm
τ_{ψ}	:	Torque in psi axis	Nm
F_{ρ}	:	Force in rho axis	N
τ_{γ}	:	Torque in gamma axis	Nm
τ_{α}	:	Torque in alpha axis	Nm
τ_{β}	:	Torque in alpha beta	Nm
IE	:	IIWA end-effector	
IB	:	IIWA base	
m	:	Master	
s	:	Slave	
$\hat{\tau}_m^{ext}$	:	External torque estimate of the master robot	Nm

$\hat{\tau}_s^{ext}$	:	External torque estimate of the slave robot	Nm
$I(q)$	:	Inertia matrix	
q_m, q_s	:	Joint-space positions of master and slave robots	deg, rad
$C_i\ (i = 1:6)$	:	Position controllers	
C_m, C_s	:	Self-position controller of master and slave robots	
C_f	:	Force controller	

ABBREVATIONS

CS	**:**	Cartesian Space
DAQ	**:**	Data Acquisition
DH	**:**	Denavit-Hartenberg
DOBS	**:**	Disturbance Force Observer
DOF	**:**	Degree-of-freedom
EAOB	**:**	Extended Active Observer
FRI	**:**	Fast Robot Interface
FTS	**:**	Force-Torque Sensors
JS	**:**	Joint Space
LM	**:**	Levenberg-Marquard
MIS	**:**	Minimally Invasive Surgery
NN	**:**	Neural Network
PID	**:**	Proportional-Integral-Derivative
PRR	**:**	Prismatic-Revolute-Revolute
RCM	**:**	Remote Center of Motion
RFOB	**:**	Reaction Force Observer
RMS	**:**	Root Mean Square
RMSE	**:**	Root Mean Square Error
RSR	**:**	Revolute-Spherical-Revolute
SMC	**:**	Sliding Mode Controller
SMCSPO	**:**	Sliding Mode Controller with Sliding Perturbation Observer
SPO	**:**	Sliding Perturbation Observer
UDP	**:**	User Datagram Protocol
USB	**:**	Universal Serial Bus

LIST OF FIGURES

Figure 1.1. General bilateral teleoperation schema 1

Figure 1.2. Miniaturized force sensors 2

Figure 1.3. MiroSurge surgical robot system 2

Figure 1.4. 4-DOF sensorized instrument including Raven 2 adapter 3

Figure 1.5. Davinci EndoWrist instrument... 4

Figure 1.6. A 3-DOF surgical grasper with cable-pulley system prototype.................... 5

Figure 1.7. Davinci EndoWrist instrument and its motion axes...................................... 6

Figure 1.8. Bilateral teleoperation of 3-DOF Sensible Phantom Omni........................... 7

Figure 2.1. 4-DOF parallel forceps wrist mechanism.. 9

Figure 2.2. Forceps mechanisms with and without a gripper 10

Figure 2.3. Schematic representation of serial chains of 3-DOF wrist (a) 3-RSR (b) 3-PRR.. 10

Figure 2.4. Degrees of freedom of the wrist mechanism (a) Comparison with the human wrist (b) Thrust motion... 11

Figure 2.5. Gripper Mechanism and transmission system.. 11

Figure 2.6. 3-DOF wrist mechanism kinematic analysis steps..................................... 12

Figure 2.7. Representation of parameters used in geometric solution of motor parts (a) Detailed representation (b) General parameters 13

Figure 2.8. The kinematic structure diagrams of the wrist 15

Figure 2.9. The parameters of the wrist (a) General representation (b) DH parameters 17

Figure 2.10. Parameters used in gripper kinematic analysis 19

Figure 3.1. A general closed-loop control system 22

Figure 3.2. A general schema of a control system of the wrist mechanism 22

Figure 3.3. Disturbance observer.. 24

Figure 3.4. Joint-space position control diagram using PD controller with DOBS 25

Figure 3.5. Position control results of 3-DOF wrist excluding gripper using PID and DOBS in (a) Joint space (b) Cartesian space.. 26

Figure 3.6. Position control results of 4-DOF wrist including gripper using PID and DOBS in (a) Joint-space (b) Cartesian -space 26

Figure 3.7. Position control result of 1-DOF motor with SMC using (a) sgn function (b) sat function 28

Figure 3.8. Position control result of 3-DOF wrist with SMC using sat function in (a) Joint-space (b) Cartesian-space 28

Figure 3.9. SMC diagram with relay function 29

Figure 3.10. Position control result of 4-DOF wrist mechanism using SMC with integral term in (a) Joint-space (b) Cartesian-space 29

Figure 3.11. Comparison of PID and SMC controllers sending the same position reference to 4-DOF wrist (a) Experiment setup (b) alpha axis (c) beta axis (c) Thrust axis 31

Figure 4.1. Neural Network model 32

Figure 4.2. Disturbances related to states 33

Figure 4.3. Disturbance observer and reaction force observer model including Neural Network 34

Figure 4.4. The sensorless control architecture of 3-DOF wrist force estimation......... 35

Figure 4.5. Free motion experiment (a) Experiment setup (b) Comparison of DOBS, NN and external forces in JS (c) End-effector force/torques in CS (d) End-effector position/orientation in CS 37

Figure 4.6. Contact force experiment in beta axis (a) Experiment setup (b) Comparison of DOBS, NN and external forces in JS (c) End-effector force/torques in CS (d) End-effector position/orientation in CS 38

Figure 4.7. Validation using force sensor (a) Experiment setup (b) Comparison of DOBS, NN and external forces in JS (c) End-effector force/torques in CS (d) End-effector position/orientation in CS 39

Figure 4.8. Tumor detection experiment setup 40

Figure 4.9. Experiment result of the stiffness determination in thrust axis 40

Figure 5.1. 7-DOF surgical robot system (a) Overview of the system (b) Inside the phantom 42

Figure 5.2. Elements of the slave manipulator (a,b) 4-DOF forceps mechanism (c) IIWA manipulator 43

Figure 5.3. Elements of the master manipulator (a) Handgrip mechanism (b) 7-DOF master manipulator 44

Figure 5.4. Control system architecture among forceps, handgrip, Omega.6, IIWA and the force sensor interfaces 45

Figure 5.5. Control system of the surgical robot system 46

Figure 5.6. Frame assignment of the 7-DOF surgical robot 47

Figure 5.7. Experiment setup for force validations (a) Fx (b) Fy (c) Fz 51

Figure 5.8. Experiment setup for torque validations (a) Nx (b) Ny (c) Nz 51

Figure 5.9. Force/torque validation results (a) Fx (b) Fy (c) Fz (d) Nx (e) Ny (d) Nz.. 53

Figure 5.10. Force/torque validation results (a) Translational Position (b) Angular Position (c) Forces in x, y, z axes (d) Torques in x, y, z axes 54

Figure 5.11. Palpation experiment setup in gripping axis 55

Figure 5.12. Gripping axis (a) Position response (b) Force response 55

Figure 6.1. Bilateral teleoperation system for a surgical robot..................................... 56

Figure 6.2. Phantom Omni robot (a) General view (b) Representation of joints 57

Figure 6.3. Representation of DH parameters of the first 3-DOF of Phantom Omni ... 57

Figure 6.4. Neural Network model for master and slave robots................................... 60

Figure 6.5. Disturbance force related to states for each joint of (a) master robot (b) slave robot.. 60

Figure 6.6. Performance results of NN training (a) mean square error (b) Error histogram 61

Figure 6.7. Linear regression results of NN training.. 62

Figure 6.8. A model-based manipulator-control system 65

Figure 6.9. 4 channel teleoperation diagram based on Lawrence Architecture for Phantom Omni robots... 66

Figure 6.10. 4-channel teleoperation system between 2 haptic devices........................ 67

Figure 6.11. Bilateral teleoperation result in –x axis (a) Experiment setup (b) Comparison of estimated force and force sensor (c) Position tracking in CS (d) Force reflection in CS 68

Figure 6.12. Bilateral teleoperation result in –y axis (a) Experiment setup (b) Comparison of estimated force and force sensor (c) Position tracking in CS (d) Force reflection in CS 69

Figure 6.13. Bilateral teleoperation result in –z axis (a) Experiment setup (b) Comparison of estimated force and force sensor (c) Position tracking in CS (d) Force reflection in CS 70

Figure 6.14. Experiment setup to compare RFOB and CTM....................................... 71

Figure 6.15. Position response in CS during free-motion (a) CTM (b) NNRFOB 71

Figure 6.16. JS torque and CS force estimations (a,c) CTM (b,d) NNRFOB............... 72

LIST OF TABLES

Table 2.1. DH Parameters of the 3-DOF Wrist 16

Table 3.1. Comparison of RMS errors of position control results for 3-DOF and 4-DOF wrist mechanisms 26

Table 3.2. Comparison of RMS errors of position control results w/o integral term in Joint-space and Cartesian-space 30

Table 3.3. Comparison of RMS errors in CS space using PID and SMC controllers ... 30

Table 4.1. Parameters used in control system... 36

Table 4.2. RMS error values in force data 41

Table 5.1. DH parameters of the 6-DOF Virtual Trocar Method 48

Table 5.2. Trocar robot joint variables during experiments.. 52

Table 5.3. RMS error values in force/torque validation experiments............................ 52

Table 6.1. DH parameters of the first 3-DOF of Phantom Omni 58

Table 6.2. Inertia and cut-off frequency values of each joint 59

Table 6.3. Position and force controllers for each joint of Phantom Omni 67

Table 6.4. RMS error values in CS as a result of validation with a force sensor 70

Table 6.5. Comparison of RMS errors in experiments with CTM and NNRFOB 72

1. INTRODUCTION

1.1. Literature Survey

Minimally invasive surgery (MIS) is a medical procedure where the surgeon operates on the patient by entering the body through small incisions. Differently from open surgery, MIS is conducted by using special tools, such as cameras and laparoscopic forceps instruments which are controlled by the surgeon via teleoperation and MIS can also offer many benefits for both surgeon and patient.

In a haptic robotic-assisted MIS system, the surgeon ideally controls a master manipulator (the haptic device) to drive slave manipulator (a robotic forceps) and can feel the reaction from the patient body through the teleoperation system which enables the transmission and reception of position and force signals based on the principle of action and reaction. This procedure is also known as bilateral teleoperation and its general structure can be seen in Fig.1.1. However, current minimally invasive surgical robot systems are not bilaterally teleoperated and do not provide force feedback. As a result, the surgeons cannot feel the reaction forces inside the body, and lose their sense of touch. Force feedback, that improves surgical performance plays an important role in MIS because it provides safe control actions to surgeons during operations, such as manipulating tissue, tying knots, suturing and so on [1]. In literature, there are a lot of force sensing techniques to measure or estimate external forces acting on a robotic manipulator.

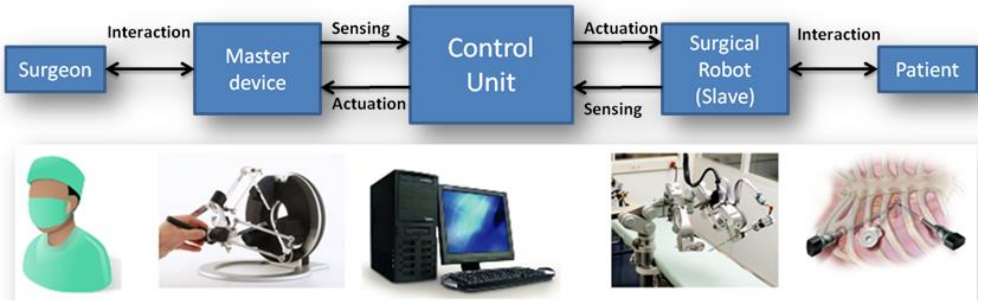

Figure 1.1. General bilateral teleoperation schema

To provide haptic feedback, researchers have worked on a variety of force sensors on surgical robotic systems to measure interaction forces between the tool and tissue (Fig.1.2). Some sensors which have strain gauges of piezoelectric materials are attached to jaws of the tool. Other sensors are located at the distal end of the shaft to measure manipulation forces at the tip and these sensors also use strain gauges [2-3]. However, the attachment of force sensors leads to other problems in minimally invasive surgery, since sensors bring about size, geometry, cost, biocompatibility, noisy outputs and sterilization issues [4-8]. For this reason, using force sensors is not practical to measure forces acting on the tool [3].

Figure 1.2. Miniaturized force sensors

Force-torque sensors (FTS) are used to measure tissue manipulation forces in only one current robotic surgery system, which is named MiroSurge as seen in Fig.1.3 and can do force measurement in 7 axes [9]. This system is not commercially available. It combines a 6-DOF FTS with a 2-DOF cable driven joint. The force sensor has an advantage of being miniaturized. Gripping forces are measured independently of the manipulation forces by a second uniaxial sensor. Nevertheless, this system is a very costly setup and is not an ideal force feedback system due to the problems of cable pulley transmission mechanism, such as friction, slip, and slack, and the limited workspace.

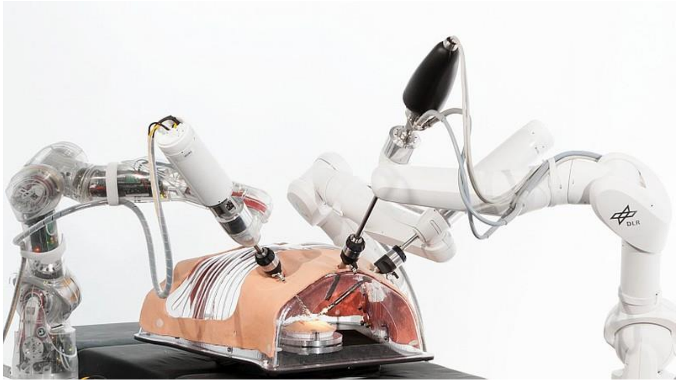

Figure 1.3. MiroSurge surgical robot system

Hannaford et al. have proposed 4-DOF surgical forceps with a special capacitive force sensor attached to inside the jaws of the gripper as shown in Fig.1.4. This forceps is compatible with the cable driven Raven 2 surgical system which can perform force sensing in x, y, z and gripping axes [10]. But forces applied on the other parts of the gripper cannot be measured with this technique.

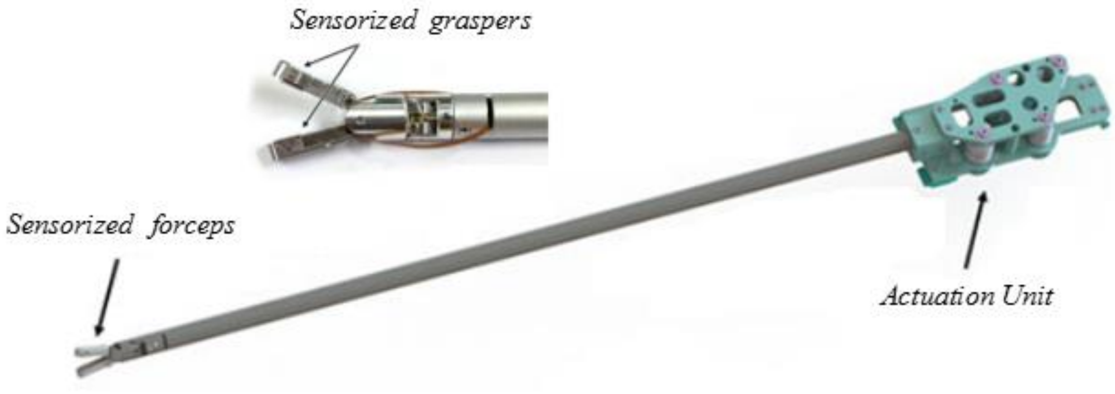

Figure 1.4. 4-DOF sensorized instrument including Raven 2 adapter

As an alternative method which provides external force estimation in remotely teleoperated MIS systems, force observers or disturbance observers have been implemented in teleoperation systems [11]. Lee et al. [12] who worked on a 4-DOF surgical robot (Intuitive EndoWrist Instrument as can be seen in Fig.1.5) consisting of cable-pulley mechanisms developed sliding mode controller with sliding perturbation observer (SMCSPO) which is a robust control algorithm to estimate external forces. In this method, they used only the state equations without any sensor. The main idea of this method was that perturbation is a combination of system uncertainties, nonlinearities and disturbances and these effects can be eliminated by using sliding perturbation observer (SPO). They assumed that perturbation value is close to the estimated reaction force if the nonlinearity or modeling parameter error of a system is small and they used the estimated reaction force as a feedback. In this process, the haptic function was realized by current control of DC motor installed in the master system. However, they performed an experiment on only gripper axis. Also, the estimation method does not distinguish between dynamic robot coupling and external forces in case the assumption is invalid. For this reason, the generalized evaluation of haptic function was insufficient.

Tadano et al. [13] developed 4-DOF robotic forceps which can provide force feedback to the surgeon without using force sensors. In design, they used pneumatic cylinders as the actuators and they estimated external force from driving force and the impedance. A bilateral control system was created by using a neural network to obtain inverse dynamics which was used as a feedforward controller and they estimated external force from the differential pressure of the cylinders by using a disturbance observer. In the experiment results, large errors can be seen in force experiments due to loss of power transmission which was caused by pneumatic cylinders and time delays. Besides, they showed only the experiment results of force estimation in bending axes and it is unknown how much accurate force estimations were in other axes.

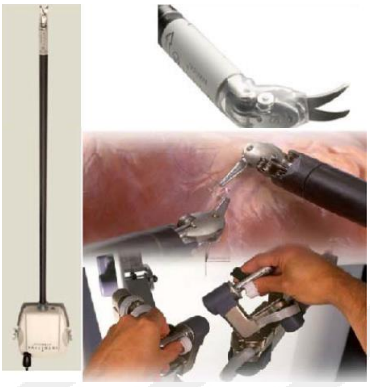

Figure 1.5. Davinci EndoWrist instrument

Hongqiang Sang et al. [1] proposed an external force estimation and implementation method based on dynamics of the system and motor currents and they implemented this method on the 7-DOF da Vinci Research Kit (Patient Side Manipulator). They derived the dynamic model for 6-DOF of the manipulator except gripper by using screw theory and Lagrange dynamics approach. Then, they obtained external torques acting on the motors of the surgical instrument by utilizing its dynamics and motor currents and estimated the external force exerted on the end effector of the surgical instrument in x-, y-, z- axes by using the Jacobian matrix. Furthermore, they also used sliding mode control with a sliding perturbation observer to separate the uncertain and nonlinear dynamic effects due to the complexity of the tendon-driven mechanism. As a result of comparison of the proposed method and SMCSPO method, proposed method predicted joint torques and external forces accurately in x-, y-, z- axes. However, experiment results were presented for only 3 axes of manipulator and how much accuracy force was estimated with in orientation axes and gripping axis is not known.

Zhao et al. [14] have proposed a decoupled cable actuated wrist design and investigated a method to estimate the interaction forces between tool and tissue by using motor current. Jeong, Li, and Tholey had done related work for estimating force with supplied motor current, but the system shows low fidelity in periodic motions and accuracy of this approach was not acceptable [15-17]. For this reason, they decoupled of motions of 3-DOF surgical grasper which had the cable-pulley system and then estimated the interaction forces separately from the respective driving motor’s current. They assumed that the dynamics effects were ignored and this caused the estimation error. They performed stiffness differentiation on 3 different materials and tumor detection experiments. Although stiffness difference was identified, the results were so noisy and had large error due to having no observer for compensating dynamic effects.

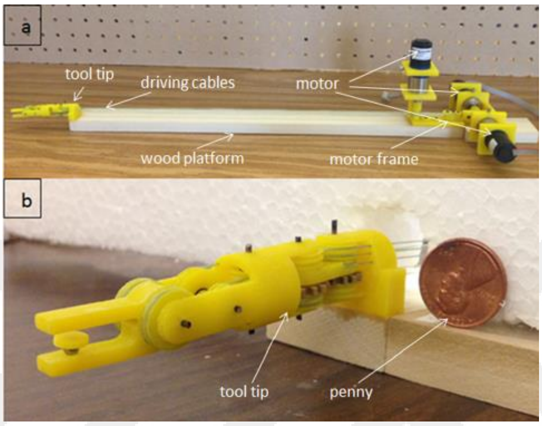

Figure 1.6. A 3-DOF surgical grasper with cable-pulley system prototype

Bolgar et al. [18] estimated force feedback through the actuators which required the dynamic of the tool and worked on 4-DOF EndoWrist which is a surgical tool for the da Vinci robot. It was difficult to derive the dynamic model precisely due to the nonlinearities of the EndoWrist which includes cable-pulley mechanisms. For this reason, they utilized black-box identification algorithm for obtaining the general model structure. Obtained model underestimated the applied force, and then, they implemented steady-state Kalman filter by using position error and velocity measurements to correct the force estimate. Nevertheless, simulation results showed that Kalman filter did not improve the system. Hannaford et al. [19] have reported that loss or variance of cable tensions is a major obstacle in force estimation and have proposed a cable tension estimator together with an external force estimator on a single axis of the Raven 2 robot.

On the other hand, there exists some important research about obtaining force feedback from non-surgical industrial robots. Murakami et al. [20] implemented disturbance force observer (DOBS) which was proposed by Ohnishi et al. [21] and reaction force observer (RFOB) on 3-DOF manipulator. The main idea is that a DOB estimates external disturbances and system uncertainties and then, RFOB was used to estimate reaction torque acting on each joint by subtracting interactive and friction torques from DOB's output [22]. To find the dynamics of the manipulator, they used Euler-Lagrange equations. Furthermore, they showed that the estimated torques in the workspace can be found by the inverse transposed Jacobian matrix of the multi-DOF manipulator.

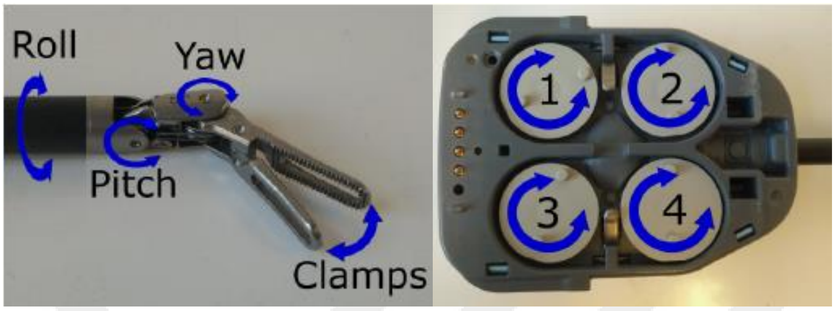

Figure 1.7. Davinci EndoWrist instrument and its motion axes

In Chan et al. [11, 23], the position-force control algorithm was proposed based on the extended active observer (EAOB) for a nonlinear bilateral teleoperation system. EAOB which is a kind of extended Kalman Filter updates the model parameters in real time to provide accurate state and force estimation simultaneously for both master and slave manipulators. EAO provides effective force tracking at the master side as the slave does position tracking in the presence of system inertial parameter uncertainties and measurement noise. In this method, only position measurement of the robot is necessary. Authors applied this method on a 2-DOF nonlinear robotic manipulator through computer simulation. However, this approach has not been applied to the real system yet. In reality, there occurs communication delay between master and slave manipulator in teleoperation system and this may result in poor force estimation and instability.

Mitsantisuk et al. [24] used Kalman filter based state observer and disturbance observer to estimate the disturbance and the external forces. This method is a combination of disturbance observer technique and Kalman filtering. Azimifar et al. [25] proposed another observer method for a nonlinear bilateral system under time delay to estimate forces and authors implemented this method on a 3-DOF Sensible Phantom Omni as the master and slave manipulator. The proposed controller achieved position tracking in free motion and force reflection when the slave robot is contact with the environment.

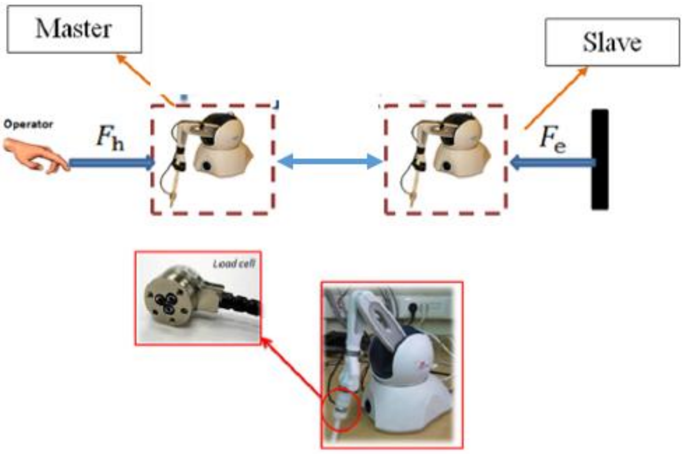

Figure 1.8. Bilateral teleoperation of 3-DOF Sensible Phantom Omni

As a result of the review of the available literature, there are many studies about estimating force feedback, compensating disturbances and designing teleoperation systems. However, there is no practical force sensing methods for robotic forceps systems that enable the estimation of external forces precisely at each axis in minimally invasive surgery due to the fact that the current surgical instruments consist of highly nonlinear cable-pulley or hydraulic systems.

1.2. Objectives

The objective of this study has been to accomplish the development of control systems and teleoperation algorithms that will solve the lack of force reflection during teleoperation for robotic minimally invasive surgery. Within this scope, a 4-DOF surgical forceps built around the wrist mechanism proposed by the author and colleagues [26] has been used due to the fact that it is able to provide force feedback inside the body. This surgical robot consists of a 3-DOF parallel wrist mechanism which can be actuated extra-corporally with rigid push-pull rods for pitch, yaw and thrust motions and a gripper for grasping.

In the beginning of this thesis, the forceps mechanism is introduced and its position and velocity kinematic equations are derived for the development of the control system and force estimation algorithms. The forceps mechanism has a nonlinear structure and unknown dynamics. It is required that a good controller must be designed by taking into account all the adverse effects, such as uncertainties, disturbances etc. acting on the forceps. Moreover, a novel force estimation method will be required, since the structure of the wrist is highly nonlinear and mechanical problems caused by manufacturing bring a lot of uncertainty. Development of a control system for the 4-DOF surgical forceps that can overcome nonlinearity, instability, uncertainties, and disturbances by using force estimation methods is aimed.

The 4-DOF robotic forceps that has been developed can be employed in minimally invasive procedures and can be used for grasping or palpation by estimating external forces. Therefore, a human operator (surgeon) can feel realistically external forces inside the body acting upon the end effector of the forceps during operation. According to the literature survey, there does not exist any forceps that can estimate contact forces accurately with force estimation algorithms and this mechanism will be a first in this field.

As an extension of this study, it will be possible to combine this 4-DOF forceps with an industrial robot to obtain 7-DOF in total (translational motions in x-, y-, z-axes, and rotational motions in roll, pitch, yaw axes, and gripper axis). The development and kinematic analysis of this combined surgical robot have been proposed in [27]. Force estimation and teleoperation algorithms developed are extended to the 7-DOF system that enables force feedback in each degree of freedom and provides a surgeon with force feedback in all the degrees of freedom of the human hand.

In the end, the proposed force estimation algorithm is implemented on a teleoperation system between two Phantom Omni robots which can be used in minimally invasive surgery and the estimated end-effector forces on the slave manipulator are validated using 1-DOF force sensor. Also, the developed method is compared to a computed torque method which requires a mathematical dynamic model of the robot.

2. A 4-DOF SURGICAL FORCEPS MECHANISM

For the purpose of the intra-corporeal bending and grasping motions in robotic surgery, a 4-DOF robotic forceps that can do pitch, yaw, thrust and grasping motions was designed as can be seen in Fig.2.1. Using this forceps, surgeon can feel external forces inside the body acting upon the end-effector of the forceps in each degree-of-freedom by the aid of its transmission system and force estimation and teleoperation algorithms during surgery. With its simple mechanical structure and an easy housing, it can be mounted to any industrial robot for the purpose of obtaining 7-DOF in total (translational motions in x, y, z axes, rotational motions in roll, pitch, yaw and gripping axis) and provide a surgeon with force feedback in all the degrees of freedom of the human hand.

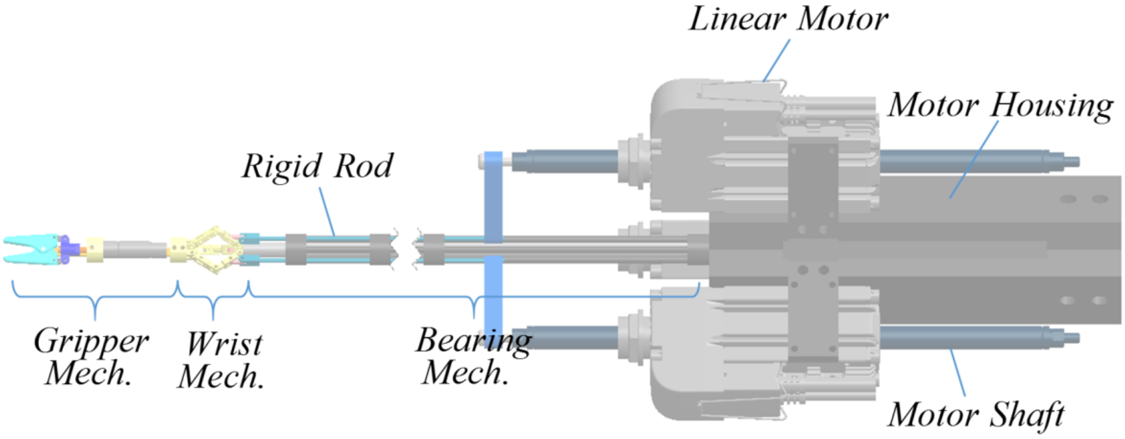

Figure 2.1. 4-DOF parallel forceps wrist mechanism

2.1. System Overview

The 4-DOF surgical forceps mechanism consists of the 3-DOF parallel wrist mechanism and 1-DOF gripper mechanism (Fig.2.2). The wrist is capable of doing pitch-yaw-thrust motions has been already manufactured and its design details and kinematic analysis were presented in [26]. For grasping motion, a spindle-drive is utilized by adding it to wrist top platform serially. The new mechanism can be examined in 2 parts: 3-DOF parallel wrist mechanism and gripper.

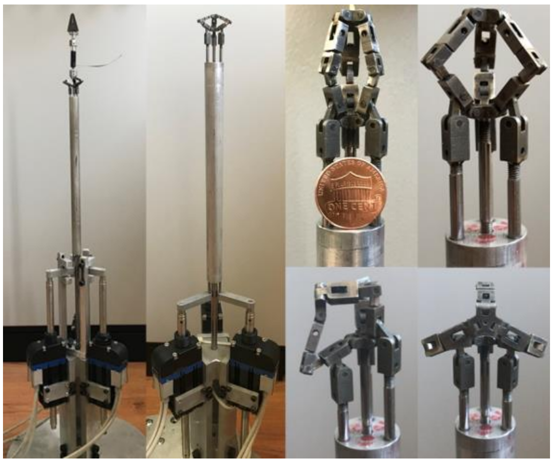

Figure 2.2. Forceps mechanisms with and without a gripper

2.1.1. 3-DOF Parallel Wrist Mechanism

The wrist is a 3-DOF parallel mechanism actuated extra-corporally by 3 linear motors and there are 3 identical serial chains at actuation part and wrist part of the mechanism. The motion of the motor part can be modeled with 3-PRR joints where P is prismatic and R is revolute joint and bottom links are connected to each other by means of this group of joints. The wrist part includes 3-RSR joints where S is spherical joint between top and bottom platforms and this group of joints provides parallel structure for the wrist. The visualization of joints are presented in Fig.2.3. Due to using rigid rods in transmission system, the wrist mechanism is highly back-drivable. Thus, it provides that forces acting on the end-effector of the wrist can be reflected to the actuators exactly.

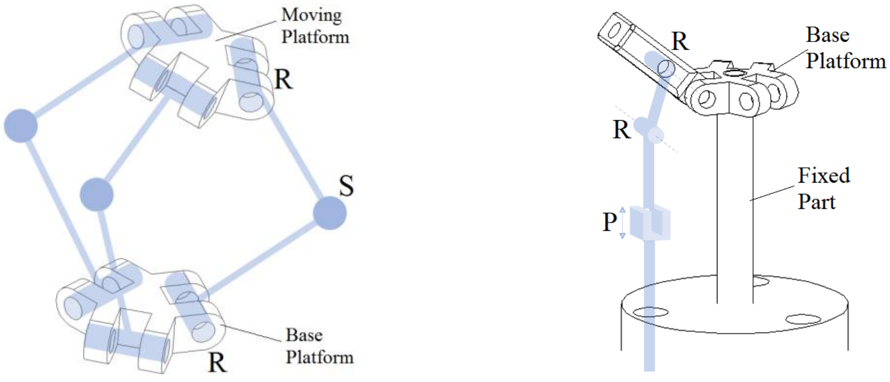

(a) (b)

Figure 2.3. Schematic representation of serial chains of 3-DOF wrist (a) 3-RSR (b) 3-PRR

With this structure, the wrist mechanism is able to do 2-DOF rotational (pitch/alpha, yaw/beta) and a radial translational (thrust/r) motions. Moreover, it has larger motion capability than human wrist so that it can do 90-degree rotations in pitch and yaw axes (Fig.2.4(a)). Also, its thrust motion can be used to pass through narrow incisions by changing its effective radius (Fig.2.4(b)). By means of this property, the workspace of the wrist mechanism can be expanded inside the body.

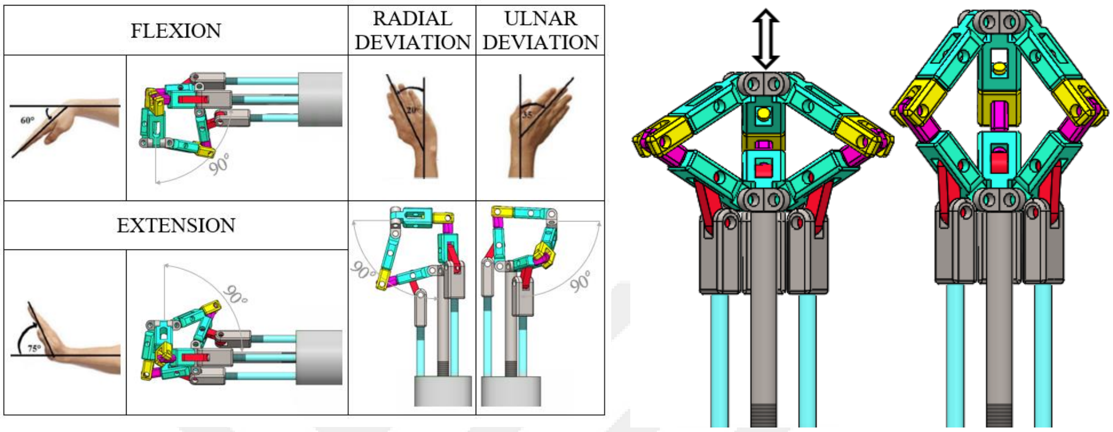
FLEXION
RADIAL DEVIATION
ULNAR DEVIATION
60°
90°
20°
35°
EXTENSION
75°
90°
90°
90°

(a) (b)

Figure 2.4. Degrees of freedom of the wrist mechanism (a) Comparison with the human wrist (b) Thrust motion

2.1.2. 1-DOF Gripper

For the grasping axis which is the fourth degree of freedom, a gripper is designed by the aid of two scissors including slider-crank mechanism that is a particular four-bar linkage configuration. The spindle drive is attached in series to the top platform of the wrist to open and close the gripper as can be seen in Fig.2.5. The spindle drive mechanism provides rotary motion to the lead screw and there is a sliding nut on this screw. When the screw turns, the nut moves linearly. With this principle, rotary motion of the spindle drive is converted into the linear motion. Therefore, that linear motion is transformed into grasping motion with the help of the slider-crank mechanism.

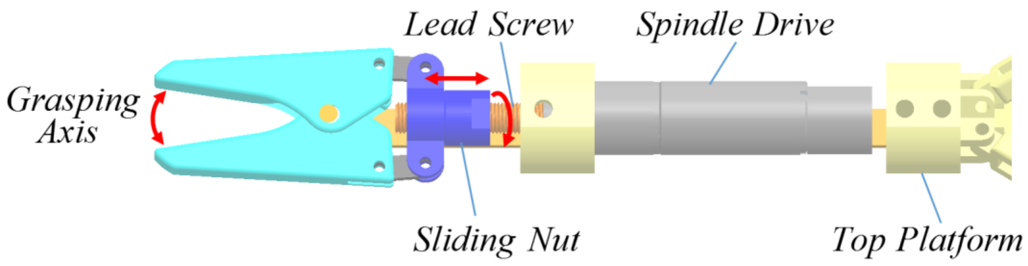
Lead Screw
Spindle Drive
Grasping Axis
Sliding Nut
Top Platform

Figure 2.5. Gripper Mechanism and transmission system

2.2. Position Kinematic Analysis

Kinematic position analysis is performed to

- Obtain mathematical model of the mechanism
- Determine constraints of the mechanism
- Find position/orientation relationships between the actuators and end-effector
- Generate workspace that shows motion range of the mechanism.

Kinematic analysis is derived separately for the 3-DOF wrist and the gripper.

2.2.1. Kinematic Analysis of the 3-DOF Parallel Wrist Mechanism

The 3-DOF parallel forceps wrist is able to do pitch (α), yaw (β) and thrust (r) motions. In this section, the forward and inverse kinematic equations which define mathematical modeling of the 3-DOF wrist mechanism are given and kinematic analysis steps can be seen that in Fig.2.6. According to kinematic solution, the relationship between motor positions (L_1, L_2, L_3) and tool position/orientation (α, β, r) is presented.

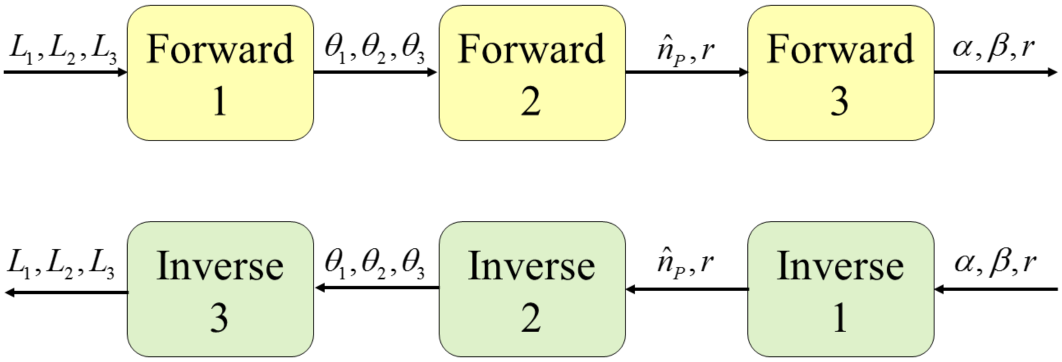
L_1, L_2, L_3
Forward 1
$\theta_1, \theta_2, \theta_3$
Forward 2
$\hat{n}_P, r$
Forward 3
α, β, r
L_1, L_2, L_3
Inverse 3
$\theta_1, \theta_2, \theta_3$
Inverse 2
$\hat{n}_P, r$
Inverse 1
α, β, r

Figure 2.6. 3-DOF wrist mechanism kinematic analysis steps

a) Forward Kinematics

In forward kinematics, the goal is to find tool position/orientation where the inputs are linear motor displacements.

i. Forward 1:

By the aid of loop closure equations, the complete kinematic information that gives relationship between L_i and θ_i are derived for each separate link,

$$
\begin{aligned}
x &\rightarrow L_i \cos\phi_{Li} = G\cos\phi_G + K_{1i}\cos\phi_{Ri} \\
y &\rightarrow L_i \sin\phi_{Li} = G\sin\phi_G + K_{1i}\sin\phi_{Ri}
\end{aligned} \tag{2.1}
$$

where L_i, G, ϕ_{Li} and ϕ_G are constant variables, ϕ_{Ri} is a summation of θ_i and ϕ_0,

$$\phi_{Ri} = \phi_0 + \theta_i \tag{2.2}$$

and K_{1i} is found from cosine theorem for 2nd loop,

$$K_{1i} = \sqrt{{L_i}^2 + G^2 - 2L_i G\cos\left(\phi_{Li} - \phi_G\right)} \tag{2.3}$$

Also, ϕ_0 is obtained by using cosine theorem for 1st loop where K_2 and K_3 are known parameters as shown in Fig.2.7,

$$\phi_0 = \cos^{-1}\left(\frac{{K_2}^2 + {K_{1i}}^2 - {K_3}^2}{2K_2K_{1i}}\right) \tag{2.4}$$

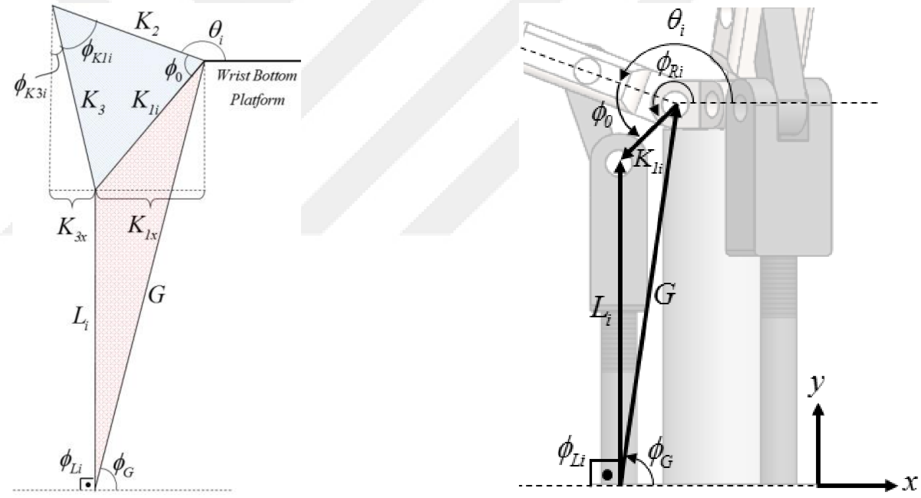
K_2
θ_i
ϕ_{K1i}
ϕ_0
Wrist Bottom Platform
ϕ_{K3i}
K_3
K_{1i}
K_{3x}
K_{1x}
L_i
G
ϕ_{Li}
ϕ_G
θ_i
ϕ_{Ri}
ϕ_0
K_{1i}
L_i
G
y
ϕ_{Li}
ϕ_G
x

(a) (b)

Figure 2.7. Representation of parameters used in geometric solution of motor parts (a) Detailed representation (b) General parameters

Rearranging (2.1) to get ϕ_{Ri} alone on the left side,

$$\phi_{Ri} = \cot^{-1}\left(\frac{L_i\cos\phi_{Li} - G\cos\phi_G}{L_i\sin\phi_{Li} - G\sin\phi_G}\right) \tag{2.5}$$

Then, θ_i is found by substituting (2.4) and (2.5) into (2.2),

$$\theta_i = \cot^{-1}\left(\frac{L_i\cos\phi_{Li} - G\cos\phi_G}{L_i\sin\phi_{Li} - G\sin\phi_G}\right) - \phi_0 \tag{2.6}$$

ii. Forward 2:

This section explains how the tool orientation unit vector $(\hat{n}_P)$ and thrust distance (r) are defined with respect to link angles (θ_i).

Based on Fig.2.8, the vertices ${}^{B}E_i$ on the midplane can be found by adding vectors whose unit vectors are ${}^{B}l_i$ to fixed points ${}^{B}F_i$ on the wrist bottom platform,

$$ {}^{B}E_i = {}^{B}F_i + D_i\, {}^{B}l_i \tag{2.7} $$

where D_i is the length of the links between points of ${}^{B}E_i$ and ${}^{B}F_i$ including x, y, z components,

$$ {}^{B}F_i = \begin{bmatrix} F_{ix} \\ F_{iy} \\ F_{iz} \end{bmatrix} \tag{2.8} $$

Here, F_{ix} equals to 0 because it has no component in –x axis on the wrist bottom platform and ${}^{B}l_i$ can be defined as a function of θ_i,

$$ {}^{B}l_i = \begin{bmatrix} s_i \\ -c_i c\phi_i \\ -c_i s\phi_i \end{bmatrix} \tag{2.9} $$

where $\phi_1 = 180^o$, $\phi_2 = 300^o$, $\phi_3 = 60^o$ and the notations of s_i and c_i symbolize $\sin\theta_i$ and $\cos\theta_i$, respectively. In Fig.2.9, the unit vector $\hat{u}$ which is from center of the bottom platform (B) to the center of the top platform can be computed by,

$$ \hat{u} = \frac{\left({}^{B}E_2 - {}^{B}E_1\right)\times\left({}^{B}E_3 - {}^{B}E_1\right)}{\left|\left({}^{B}E_2 - {}^{B}E_1\right)\times\left({}^{B}E_3 - {}^{B}E_1\right)\right|} = \begin{bmatrix} \hat{u}_x \\ \hat{u}_y \\ \hat{u}_z \end{bmatrix} \tag{2.10} $$

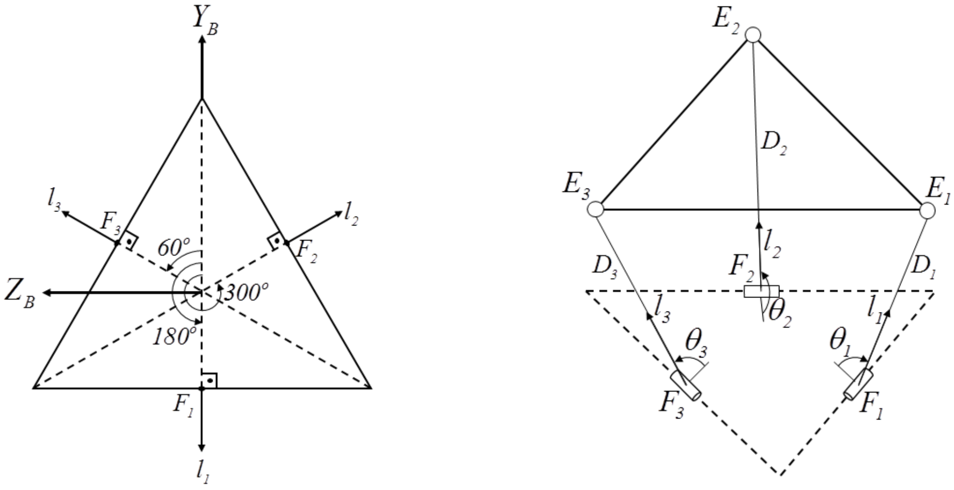
Y_B
l_3
F_3
$60°$
l_2
F_2
Z_B
$300°$
$180°$
F_1
l_1
E_2
D_2
E_3
E_1
l_2
F_2
D_3
D_1
l_3
θ_2
l_1
θ_3
θ_1
F_3
F_1

Figure 2.8. The kinematic structure diagrams of the wrist

The projection of r along $\hat{u}$ is $\frac{P}{2}$ and using this relation r is found:

$$r = \frac{P}{2\hat{n}_B \cdot \hat{u}} \tag{2.11}$$

where $\hat{n}_B = \begin{bmatrix} 1 & 0 & 0 \end{bmatrix}^T$ is the unit vector perpendicular to the bottom platform at point B and P is the projection of ${}^B E_i$ onto $\hat{u}$,

$$P = 2\left({}^B E_1 \cdot \hat{u} \right) \tag{2.12}$$

Then, using the relationship:

$$\hat{n}_B r + \hat{n}_{\mathrm{P}}\, \mathrm{r} = {}^B P \tag{2.13}$$

Here, ${}^B P$ is defined as following:

$$ {}^B P = \hat{u}P = r \begin{bmatrix} 1 + \hat{n}_{Px} \\ \hat{n}_{Py} \\ \hat{n}_{Pz} \end{bmatrix} \tag{2.14}$$

$\hat{n}_P$ can be computed by substituting (2.11) and (2.12) into (2.13):

$$\hat{n}_P = \frac{{}^B P}{r} - \hat{n}_B \tag{2.15}$$

iii. Forward 3:

In this section, tool orientation/position (α, β, r) are calculated by using $\hat{n}_P$ and r that are found in Forward 2 and transformation matrix associated with the Denavit-Hartenberg (DH) parameters is derived using frames in Fig.2.9(b). To find α and β, the relationship that the first column of the transformation matrix equals to $\hat{n}_P$ is used since the direction is perpendicular to base is chosen as –x axis. DH parameters are shown in Table 2.1.

$$ {}_P^BT = \begin{bmatrix} c\alpha c\beta & -s\alpha & c\alpha s\beta & r(1+c\alpha c\beta) \\ s\alpha c\beta & c\alpha & s\alpha s\beta & rs\alpha c\beta \\ -s\beta & 0 & c\beta & -rs\beta \\ 0 & 0 & 0 & 1 \end{bmatrix} \tag{2.16} $$

And, the first column of ${}_P^BT$ is

$$ \hat{n}_P = \begin{bmatrix} c\alpha c\beta \\ s\alpha c\beta \\ -s\beta \end{bmatrix} \tag{2.17} $$

Table 2.1. DH Parameters of the 3-DOF Wrist

i	θ_i	d_i	α_{i-1}	a_{i-1}
1	0	0	0	r
2	α	0	0	0
3	β	0	$-\pi/2$	0
4	0	0	$\pi/2$	r

Although thrust distance is an input parameter in this part, it is considered also as output parameter and it was found in (2.11). As a result, α and β can be calculated from (2.17),

$$ \begin{aligned} \alpha &= a\tan 2\left(\hat{n}_P(2), \hat{n}_P(1)\right) \\ \beta &= a\tan 2\left(-\hat{n}_P(3), \sqrt{\hat{n}_P(1)^2 + \hat{n}_P(2)^2}\right) \end{aligned} \tag{2.18} $$

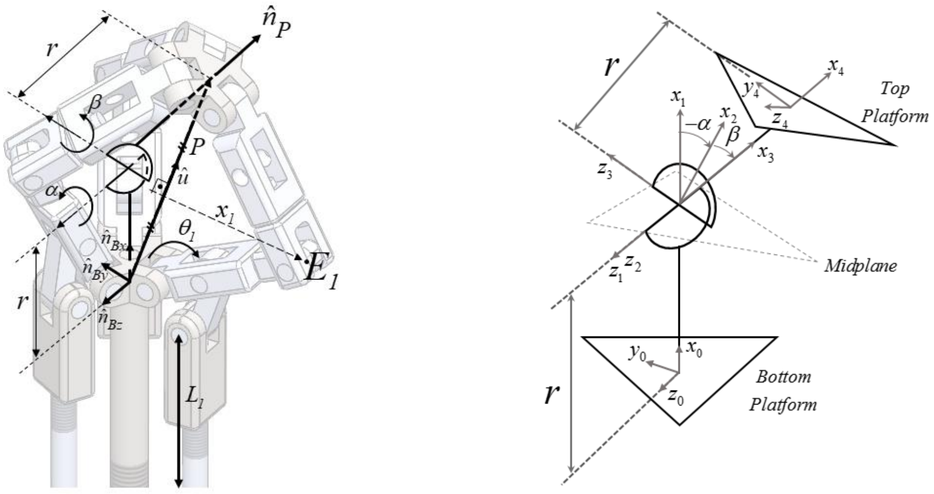

r
$\hat{n}_P$
β
P
$\hat{u}$
α
x_1
θ_1
$\hat{n}_{Bx}$
$\hat{n}_{By}$
$\hat{n}_{Bz}$
E_1
r
L_1
r
x_1
$-\alpha$
x_2
β
x_3
x_4
y_4
z_4
Top Platform
z_3
z_2
z_1
Midplane
r
y_0
x_0
z_0
Bottom Platform

(a) (b)

Figure 2.9. The parameters of the wrist (a) General representation (b) DH parameters

b) Inverse Kinematics

Inverse kinematics is utilized to find necessary joint positions to reach a desired end-effector position/orientation.

i. Inverse 1:

The purpose of this section is to calculate tool unit vector $\hat{n}_P$ and thrust distance r as a function of α, β, r and $\hat{n}_P$ can be obtained from (2.17).

ii. Inverse 2:

In this section, the link angles are computed based on $\hat{n}_P$ and r. Link angles can be obtained by using 2 constraint equations that give relationship between θ_i and $\hat{n}_P$:

$$x_i \cdot \hat{u} = 0 \tag{2.19}$$

$$\frac{P}{2}\hat{u} + x_i = {}^{B}E_i \tag{2.20}$$

In (2.19) and (2.20), x_i is a vector directing from the center of the ${}^{B}P$ vector to ${}^{B}E_i$ and it must be perpendicular to $\hat{u}$.

By substituting (2.19) into (2.20),

$$\left({}^{B}E_i - \frac{P}{2}\hat{u} \right) \cdot \hat{u} = 0 \tag{2.21}$$

Here, $\hat{u}$ is defines as

$$\hat{u} = \frac{{}^{B}P}{\left|{}^{B}P\right|} \tag{2.22}$$

Also, ${}^{B}P$ is calculated by

$${}^{B}P = r\left(\hat{n}_B + \hat{n}_P\right) \tag{2.23}$$

where $\hat{n}_B = \begin{bmatrix} 1 & 0 & 0 \end{bmatrix}^T$ and $\hat{n}_P = \begin{bmatrix} \hat{n}_{Px} & \hat{n}_{Py} & \hat{n}_{Pz} \end{bmatrix}^T$. By substituting (2.7), (2.22) and (2.23) into (2.21), 3 constraint equations can be obtained for 3 serial links,

$$V_i c_i + Y_i s_i + Z_i = 0 \tag{2.24}$$

In (2.24), V_i, Y_i and Z_i are the parameters which include constant link lengths, tool unit vector and thrust distance. Then, θ_i values can be computed by,

$$\theta_i = 2\tan^{-1}\left(\frac{-Y_i \pm \sqrt{Y_i^2 - Z_i^{\,2} + V_i^2}}{Z_i - V_i} \right) \tag{2.25}$$

iii. Inverse 3:

This section gives the solution for actuator positions based on link angles. Since each serial chain has same geometry, actuator positions $\left(L_i\right)$ can be found by the aid of loop closure equations for only one serial chain,

$$L_i = \frac{-G\cos\phi_G \sin\phi_{Ri}}{\cos\phi_{Ri}} + G\sin\phi_G \tag{2.26}$$

where ϕ_G is a constant parameter and ϕ_{Ri} is variable depending on the change of θ_i. For this reason, firstly ϕ_{Ri} is found by summation of θ_i and ϕ_0 and ϕ_0 is formulated in (2.4). In (2.4), K_{1i} changes depending on ϕ_{K1i} which can be found as,

$$\phi_{K1i} = \sin^{-1}\left(\frac{K_{3x} + K_{1x}}{K_2} \right) - \sin^{-1}\left(\frac{K_{3x}}{K_3} \right) \tag{2.27}$$

Using (2.27), K_{1i} can be calculated by applying cosine theorem for the first loop that can be seen in Fig.2.7(a),

$$K_{1i} = \sqrt{{K_2}^2 + {K_3}^2 - 2K_2K_3 \cos\phi_{K1i}} \tag{2.28}$$

In (2.28), N is

$$N = \sqrt{a^2 + b^2 - 2ab\cos\phi_a} \tag{2.29}$$

2.2.2. Kinematic Analysis of the 1-DOF Gripper

The forward and inverse kinematic equations of the gripper mechanism are derived by taking a geometric approach for the gripper in this section. In Fig.2.10, the parameters that are used in kinematic equations are shown. Spindle drive displacement $\left(s_d\right)$ is transformed to grasping angle $\left(\theta_g\right)$ or vice versa through these kinematic equations.

a) Forward Kinematics

The purpose of forward kinematics is to find grasping angle $\left(\theta_g\right)$ from given desired motor displacement $\left(s_d\right)$.

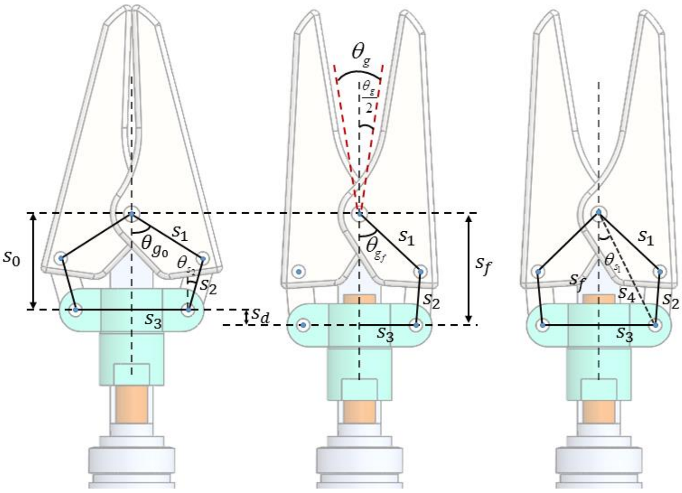

Figure 2.10. Parameters used in gripper kinematic analysis

s_f is the summation of s_0 and s_d when the gripper is open,

$$s_f = s_0 + s_d \tag{2.30}$$

where s_0 is the initial length when the gripper is closed.

Using the cosine theorem, following equation can be described as,

$$s_2{}^2 = s_1{}^2 + s_4{}^2 - 2s_1s_4\cos\left(\theta_{gf} - \theta_{s1}\right) \tag{2.31}$$

In (2.31), s_1 and s_2 are constant parameters that are link lengths. θ_{s1} is calculated based on the right-angled triangle:

$$\theta_{s1} = \tan^{-1}\left(\frac{s_3}{s_f}\right) \tag{2.32}$$

where s_3 is constant variable and s_4 can be computed using Pythagoras theorem,

$$s_4 = \sqrt{s_f{}^2 + s_3{}^2} \tag{2.33}$$

By substituting (2.32) and (2.33) into (2.31), θ_{gf} is isolated,

$$\theta_{gf} = \cos^{-1}\left(\frac{s_1{}^2 - s_f{}^2 - s_3{}^2 - s_2{}^2}{2s_1\sqrt{s_f{}^2 + s_3{}^2}}\right) + \theta_{s1} \tag{2.34}$$

Then, grasping angle $\left(\theta_g\right)$ is obtained,

$$\theta_g = 2\left(\theta_{g0} - \theta_{gf}\right) \tag{2.35}$$

where θ_{g0} is the initial angle between links s_f and s_1 when the gripper is closed.

b) Inverse Kinematics

The goal of inverse kinematics is to calculate desired position of the spindle drive $\left(s_d\right)$ as a function of grasping angle $\left(\theta_g\right)$.

θ_{gf} is found from (2.35) and θ_{s2} is calculated by substituting into following equation,

$$\theta_{s2} = \sin^{-1}\left(\frac{s_1\sin\theta_{gf} - s_3}{s_2}\right) \tag{2.36}$$

s_f is the sum of link lengths in vertical axis,

$$s_f = s_1\cos\theta_{\mathrm{gf}} + s_2\cos\theta_{s2} \tag{2.37}$$

Therefore, desired spindle position $\left(s_d\right)$ is calculated,

$$s_d = s_f - s_0 \tag{2.38}$$

2.3. Velocity Kinematic Analysis

With velocity kinematic analysis, Jacobian of the manipulator that is utilized in force estimation is found by differentiating forward kinematic equations. Total Jacobian matrix is composed of 2 parts that are 3-DOF wrist mechanism (J_1) and motor parts (J_2), respectively.

J_1 matrix gives the change in the unit vector $\hat{n}_P$ as a function of the change in link angles. $\hat{n}_{Py}$ and $\hat{n}_{Pz}$ are the components of tool unit vector and r motion is realized in –x axis. To find J_2 matrix, partial derivation of link angles is necessary with respect motor displacements (L_i).

$$J_1 = \begin{bmatrix} \frac{\partial \hat{n}_{Py}}{\partial \theta_1} & \frac{\partial \hat{n}_{Py}}{\partial \theta_2} & \frac{\partial \hat{n}_{Py}}{\partial \theta_3} \\ \frac{\partial \hat{n}_{Pz}}{\partial \theta_1} & \frac{\partial \hat{n}_{Pz}}{\partial \theta_2} & \frac{\partial \hat{n}_{Pz}}{\partial \theta_3} \\ \frac{\partial r}{\partial \theta_1} & \frac{\partial r}{\partial \theta_2} & \frac{\partial r}{\partial \theta_3} \end{bmatrix} \qquad J_2 = \begin{bmatrix} \frac{\partial \theta_1}{\partial L_1} & \frac{\partial \theta_1}{\partial L_2} & \frac{\partial \theta_1}{\partial L_3} \\ \frac{\partial \theta_2}{\partial L_1} & \frac{\partial \theta_2}{\partial L_2} & \frac{\partial \theta_2}{\partial L_3} \\ \frac{\partial \theta_3}{\partial L_1} & \frac{\partial \theta_3}{\partial L_2} & \frac{\partial \theta_3}{\partial L_3} \end{bmatrix} \tag{2.39}$$

The Jacobian of the whole system is the multiplication of J_1 and J_2,

$$J = J_1 J_2 \tag{2.40}$$

In final step, time derivatives of tool orientation/position are found using a transformation matrix that gives the relation between the time derivatives of $\hat{n}_{Py}$, $\hat{n}_{Pz}$ and α, β,

$$\begin{bmatrix} \dot{\alpha} \\ \dot{\beta} \\ \dot{r} \end{bmatrix} = \begin{bmatrix} & & 0 \\ & T_{2x2} & 0 \\ 0 & 0 & 1 \end{bmatrix} J_1 J_2 \begin{bmatrix} \dot{L}_1 \\ \dot{L}_2 \\ \dot{L}_3 \end{bmatrix} \tag{2.41}$$

where

$$\begin{bmatrix} \dot{\alpha} \\ \dot{\beta} \end{bmatrix} = T_{2x2} \begin{bmatrix} \dot{\hat{n}}_{Py} \\ \dot{\hat{n}}_{Pz} \end{bmatrix} \tag{2.42}$$

3. CONTROL SYSTEM OF A 4-DOF FORCEPS MECHANISM

A closed-loop control system, also known as a feedback control system is a system which manages or controls devices or systems in order to provide the desired response by controlling the output. The control action of the controller is dependent on the desired and actual process variable and a controller produces an actuating signal which controls the plant in order to improve the system performance by maintaining stability, rejecting disturbances and reducing tracking error in a good control system (Fig.3.1).

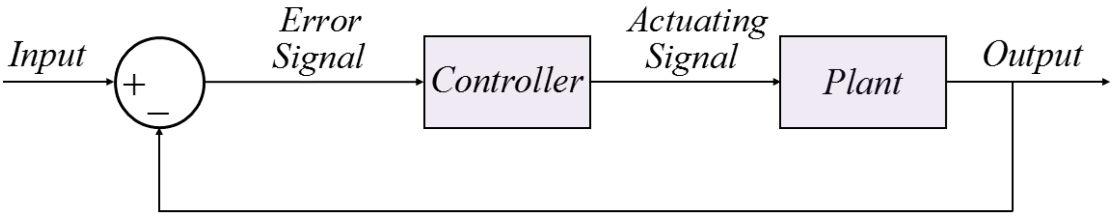
Input
+
_
Error Signal
Controller
Actuating Signal
Plant
Output

Figure 3.1. A general closed-loop control system

Considering the control system of the forceps mechanism with and without a gripper in Joint-space, two common controllers were applied which are the Disturbance Observer based Proportional-Integral-Derivative (PID) controller and Sliding Mode Controller (SMC). In both systems, orientation and positions of the wrist mechanism that are pitch, yaw and thrust motions are given to control system as reference inputs $\left(x=[\alpha,\beta,\mathrm{r}]\right)$ and they are transformed into position commands for each motor $\left(q^{ref}=L_i^{ref}\ with\ i=1{:}3\right)$ solving the kinematic equations of the wrist mechanism developed in Section 2 (Fig.3.2). Briefly, the main goal for designing a Joint-space (JS) controller is to find how much forces should be applied to the motors by minimizing the error in order to realize the desired motion $\left(q^{ref}\right)$ [28-30].

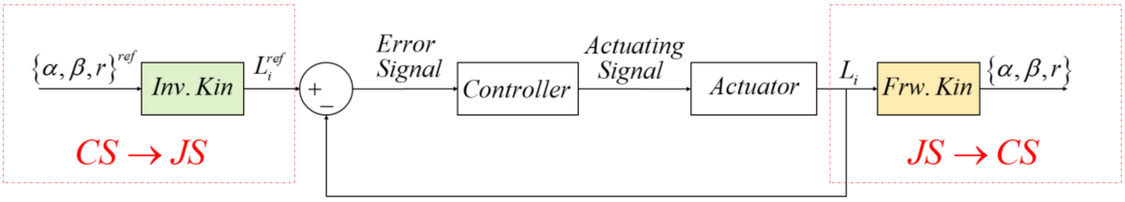
$\{\alpha,\beta,r\}^{ref}$
Inv. Kin
L_i^{ref}
CS → JS
+
_
Error Signal
Controller
Actuating Signal
Actuator
L_i
Frw. Kin
$\{\alpha,\beta,r\}$
JS → CS

Figure 3.2. A general schema of a control system of the wrist mechanism

3.1. PID Controller with Disturbance Observer

To increase the robustness of the system and suppress disturbances caused by gravitational, friction forces and effects of parameter variations, DOBS is utilized in addition to PID controller.

3.1.1. Conventional PID Controller

The conventional Proportional-Integral-Derivative (PID) controller is a most common linear feedback controller widely used in industry with the functionality of three terms which are proportional, derivative and integral. Output of a PID controller can be written in time domain as:

$$u(t) = K_p e(t) + K_i \int_0^t e(\tau) d\tau + K_d \frac{d}{dt} e(t) \tag{3.1}$$

Where t denotes time, $u(t)$ is the control input, K_p is the proportional gain, K_i the integral gain, K_d the derivative gain and $e(t)$ is steady-state error as a function of time. In (3.1), $e(t)$ is the difference between desired position $\left(q^{ref}\right)$ and actual position (q) in the closed loop control system:

$$e = q^{ref} - q \tag{3.2}$$

In the Laplace domain (s-domain), (3.1) can be written as:

$$U(s) = \left(K_p + \frac{K_i}{s} + sK_d \right) E(s) \tag{3.3}$$

The fundamental functionalities and effects on the system of PID parameters are:

- P term provides that a control signal is proportional to the error signal.
- I term eliminates the steady-state error.
- D term reduces oscillations and works on the rate of state changes.

Assuming these functionalities, the most important thing is to determine and tune PID parameters to control the system and provide the proper control actions. There are a lot of ways for PID tuning, such as analytical, heuristic, frequency response, trial-and-error and adaptive tuning methods [31]. In this study, unity feedback system by choosing a JS controller as a PD controller was considered and PD gains were tuned using the trial-and-error method which satisfies the criteria for a good control system.

3.1.2. Disturbance Observer

In addition to PID controller, disturbance observer which is a disturbance estimation method is utilized for disturbance compensation and the disturbance force estimate is fed back to the system to provide robust motion control based on acceleration control of electric motors and robot manipulator using DOBS [21].

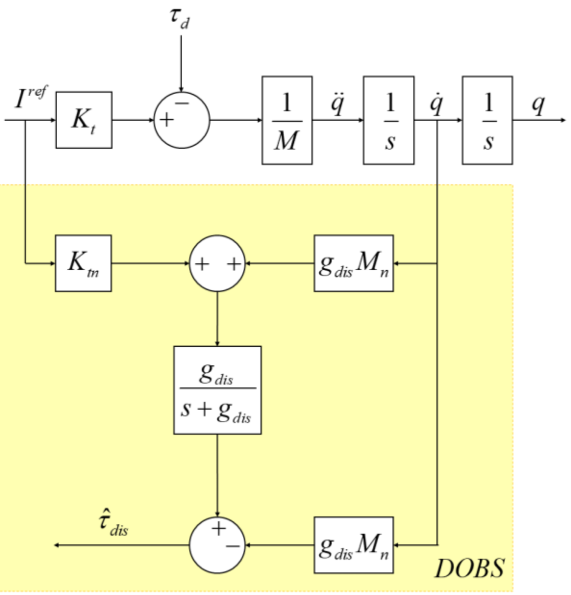

Figure 3.3. Disturbance observer

A joint-space disturbance observer contains a nominal model of the motor and a low-pass filter which can estimate the total disturbance acting on the motor. The block diagram of disturbance observers used in the control of linear actuators of the robotic wrist is shown in Fig.3.3. In Fig 3.3, g_{dis} is the cut-off frequency of the low-pass filter, M and M_n are actual and nominal mass values, I^{ref} is the supplied current, K_t and K_{tn} are actual and nominal force constant values and q is the position measurement of motor encoders. The disturbance estimate in frequency domain on linear motors can be written as,

$$\hat{\tau}_{dis} = \frac{g_{dis}}{s+g_{dis}}\left(I^{ref}K_{tn} + g_{dis}M_n q\right) - g_{dis}M_n\dot{q} \tag{3.4}$$

$$\hat{\tau}_{dis} = \frac{g_{dis}}{s+g_{dis}}\tau_{dis} \tag{3.5}$$

The disturbance estimate is fed back to the system in order to realize robust acceleration control with the following control law:

$$\ddot{q}^{des} = \ddot{q}^{ref} + K_p\left(q^{ref} - q\right) + K_d\left(\dot{q}^{ref} - \dot{q}\right) \tag{3.6}$$

The error with (3.6) becomes:

$$Q^{ref} - Q = \frac{G(s)}{M_n\left(s^2 + sK_d + K_p\right)}\tau^{dis} \tag{3.7}$$

with the disturbance sensitivity function $G(s)$ [32]. Therefore, the robust controller is achieved and the error becomes zero if disturbance observer works ideally.

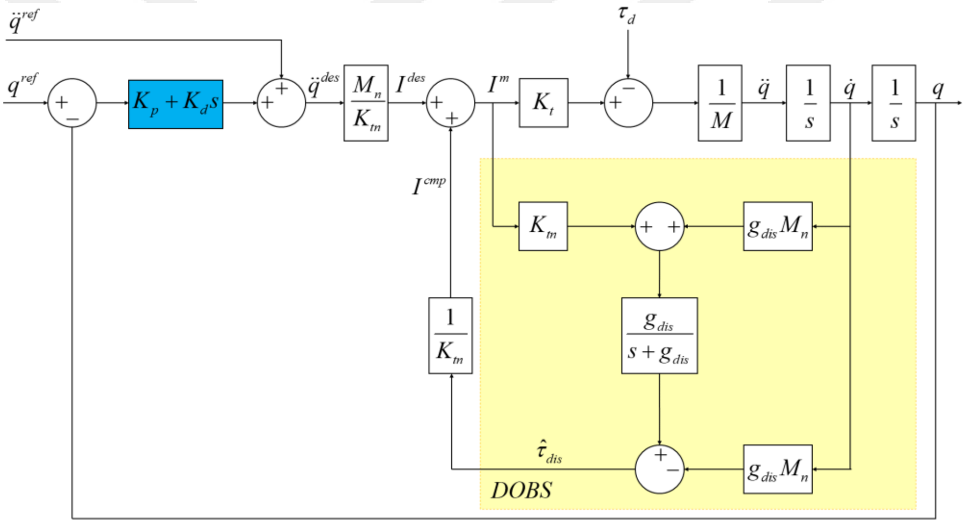
$\ddot{q}^{ref}$
τ_d
q^{ref}
$K_p + K_d s$
$\ddot{q}^{des}$
$\frac{M_n}{K_{tn}}$
I^{des}
I^m
K_t
$\frac{1}{M}$
$\ddot{q}$
$\frac{1}{s}$
$\dot{q}$
$\frac{1}{s}$
q
I^{cmp}
K_{tn}
$g_{dis}M_n$
$\frac{g_{dis}}{s+g_{dis}}$
$\frac{1}{K_{tn}}$
$\hat{\tau}_{dis}$
$g_{dis}M_n$
DOBS

Figure 3.4. Joint-space position control diagram using PD controller with DOBS

In this study, the PID controller with DOBS was applied on both 3-DOF and 4-DOF wrist mechanisms and the wrists were moved by Falcon robot in real time with the sample time of 0.001s. The motor position and end-effector position responses due to the reference signals for 3-DOF and 4-DOF wrists are depicted in Fig.3.5-6. From the experiment results performed by 3-DOF wrist, it is clear that perfect tracking responses and robust motion characteristics are obtained in both JS and CS positions (Fig.3.5) with maximum RMS error values of 0.0856 mm in JS, 0.9386^{o} in α and 0.0963 mm in r (Table 3.1). However, in experiments performed using 4-DOF wrist, during the stage where the wrist passes to straight position when α and β go to zero, it is seen that oscillations occurred from Fig.3.6 due to the limited bandwidth of the low-pass filter in DOBS [33]. Since the force exerted on the each motor changes more compared to 3-DOF forceps mechanism during motion because of the gripper weight, it causes large parametric uncertainties and disturbance compensation is not achieved ideally with the chosen cut-off frequency.

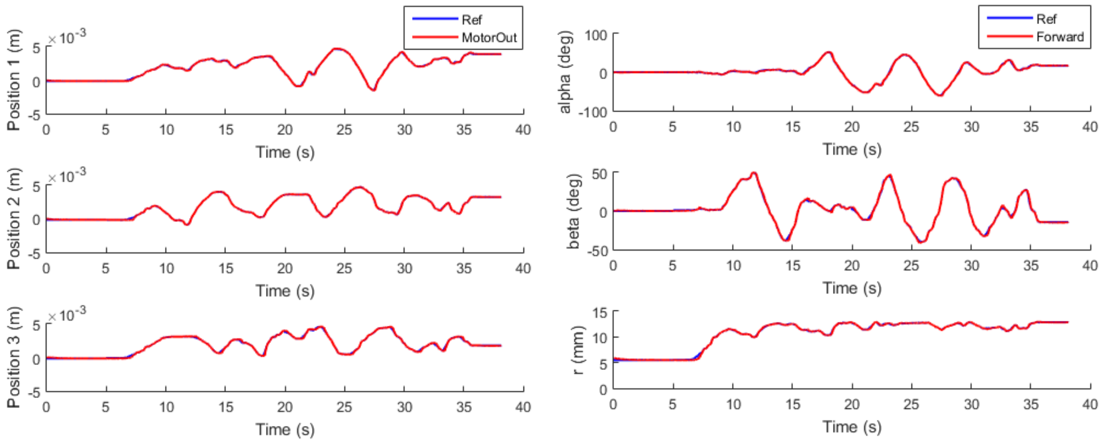

(a) (b)

Figure 3.5. Position control results of 3-DOF wrist excluding gripper using PID and DOBS in (a) Joint space (b) Cartesian space

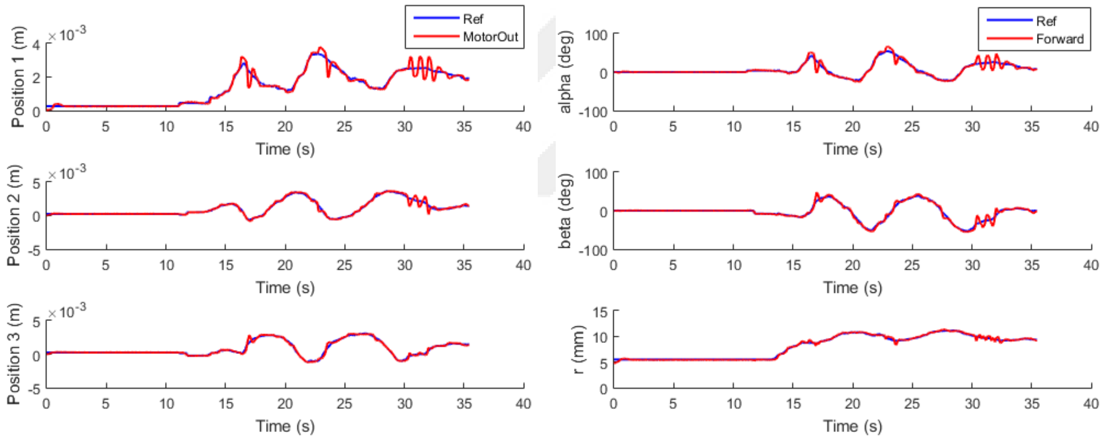

(a) (b)

Figure 3.6. Position control results of 4-DOF wrist including gripper using PID and DOBS in (a) Joint-space (b) Cartesian -space

Table 3.1. Comparison of RMS errors of position control results for 3-DOF and 4-DOF wrist mechanisms

	RMSE in L1 (mm)	**RMSE in L2 (mm)**	**RMSE in L3 (mm)**
3-DOF wrist	0.0485	0.0357	0.0856
4-DOF wrist	0.1961	0.1899	0.1425
	RMSE in α (deg)	**RMSE in β (deg)**	**RMSE in r (mm)**
3-DOF wrist	0.8513	0.9386	0.0963
4-DOF wrist	5.4091	4.0389	0.1713

3.2. Sliding Mode Control

Sliding mode control is a robust nonlinear control method that was proposed in the early 1950s [34]. In this method, uncertainties are considered and the response of the system is stabilized using nonlinear feedback. The main idea is that the control input switches rapidly between control limits in the presence of uncertainties and external disturbances. The design of an ideal sliding mode controller has three fundamental steps [35]:

- Designing sliding (switching) surface $s(t)$ on which the system has desired dynamic behavior, control specifications and performance where $s(t)$ is a function of error $e(t)$,

$$s(t)=e(t)+\lambda\dot{e}(t) \tag{3.8}$$

- Designing the control law based on $s(t)$ such that the system state trajectories are forced to track and slide on the surface and the error remains on the sliding surface $s(t)=0$ for all $t\geq 0$ even with disturbances.
- Compensation of chattering which is an undesirable high frequency oscillation around the sliding surface and affects the control performance negatively.

Considering the 4-DOF wrist mechanism, SMC is used as a joint space position controller where q is a vector of linear motor displacements. In the beginning, the first order sliding mode control was implemented where the control input is discontinuous on the wrist actuators;

$$u=-U\,sgn(s) \tag{3.9}$$

(3.9) is defined as with a sufficiently large positive constant U :

$$u=\begin{cases}-U & s>0\\ U & s<0\end{cases} \tag{3.10}$$

Using (3.10), the control input u changes its value between $-U$ and U at a very high frequency depending on the sliding surface condition and obviously this high frequency caused a chattering problem that can be seen as the “Zigzag” motion. (Fig.3.7(a)).

To overcome chattering problem, instead of using discontinuous sign term in (3.9), a continuous smooth approximation that is saturation function was used as described in the following equation:

$$u = U\,\mathrm{sat}(s,\varepsilon) = \begin{cases} U\,\mathrm{sgn}(s) & |s| > \varepsilon \\ \dfrac{Us}{\varepsilon} & |s| \le \varepsilon \end{cases} \tag{3.11}$$

Here, ε is a small positive number. By implementing (3.11) and choosing sliding surface as in (3.8), smoother tracking was achieved without compromising the robustness. The difference between the responses of both SMC with $\mathrm{sgn}(s)$ and $\mathrm{sat}(s)$ can be seen in Fig.3.7.

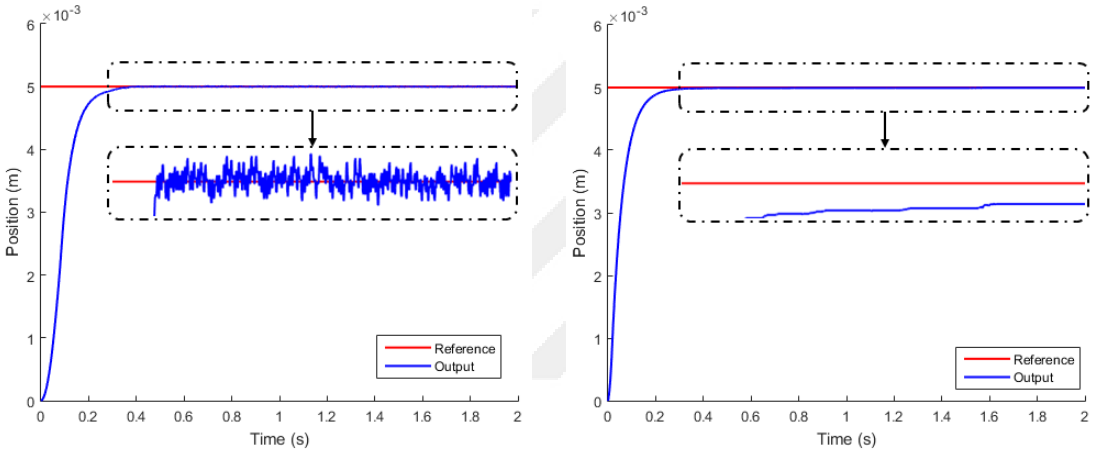

(a) (b)

Figure 3.7. Position control result of 1-DOF motor with SMC using (a) sgn function (b) sat function

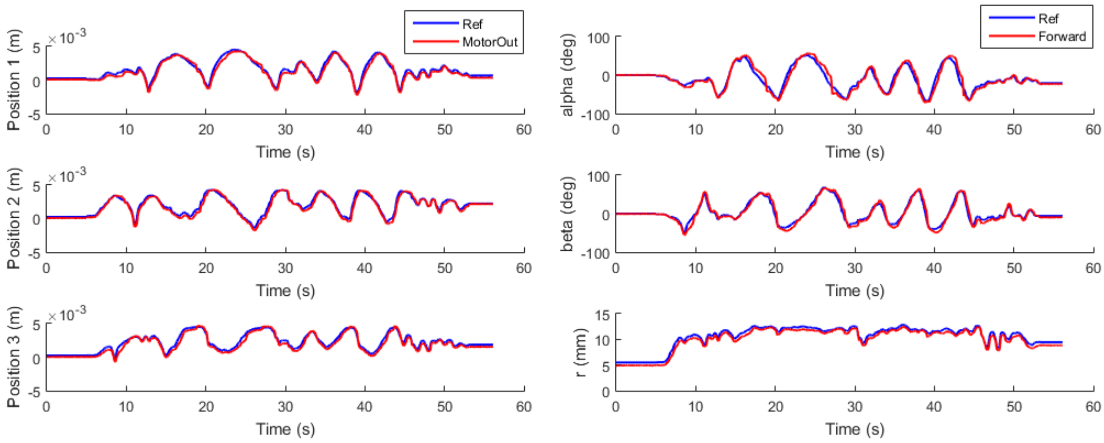

(a) (b)

Figure 3.8. Position control result of 3-DOF wrist with SMC using sat function in (a) Joint-space (b) Cartesian-space

However, although chattering problem was solved with $\mathrm{sat}(s)$ function, steady-state error has occurred because of the sliding surface chosen as in (3.8). Also, this problem can be seen in the experiment using 4-DOF wrist mechanism including gripper.

For this reason, integral term was added to sliding surface to achieve zero steady-state error and sliding surface function was chosen as:

$$s(t)=k_1 e(t)+k_2\int_0^t e(\tau)d\tau+k_3\frac{de(t)}{dt} \tag{3.12}$$

where the coefficients k_1, k_2 and k_3 are strictly positive constants.

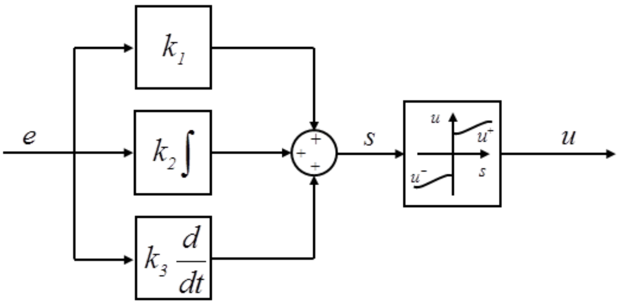

Figure 3.9. SMC diagram with relay function

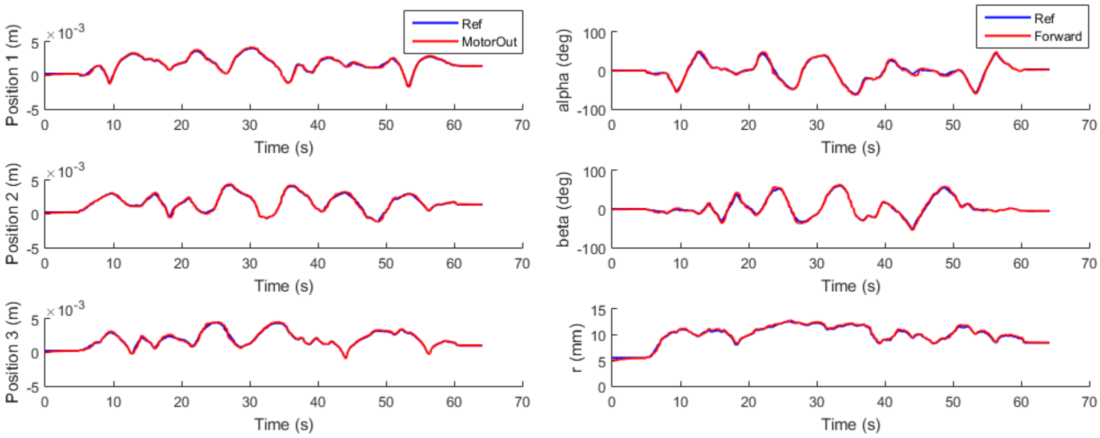

(a) (b)

Figure 3.10. Position control result of 4-DOF wrist mechanism using SMC with integral term in (a) Joint-space (b) Cartesian-space

Table 3.2. Comparison of RMS errors of position control results w/o integral term in Joint-space and Cartesian-space

	RMSE in L1 (mm)	**RMSE in L2 (mm)**	**RMSE in L3 (mm)**
w/o Integral	0.3609	0.3233	0.3686
w Integral	0.1056	0.1185	0.1220
	RMSE in α (deg)	**RMSE in β (deg)**	**RMSE in r (mm)**
w/o Integral	8.1916	6.2747	0.5429
w Integral	2.5081	2.5948	0.1746

3.3. Comparison of DOBS based PID Controller and SMC with Integral Term

To demonstrate the performance of the system using combination of PID and DOBS and SMC with integral term, experiments were carried out on the 4-DOF wrist mechanism. Firstly, reference pitch, yaw and thrust signals were generated for the 4-DOF forceps mechanism by Falcon robot. These recorded reference signals were given to both systems which are controlled using PID with DOBS and SMC, separately. Some captures from experiments can be seen in Fig.3.11(a) during motion. Cartesian space position responses for the SMC and DOBS based PID controller for a given reference position are illustrated in Fig.3.11(b-d). It is observed that the performance of the SMC is much better than DOBS based PID. In some cases of using PID, it can be seen that oscillations occurred during teleoperation since its efficiency is limited when applying in nonlinear systems. On the other hand, these results confirm that SMC presents a better tracking performance than PID with small RMS error values that are 2.0147° in α, 1.9365° in β, 0.1088 mm in r (Table 3.3) and it suppresses disturbance effect caused by the weight of the gripper mechanism .

Table 3.3. Comparison of RMS errors in CS space using PID and SMC controllers

	RMSE in α (deg)	**RMSE in β (deg)**	**RMSE in r (mm)**
PID	5.0407	3.1444	0.1289
SMC	2.0147	1.9365	0.1088

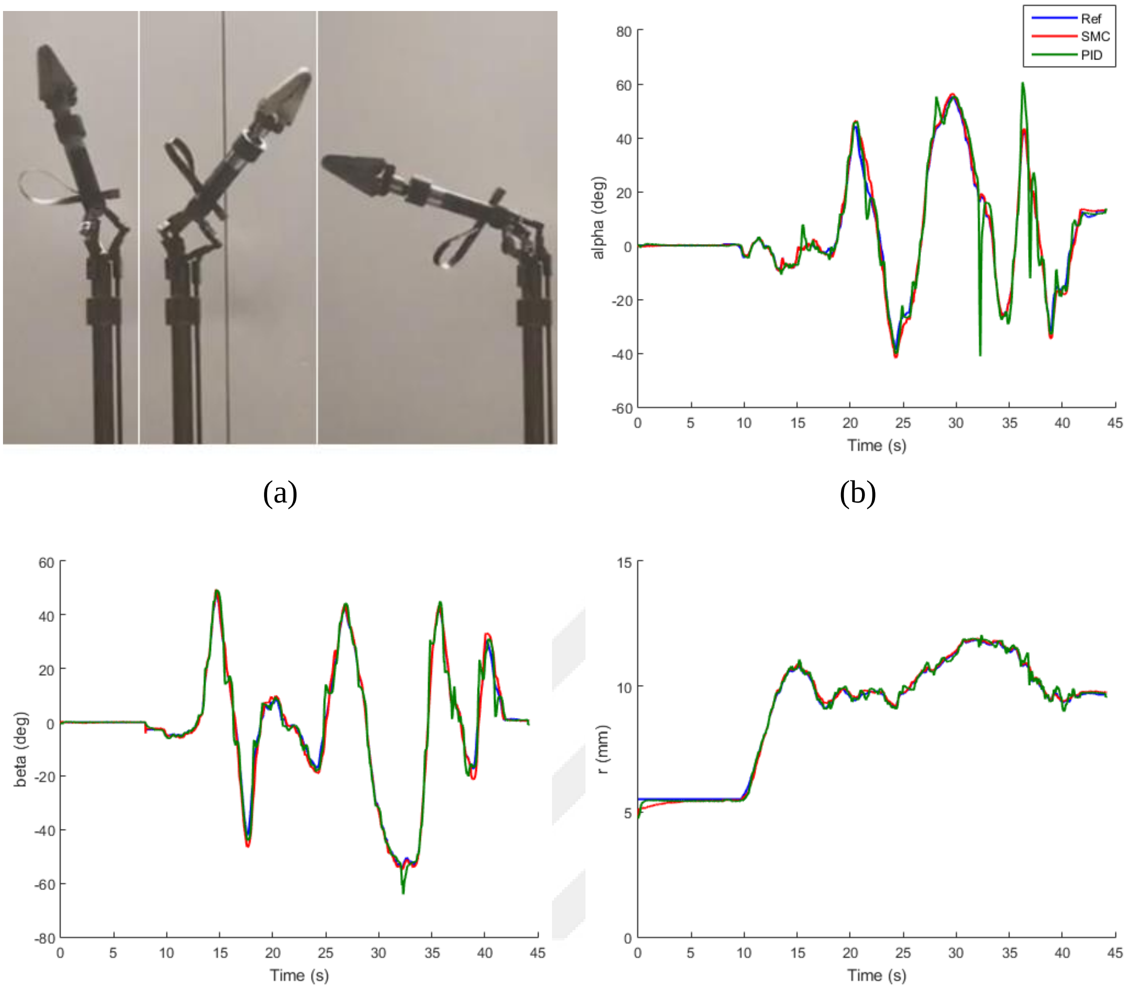

(a) (b)

(c) (d)

Figure 3.11. Comparison of PID and SMC controllers sending the same position reference to 4-DOF wrist (a) Experiment setup (b) alpha axis (c) beta axis (c) Thrust axis

4. EXTERNAL FORCE/TORQUE ESTIMATION METHOD

This section describes a novel sensorless force estimation algorithm that was proposed in [36] for any robot whose dynamics is unknown. The method utilizes novel reaction force observer (RFOB) in joint space, which are modified disturbance observers (DOBS) combined with Neural Networks (NN) for inverse dynamics calculations to estimate external forces acting on the motors. External force/torque estimation in Cartesian space is achieved by the use of the robot Jacobian. The proposed method is applicable to any mechanism without the need for force sensor and dynamic equations. The method is implemented on a novel 3-degrees-of-freedom (DOF) parallel robotic surgical wrist mechanism that is designed for high dexterity and force/torque estimation.

4.1. Inverse Dynamics Calculation by Neural Networks

Among many other emerging applications, Neural Networks (NN) are used in the control of nonlinear systems through learning and approximation of nonlinear functions. The dynamic model of the wrist mechanism is nonlinear due to internal coupling forces, friction and gravity, and has uncertain system parameters. For this reason, NN is utilized for the system identification using Levenberg-Marquard (LM) algorithm with a dynamic neural network.

For the NN, the number of input neurons has been selected as 6 which are position and velocity measurements of each motor, respectively and 20 neurons have been chosen in the hidden layer. In output layer, 3 output neurons have been selected whose outputs correspond to the dynamic forces of the mechanism as seen from the actuators in joint space. Initial weights and biases have been randomly selected in the beginning. To train network and update weight and bias values, Levenberg-Marquard optimization function has been used as it is one of the fastest back-propagation algorithms.

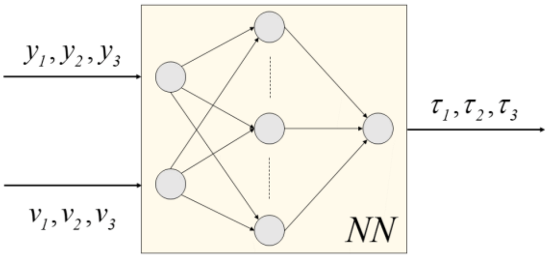

Figure 4.1. Neural Network model

To create training data, the wrist mechanism is unilaterally tele-manipulated by a 3-DOF Novint Falcon robot by providing different pose references and velocities in free space and disturbance values are obtained for each motor to find a suitable network. The states of the actuators (motor positions and velocities) which are the inputs of the predictor model and disturbance forces which are the target outputs are recorded in real time with a sampling frequency of 1 kHz. Figure 4.1 presents the general neural network model which shows inputs and outputs for the wrist. The relationship between inputs and outputs can be seen as an unknown nonlinear function in Fig 4.2. In figure 4.2, x and y axes show velocity and position measurements, respectively and the color scale presents disturbance forces acting on the linear motors.

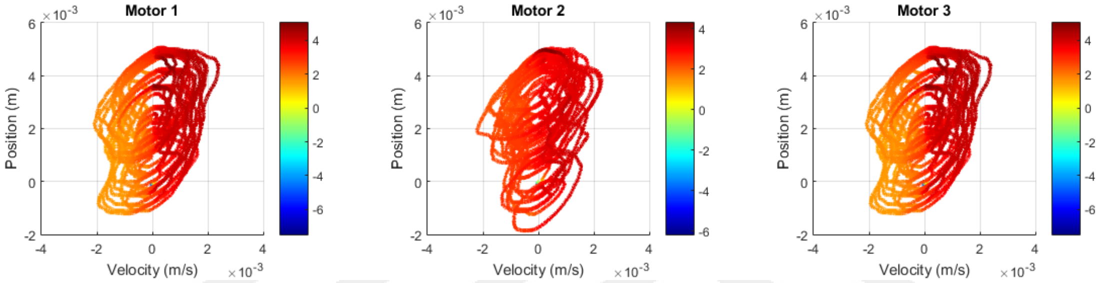

Figure 4.2. Disturbances related to states

The generalized dynamic equation of motion for the manipulator written in Joint-space is

$$M(q)\ddot{q}+C(q,\dot{q})+G(q)+\tau_{ext}=\tau \tag{4.1}$$

where q, $\dot{q}$, $\ddot{q}$ are the vectors of joint position, velocity and acceleration, respectively, $M(q)$ is the mass matrix, $C(q,\dot{q})$ is the vector of Coriolis and centrifugal forces, $G(q)$ denotes the gravity vector, τ_{ext} is the vector of external forces and τ represents the vector of forces exerted on the actuators. During the development of training data, τ_{ext} is not applied on the system and τ represents the internal dynamic force when τ_{ext} equals to 0.

4.2. Reaction Force Observer

A reaction force observer [19] is used to find external forces acting on a robot manipulator. In a conventional reaction force observer nonlinear effects such as friction forces and coupling forces are obtained with constant velocity tests and are filtered out from the total disturbance estimate. Here, instead of utilizing constant velocity tests, neural network is utilized for more robust and accurate inverse dynamics compensation. The proposed combination of DOBS, RFOB, and NN is shown in Fig.4.3. The external forces F_{ext} are extracted from total disturbance forces, by subtracting friction $f(\dot{q})$, interactive τ_{int} (a combination of inertial, centrifugal and Coriolis force), gravitational $G(q)$ forces:

$$\tau_{ext} = \tau_{dis} - \tau_{\text{int}} - \mathrm{f}(\dot{q}) - G(q) - (M - M_n)\ddot{q} - (K_{tn} - K_t)I_a^{ref} \tag{4.2}$$

It is assumed that nominal values of M_n and K_{tn} are equal to the real values of M and K_t. (4.2) becomes,

$$\tau_{ext} = \tau_{dis} - \tau_{\text{int}} - \mathrm{f}(\dot{q}) - G(q) \tag{4.3}$$

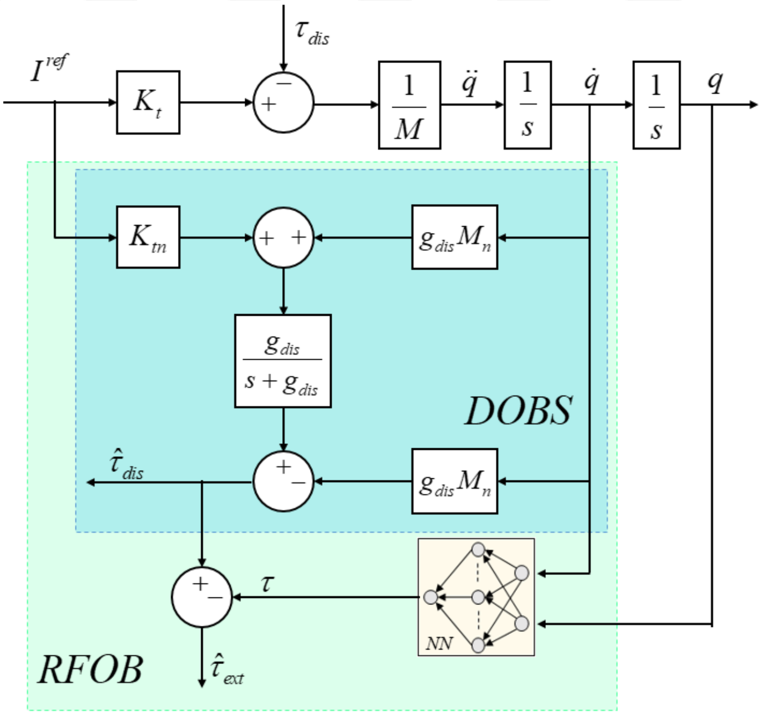
τ_{dis}
I^{ref}
K_t
$-$
$+$
$\frac{1}{M}$
$\ddot{q}$
$\frac{1}{s}$
$\dot{q}$
$\frac{1}{s}$
q
K_{tn}
$+$ $+$
$g_{dis}M_n$
$\frac{g_{dis}}{s+g_{dis}}$
DOBS
$\hat{\tau}_{dis}$
$+$
$-$
$g_{dis}M_n$
$+$
$-$
τ
NN
RFOB
$\hat{\tau}_{ext}$

Figure 4.3. Disturbance observer and reaction force observer model including Neural Network

In this method, the disturbances approximated by the Neural Network are subtracted from the total disturbance estimate to obtain external forces acting on the linear motors as shown in (4.3). With NN estimation output:

$$\tau = \tau_{\text{int}} + \mathrm{f}(\dot{q}) + G(q) \tag{4.4}$$

(4.3) becomes,

$$\tau_{ext} = \tau_{dis} - \tau \tag{4.5}$$

Thus, the external joint forces τ_{ext} can be estimated by applying a low pass filter with a cut-off frequency g_{reac},

$$\hat{\tau}_{ext} = \frac{g_{reac}}{s + g_{reac}}\left(I_a^{ref} K_{tn} + g_{reac} M_n q\right) - g_{reac} M_n \dot{q} \tag{4.6}$$

where $\hat{\tau}_{ext}$ is the estimate of τ_{ext}.

Finally, the estimated external forces F_{ext} exerted on the end-effector of the wrist are found by premultiplying joint forces by the inverse of the Jacobian transpose,

$$\hat{F}_{ext} = J^{-T} \hat{\tau}_{ext} \tag{4.7}$$

Then, the dynamics of the wrist in Cartesian space can be expressed by premultiplying (4.1) by the inverse of the Jacobian transpose,

$$J^{-T} M(q)\ddot{q} + J^{-T} C(q,\dot{q}) + J^{-T} G(q) + F_{ext} = F \tag{4.8}$$

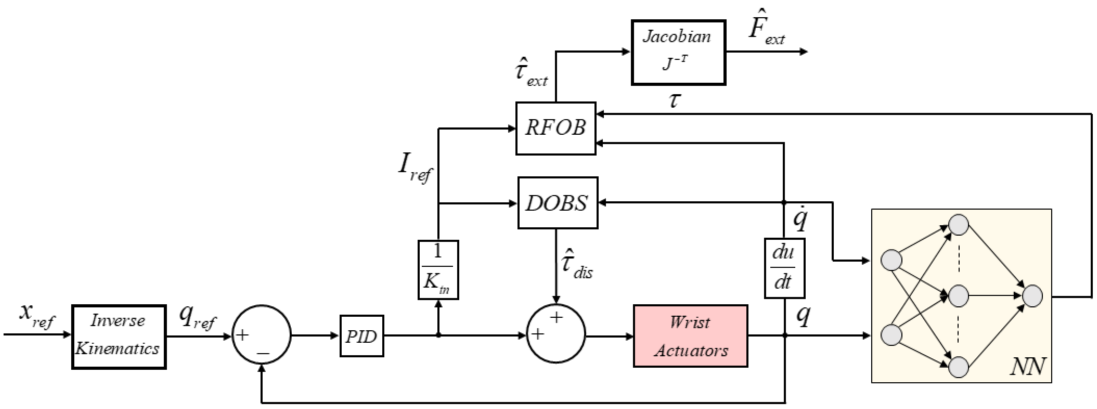
Jacobian J^{-T}
$\hat{F}_{ext}$
$\hat{\tau}_{ext}$
τ
RFOB
I_{ref}
DOBS
$\dot{q}$
$\frac{1}{K_{tn}}$
$\hat{\tau}_{dis}$
$\frac{du}{dt}$
x_{ref}
Inverse Kinematics
q_{ref}
+
−
PID
+
+
Wrist Actuators
q
NN

Figure 4.4. The sensorless control architecture of 3-DOF wrist force estimation

4.3. Force Estimation Experiments and Results

Performed experiments using the proposed force estimation method are explained. The experiment system consists of 3-DOF wrist excluding gripper mechanism as a slave manipulator and 3-DOF Novint Falcon robot as a master manipulator. The wrist mechanism is actuated with 3 linear brushless DC motors: STA 1104 by Dunkermotoren with integrated hall sensor for position measurement. Motors are connected to drivers which operate in current control mode. DAQ cards (NI-6321e) are utilized to send analog reference signals to motor drivers and read encoder signals of the motors. Control system and required functions which include kinematic and Jacobian equations were created using Matlab/Simulink and the Data Acquisition Toolbox which allows acquisition data from sensors and outputting signals to devices in real time. Master robot (Novint Falcon) is interfaced to the system through C++ library. The communication between two robots was achieved over Ethernet using UDP communication. Since each system was not started at the same time, all experiment results were plotted after 7 seconds. The specification of the control system of the wrist and the parameters used in the experiments are shown in Table 4.1.

The end-effector of the wrist does 2 rotational motions (pitch and yaw) and a thrust motion (r) whereas Falcon robot does translational motion. Therefore, transformation and scaling were required between the motion ranges of both robots. x, y, z axes of Falcon robot were transformed to r, α and β, respectively.

Table 4.1. Parameters used in control system

Parameter	Value	Parameter	Value
P	1200	$\boldsymbol{M_n}$	0.3 kg
D	3	$\boldsymbol{K_{tn}}$	5.42 N/Arms
$\boldsymbol{g_{dis}}$	1000 rad/s	$\boldsymbol{g_{reac}}$	1000 rad/s

In order; free space manipulation, contact force, force sensor validation and tumor detection experiment setups are seen in Fig 4.5-7(a) and Fig.4.8. The corresponding results for the experiments can be seen in Fig 4.5-7(b,c,d) and Fig.4.9, respectively. Figure 4.5-7(b) show disturbance observer outputs (blue), neural network outputs (red) and the difference between them (dashed green), which are the external force estimates, for each motor. As a result of manual operation, the master manipulator tool position response and wrist tool position/orientation response, which is calculated using the forward kinematics equations, are compared in Fig. 4.5-7(d). Also, the external force/torques exerted on the end-effector of the wrist are seen in Fig. 4.5-7(c). The notations of T_a, T_b and F_r are torques in α and β and the force in r axis, respectively.

In the experiments excluding free-motion experiment, forces up to 3N in thrust axis and torques up to 0.03Nm in yaw axis were applied on the wrist end-effector. Table 4.2 shows the root mean square of errors in tool force/torques over the duration of free-space manipulation and force sensor experiments.

4.3.1. Free Motion

In the free-motion experiment, the wrist was moved to different position/orientations without any contact to an environment to see the zero external force estimate on the wrist in free motion.

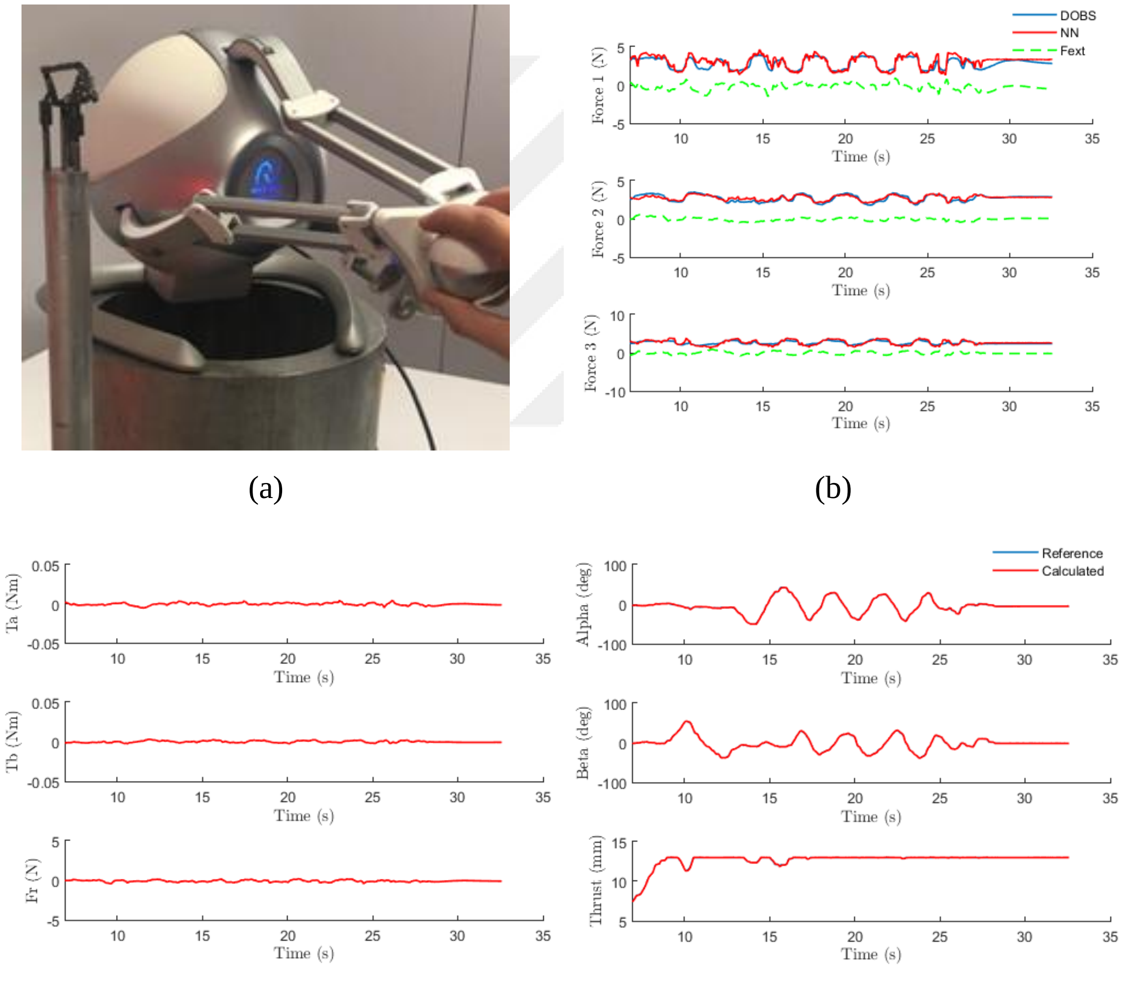

(a) (b)

(c) (d)

Figure 4.5. Free motion experiment (a) Experiment setup (b) Comparison of DOBS, NN and external forces in JS (c) End-effector force/torques in CS (d) End-effector position/orientation in CS

It can be seen that disturbance observer and neural network force estimation results are very close to each other with a small error which is illustrated with green dashed line for each motor in Fig.4.5(b). The external force exerted on the end-effector of the wrist should ideally be zero when there is no contact with environment. As illustrated in Fig.4.5(c), the estimated external force is close to zero with RMS error values of 0.0016Nm in α, 0.0011Nm in β and 0.1423N in radial axis (Table.4.2). Also, it is clear from Fig.4.5(d) that the robot followed commanded path as desired in Cartesian space.

4.3.2. Contact Force in β axis

The contact force experiment was conducted using an obstacle which is white foam in β axis (Fig.4.6(a)). For this experiment, the wrist was moved in all axes randomly and then contacted a white foam in β axis.

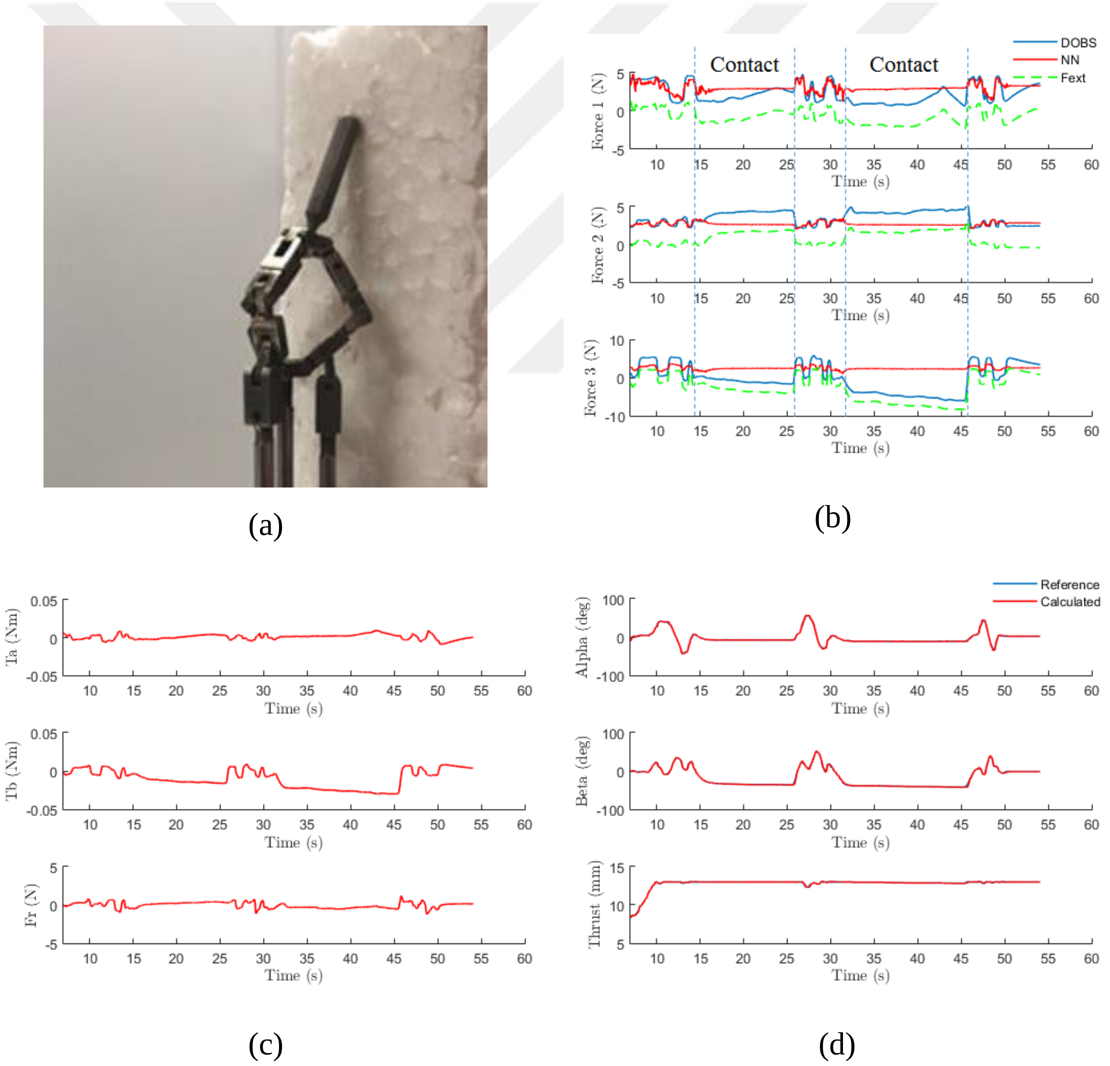

(a) (b)

(c) (d)

Figure 4.6. Contact force experiment in beta axis (a) Experiment setup (b) Comparison of DOBS, NN and external forces in JS (c) End-effector force/torques in CS (d) End-effector position/orientation in CS

As can be seen from Fig.4.6(b), external force estimate is close to zero in joint-space when there is no contact and external force changes during contact. Fig.4.6(d) shows that position tracking is achieved in Cartesian space. Besides, it can be seen that only external torque in β axis changes during contact motion in Fig.4.6(c).

4.3.3. Validation using Force Sensor

The experiment was performed in thrust axis to validate the proposed estimation method by comparing it with a reference force sensor. To provide actual force/torque measurements in Cartesian space, a force sensor (ATI/Schunk Delta SI-330-30 with resolution of 1/16N in F_x and F_y, 1/8N in F_z, 5/1333Nm in τ_x, τ_y and τ_z) was fixed to a platform vertically as in Fig.4.7(a).

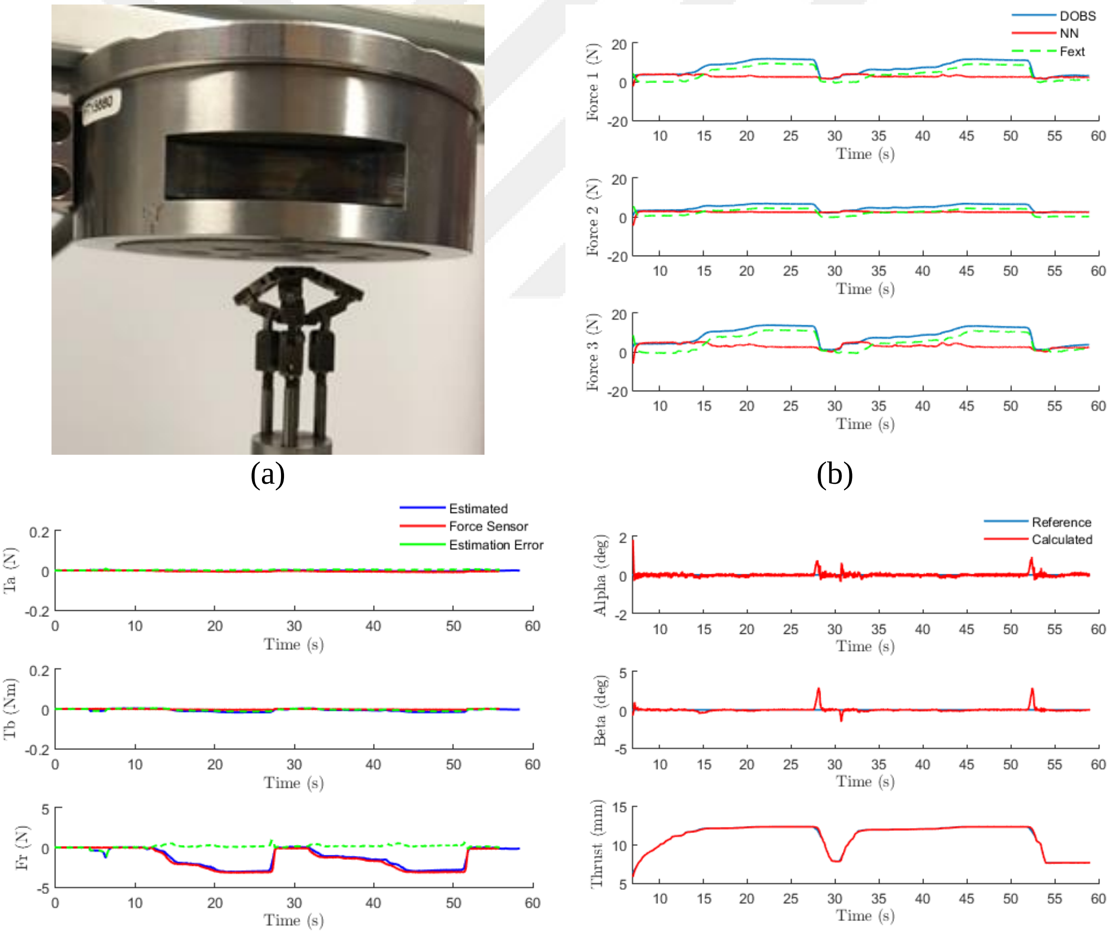

(a) (b)

(c) (d)

Figure 4.7. Validation using force sensor (a) Experiment setup (b) Comparison of DOBS, NN and external forces in JS (c) End-effector force/torques in CS (d) End-effector position/orientation in CS

Fig.4.7(b) shows the measured and estimated forces when the wrist platform contacts the force sensor in its thrust axis and it is clear that the estimated forces/torques which are obtained by the proposed method are almost equal to actual forces/torques with RMS error values of 0.0031Nm in α, 0.0075 Nm in β and 0.2309N in radial axis (Table 4.2)

4.3.4. Tumor Detection

Another experiment which is similar to [14,17] was performed is to detect a phantom tumor in a phantom intestine by touching 4 different points which can be seen in Fig.4.8 and comparing the stiffness values. An object which has high stiffness value was embedded as tumor at the 3rd point.

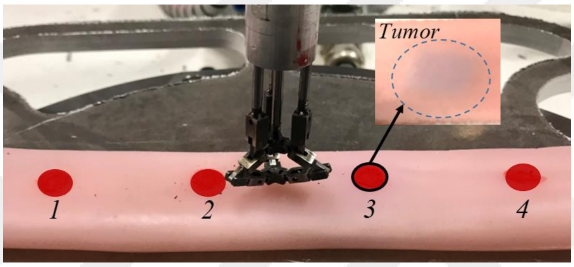

Figure 4.8. Tumor detection experiment setup

During experiments, thrust length and force data in thrust axis of the wrist were recorded and are shown in Fig.4.9. In the beginning, external force is zero and force increases when the end-effector of the wrist starts to touch the artificial organ. Slope, obtained by regression represents the stiffness values for each point.

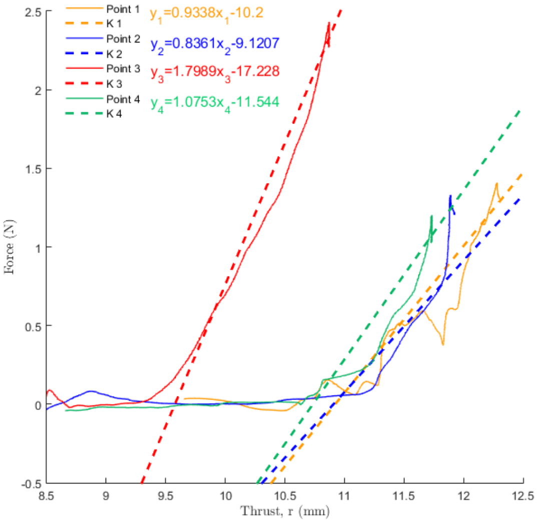

Figure 4.9. Experiment result of the stiffness determination in thrust axis

Tumor can be distinguished by a higher stiffness that can be seen from the force/displacement slopes. Therefore, it is seen that the highest stiffness value is at the 3rd point (with slope value of 1.7989).

Table 4.2. RMS error values in force data

Experiments	**T_a (Nm)**	**T_b (Nm)**	**F_r (N)**
Free Space	0.0016	0.0011	0.1423
Force Sensor	0.0031	0.0075	0.2309

5. FORCE ESTIMATION ALGORITHM ON A 7-DOF SURGICAL ROBOT

This section describes the force estimation algorithm of a 7-DOF surgical robot that was designed within the scope of the TUBITAK project titled “Design and Development of a Robotic Forceps with Force Feedback Capability for Minimally Invasive Surgery” (Project ID: 115E712) and it has been completed with a collaboration of a team from Bahçeşehir University and Marmara University. The main contribution in this thesis is to implement the idea explained in Section 4 on a 7-DOF surgical robot and to derive force/torque transformations between both robots.

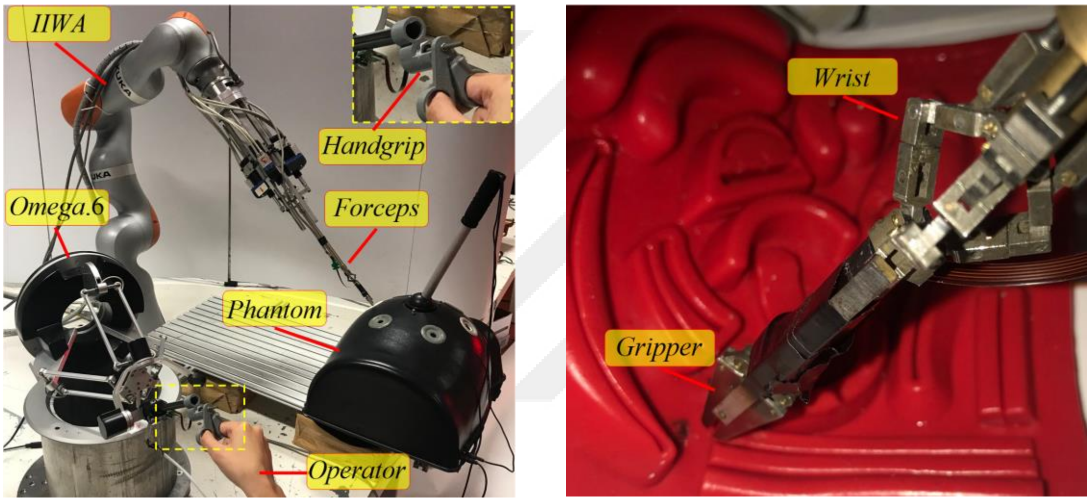

(a) (b)

Figure 5.1. 7-DOF surgical robot system (a) Overview of the system (b) Inside the phantom

5.1. The Surgical Robot System Overview

The whole surgical robot system can be seen in Fig.5.1 and consists of 3 main parts: master, slave manipulators and control and communication system that sends and receives position and force signals.

5.1.1. Slave Side

Slave manipulator makes use of a novel surgical robot system [27] that is a combination of a novel wrist mechanism first proposed in [26] and presented in Section 2 of this thesis and 7-DOF Kuka IIWA LBR7 R800 robot. Detailed design and the kinematic analysis can be found in [27].

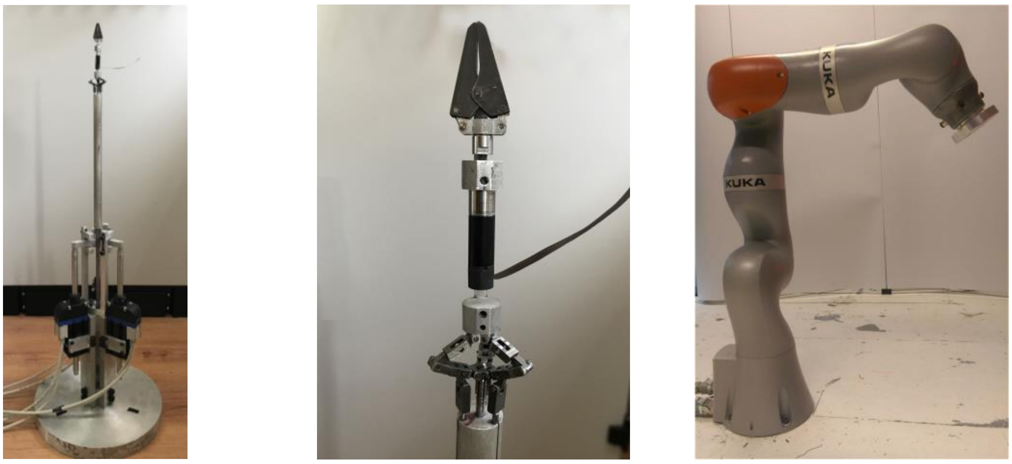

(a) (b) (c)

Figure 5.2. Elements of the slave manipulator (a,b) 4-DOF forceps mechanism (c) IIWA manipulator

a) 4-DOF Parallel Wrist Mechanism

For the purpose of doing intra-corporeal bending and gripping motions inside body in a surgery, a 4-DOF robotic forceps mechanism which is explained in Section 2 is utilized.

b) The Kuka IIWA 7 R800 Robot

The redundant IIWA manipulator is used to provide the remote center of motion (RCM) to locate the wrist mechanism as desired. The robot controller is set to joint position control mode. Given the robot's end-effector transformation, the joint space trajectory of IIWA is determined analytically and commanded via the built-in UDP based interface: FRI (Fast Robot Interface).

5.1.2. Master Side

Master manipulator makes use of a 1-DOF handgrip mechanism and 6-DOF Omega.6 manipulator (Fig.5.3). The handgrip was produced using 3D printer and connected serially to the stylus of Omega.6.

a) Omega.6

Omega.6 is a parallel robotic mechanism with a 3-R type wrist mounted on top of it. The parallel mechanism is actuated with tendon-driven joints to provide both the Cartesian translational motion in addition to translational haptic feedback. On the other hand, the wrist is merely serial chain of three encoders that is not actively actuated hence, it only captures the commanded orientation. The Haptic SDK and Robotic SDK are two C++

based libraries that represent the software interface of the device whereas the physical interface of the device is USB.

b) Handgrip

The handgrip is a simple mechanism consisting of stationary and revolutionary jaws to control the opening and closing motions of the gripper on the slave manipulator. It is actuated by a spindle drive motor and gripping motion is provided by the rotational motion of the motor.

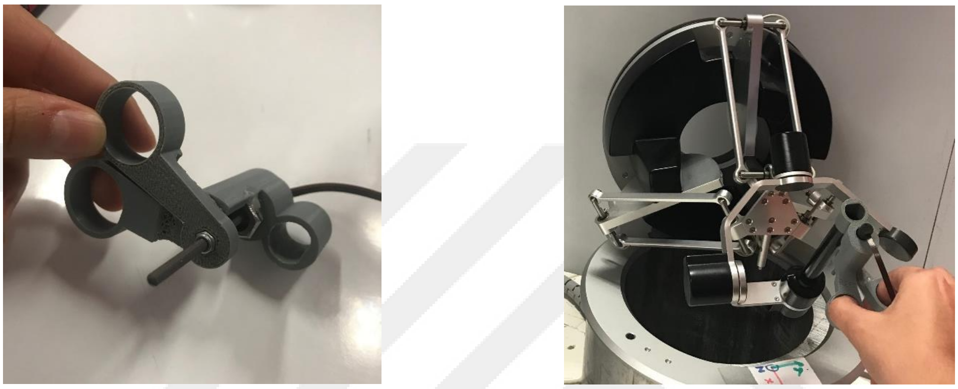

(a) (b)

Figure 5.3. Elements of the master manipulator (a) Handgrip mechanism (b) 7-DOF master manipulator

5.1.3. Communication System

Referring to Fig.5.4, the system consists of two subsystems that are handling real-time communication with the hardware. The division is based on the programming interface of system components.

- PC-1: This subsystem handles bidirectional communication with the haptic device Omega.6, the RCOM manipulator IIWA, and the force/torque sensor. The interface of this system is C++based.
- PC-2: This subsystem handles the bidirectional communication with the forceps, handgrip, and gripper. The interface of this system is Matlab/Simulink based.

Both two subsystems communicate with each other through a UDP based Client-Server model implemented on PC-1 and PC-2, respectively. The communication on subsystem level for PC-1 is handled by a shared memory segment where each process can write and read from. For example, the haptic device writes the commanded position and orientation and reads the contact forces. On the other hand, PC-2 subsystem drives the motors of the wrist mechanism and gripper and handgrip and also reads the encoder signals from these motors. In addition, it handles the computations regarding kinematics and force estimation. This subsystem is entirely based on the Quarc real-time control software [37].

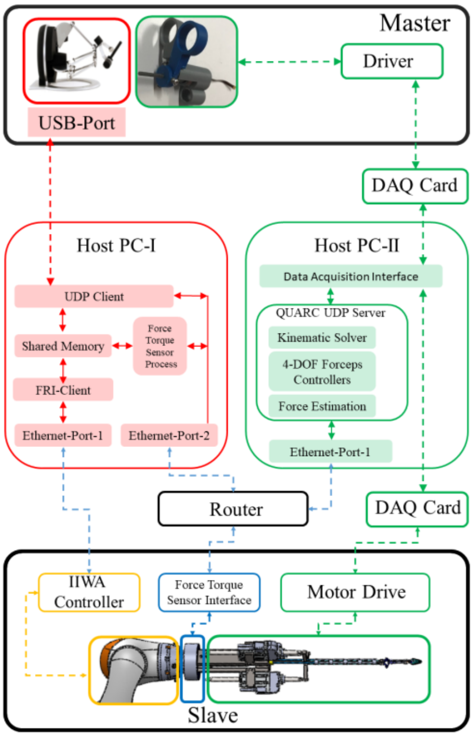
Master
Driver
USB-Port
DAQ Card
Host PC-I
UDP Client
Shared Memory
Force Torque Sensor Process
FRI-Client
Ethernet-Port-1
Ethernet-Port-2
Host PC-II
Data Acquisition Interface
QUARC UDP Server
Kinematic Solver
4-DOF Forceps Controllers
Force Estimation
Ethernet-Port-1
Router
DAQ Card
IIWA Controller
Force Torque Sensor Interface
Motor Drive
Slave

Figure 5.4. Control system architecture among forceps, handgrip, Omega.6, IIWA and the force sensor interfaces

5.2. Force Estimation Process

During operation, disturbance forces of the wrist change since the position of the forceps changes when IIWA moves. Thus, wrist mechanism is trained considering the IIWA position $\{x, y, z\}_{IIWA}$, self-positions and velocities $\{q, \dot{q}\}_{wrist}$ of wrist motors for 7-DOF force estimation to provide the wrist to learn disturbance forces in different locations by using the collected data. This procedure is realized and external forces acting on the wrist end-effector $\{\tau_{\alpha}, \tau_{\beta}\}_{wrist}$ are calculated in “Wrist Force Estimation Block” in Fig.5.5 with the same principle explained in Section 4.

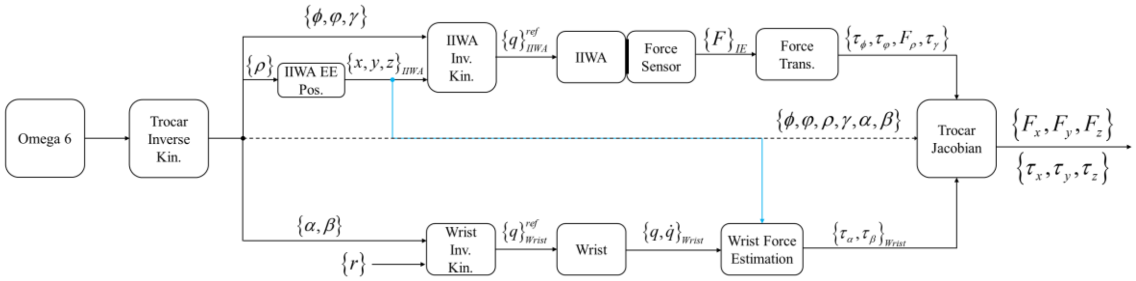
Omega 6
Trocar Inverse Kin.
$\{\phi,\varphi,\gamma\}$
$\{\rho\}$
IIWA EE Pos.
$\{x,y,z\}_{IIWA}$
IIWA Inv. Kin.
$\{q\}_{IIWA}^{ref}$
IIWA
Force Sensor
$\{F\}_{IE}$
Force Trans.
$\{\tau_\phi,\tau_\varphi,F_\rho,\tau_\gamma\}$
$\{\phi,\varphi,\rho,\gamma,\alpha,\beta\}$
Trocar Jacobian
$\{F_x,F_y,F_z\}$
$\{\tau_x,\tau_y,\tau_z\}$
$\{\alpha,\beta\}$
$\{r\}$
Wrist Inv. Kin.
$\{q\}_{Wrist}^{ref}$
Wrist
$\{q,\dot{q}\}_{Wrist}$
Wrist Force Estimation
$\{\tau_\alpha,\tau_\beta\}_{Wrist}$

Figure 5.5. Control system of the surgical robot system

Using trocar inverse kinematics based on the “Virtual Laparoscopic Robotic Instrument” method, reference position for the surgical robot coming from Omega.6 is transformed into commands for both IIWA $\{\phi,\psi,\rho,\gamma\}$ and wrist manipulators $\{\alpha,\beta\}$. With the self-control systems of each robot, it is provided that robots track desired path depending on the computed command signal. Finally, the required IIWA end-effector forces and the estimated wrist forces with trocar robot variables are sent to “Trocar Jacobian” block and end-effector forces of the 7-DOF surgical robot are calculated. The whole force estimation algorithm is explained in detail in Section 5.3.

5.3. Force Estimation Algorithm

The relationship between joint and Cartesian space forces and torques for an n link manipulator is given by

$$\tau = {}^{n}J\left(q\right)^{T}\ {}^{n}F \tag{5.1}$$

where J defines Jacobian matrix of the manipulator that converts force/torques acting on end-effector to joint space, q is the joint position variables , τ represents force/torques exerted on joints and F denotes end-effector forces in Cartesian space.

6×6 Jacobian matrix of the surgical robot excluding grasping axis is generated through relations between joint and Cartesian space velocities. By only adding a frame to the end-effector and using the same principle with “Virtual Laparoscopic Surgical Instrument”, which provides reducing total degrees of freedom of the combination of 7-DOF IIWA manipulator and the 4-DOF wrist mechanism to 6 [27], Jacobian matrix is found by means of JS and CS velocity relations that are $\dot{q}$ and v, respectively :

$$v = J\left(q\right)\dot{q} \tag{5.2}$$

For this purpose, the velocity of each link can be calculated by propagating them iteratively from the robot base to end-effector. The angular velocity and the linear velocity of the link $\{i+1\}$ are calculated with respect to frame $\{i+1\}$ depending on joint type:

- If joint $\{i+1\}$ is revolute,

$$ {}^{i+1}\omega_{i+1} = {}^{i+1}_{i}R\,{}^{i}\omega_{i} + \dot{\theta}_{i+1}\,{}^{i+1}\hat{Z}_{i+1} \tag{5.3} $$

$$ {}^{i+1}v_{i+1} = {}^{i+1}_{i}R\left({}^{i}v_{i} + {}^{i}\omega_{i} \times {}^{i}P_{i+1}\right) \tag{5.4} $$

- If joint $\{i+1\}$ is prismatic,

$$ {}^{i+1}\omega_{i+1} = {}^{i+1}_{i}R\,{}^{i}\omega_{i} \tag{5.5} $$

$$ {}^{i+1}v_{i+1} = {}^{i+1}_{i}R\left({}^{i}v_{i} + {}^{i}\omega_{i} \times {}^{i}P_{i+1}\right) + \dot{d}_{i+1}\,{}^{i+1}\hat{Z}_{i+1} \tag{5.6} $$

To compute force/torques acting on the end-effector of the surgical robot, joint force/torques of the virtual trocar robot which consists of IIWA end-effector and 4-DOF wrist forces and torques are required and they are defined as a vector,

$$ \tau = \begin{bmatrix} \tau_{\phi} & \tau_{\psi} & F_{\rho} & \tau_{\gamma} & \tau_{\alpha} & \tau_{\beta} \end{bmatrix}^{T} \tag{5.7} $$

Here, whereas $\tau_{0-4} = \begin{bmatrix} \tau_{\phi} & \tau_{\psi} & F_{\rho} & \tau_{\gamma} \end{bmatrix}^{T}$ is provided by IIWA, τ_{α} and τ_{β} are provided by the integrated robotic wrist.

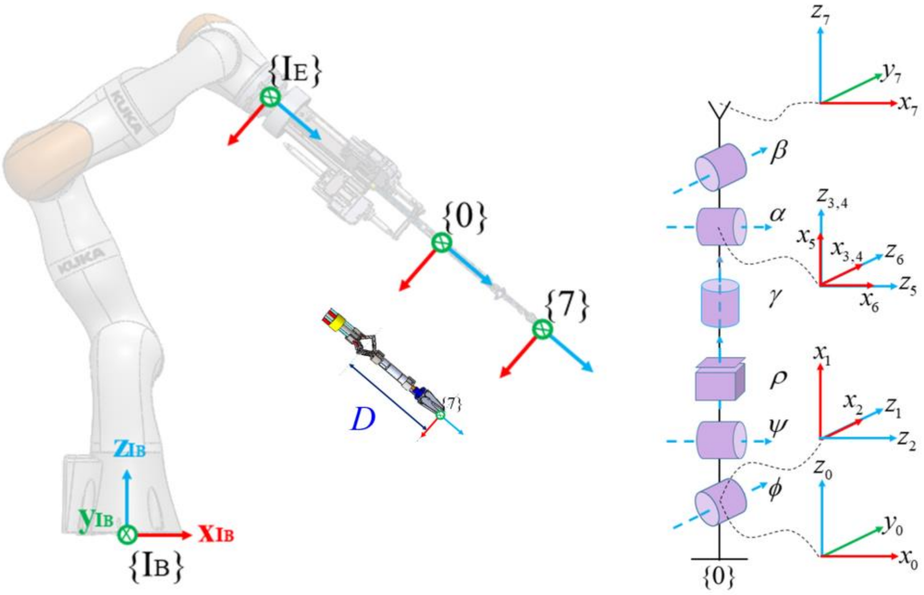

Figure 5.6. Frame assignment of the 7-DOF surgical robot

Let ${}^{j}_{i}T$ be the transformation matrix, which transforms the description in $\{i\}$ frame to $\{j\}$ frame. Further, for necessary transformations in force estimation, I_B , I_E , 0 , 4 and 7 are defined as the IIWA base and IIWA end-effector coordinate frames, trocar frame, 4^{th} and 7^{th} frames of the virtual trocar robot, respectively as seen in Fig.4.

Table 5.1. DH parameters of the 6-DOF Virtual Trocar Method

i	θ_i	d_i	α_{i-1}	a_{i-1}
1	$-\pi/2+\phi$	0	$-\pi/2$	0
2	$-\pi/2+\psi$	0	$-\pi/2$	0
3	0	ρ	$-\pi/2$	0
4	γ	0	0	0
5	$\pi/2+\alpha$	0	$\pi/2$	0
6	$\pi/2+\beta$	0	$\pi/2$	0
7	0	D	$\pi/2$	0

Due to the fact that torque sensors on IIWA's joint are not sensitive enough, parameters in dynamic analysis of IIWA are not able to be determined exactly and IIWA cannot compensate forceps weight so that this problem affects force estimation algorithm. For this reason, 6-DOF force sensor is mounted to the place between IIWA end-effector and forceps mechanism. Thus, force/torques exerted on the IIWA end-effector are measured by the aid of this sensor.

Since 6×1 IIWA Cartesian force-torque vector acting on the end-effector $\left({}^{I_E}F\right)$ is calculated using force sensor with respect to its own frame that is coincident with the IIWA end-effector frame $\left(I_E\right)$, 6×1 force vector ${}^{I_E}F$ written in terms of I_E is transformed into $\{4\}$ multiplying by 6×6 transformation matrix for the purpose of computing the first trocar robot joint force and torques,

$$ {}^{4}F = \begin{bmatrix} {}^{4}_{I_E}R & 0 \\ {}^{4}P_{I_E ORG} \times {}^{4}_{I_E}R & {}^{4}_{I_E}R \end{bmatrix} {}^{I_E}F \tag{5.8} $$

where the cross product is understood to be the matrix operator:

$$ {}^{4}P_{I_E ORG} = \begin{bmatrix} 0 & -{}^{4}P_{I_E ORG\,z} & {}^{4}P_{I_E ORG\,y} \\ {}^{4}P_{I_E ORG\,z} & 0 & -{}^{4}P_{I_E ORG\,z} \\ -{}^{4}P_{I_E ORG\,y} & {}^{4}P_{I_E ORG\,x} & 0 \end{bmatrix} \tag{5.9} $$

and (5.8) maybe written compactly as

$$ {}^{4}F = {}^{4}_{I_E}\mathbf{T}\,{}^{I_E}F \tag{5.10} $$

Here, ${}^{4}_{I_E}\mathbf{T}$ is 6×6 force-torque transformation matrix and ${}^{4}_{I_E}R$ seen in (5.8) is a rotation part 4×4 transformation matrix which is expressed as products of transformations,

$$ {}^{4}_{I_E}T = {}^{4}_{0}T\,{}^{0}_{I_E}T \tag{5.11} $$

In (5.11), ${}^{4}_{0}T$ is calculated using DH parameters given in Table 5.1 and ${}^{0}_{I_E}T$ can be computed by:

$$ {}^{0}_{I_E}T = \left({}^{I_B}_{0}T\right)^{-1}\,{}^{I_B}_{I_E}T \tag{5.12} $$

with ${}^{I_B}_{I_E}T$ in (5.12) representing a transformation matrix composed by IIWA DH-parameters and a constant transformation matrix ${}^{I_B}_{0}T$ depending on angles at initial configuration of the IIWA.

Therefore, to find the joint torques and force acting on the first 4-DOFs $\left(\tau_{0-4} = \begin{bmatrix} \tau_{\phi} & \tau_{\psi} & F_{\rho} & \tau_{\gamma} \end{bmatrix}^{T}\right)$, ${}^{4}F$ vector found in (5.10) is multiplied by the Jacobian transpose with respect to $\{4\}$.

$$ \tau_{0-4} = \left({}^{4}J\right)^{T}\,{}^{4}F \tag{5.13} $$

where ${}^{4}J$ is a 6×4 Jacobian matrix that is described as

$$ {}^{4}J = \begin{bmatrix} -\rho c\psi s\gamma & -\rho c\gamma & 0 & 0 \\ -\rho c\psi c\gamma & \rho s\gamma & 0 & 0 \\ 0 & 0 & 1 & 0 \\ c\psi c\gamma & -s\gamma & 0 & 0 \\ -c\psi s\gamma & -c\gamma & 0 & 0 \\ -s\psi & 0 & 0 & 1 \end{bmatrix} \tag{5.14} $$

Finally, the virtual trocar robot end-effector force vector $\left({}^{7}F\right)$ is found by using the

Jacobian that can be seen in (5.16) written in frame $\{7\}$,

$$ {}^{7}F = \left({}^{7}J^{-T}\right)\tau \tag{5.15} $$

where τ includes both $\tau_{0-4} = \begin{bmatrix} \tau_\phi & \tau_\psi & F_\rho & \tau_\gamma \end{bmatrix}^T$ and the estimated wrist torques acting on the wrist end-effector that are τ_α and τ_β.

$$ {}^{7}J = \begin{bmatrix} \rho\left(-c_\psi s_\gamma s_\alpha s_\beta + c_\psi c_\gamma c_\beta\right) + D\left(c_\psi c_\gamma c_\alpha - s_\psi s_\alpha\right) & -\rho\left(c_\gamma s_\alpha s_\beta + s_\gamma c_\beta\right) - D s_\gamma c_\alpha & -c_\alpha s_\beta & D s_\alpha & 0 & D \\ -\rho c_\psi s_\gamma c_\alpha - D\left(c_\psi c_\gamma s_\alpha s_\beta + c_\psi s_\gamma c_\beta + s_\psi c_\alpha s_\beta\right) & -\rho c_\gamma c_\alpha + D\left(s_\gamma s_\alpha s_\beta - c_\gamma c_\beta\right) & s_\alpha & D c_\alpha s_\beta & -D c_\beta & 0 \\ \rho\left(c_\psi s_\gamma s_\alpha c_\beta + c_\psi c_\gamma s_\beta\right) & \rho\left(c_\gamma s_\alpha c_\beta - s_\gamma s_\beta\right) & c_\alpha c_\beta & 0 & 0 & 0 \\ c_\psi c_\gamma s_\alpha s_\beta + s_\psi c_\alpha s_\beta + c_\psi s_\gamma c_\beta & -s_\gamma s_\alpha s_\beta + c_\gamma c_\beta & 0 & -c_\alpha s_\beta & c_\beta & 0 \\ c_\psi c_\gamma c_\alpha - s_\psi s_\alpha s_\beta & -s_\gamma c_\alpha & 0 & s_\alpha & 0 & 1 \\ -c_\psi c_\gamma s_\alpha c_\beta - s_\gamma c_\alpha c_\beta + c_\psi s_\gamma s_\beta & s_\gamma s_\alpha c_\beta + c_\gamma s_\beta & 0 & c_\alpha c_\beta & s_\beta & 0 \end{bmatrix} \tag{5.16} $$

5.4. Force Estimation Experiments and Results

5.4.1. Validation of Forces and Torques in –x, –y, –z axes

For the purpose of validation force/torque estimates on 6-DOF surgical robot system, a 1-DOF force sensor (Burster 8524) for the forces in x, y, z axes (Fig.5.7) and uniform objects whose weights are known for the torques were used as seen in Fig.5.8. Each validation experiment was carried out separately. In the beginning of the experiments performed using force sensor, end-point of the robot was in contact with the force sensor and a small motion was given in the direction of validation axis after starting to the experiment. Then, the force value coming from sensor and the estimated value were compared. In torque validation experiments, uniform object whose mass is 0.05 kg was hanged to the end-effector of the robot in x and y axes as seen in Fig.5.8(a,b). The mass causes a torque at the center of the wrist so that the last frame $\{7\}$ on the robot was moved to the center of the wrist mechanism for the validation and the estimated torque and applied torque were compared at that point.

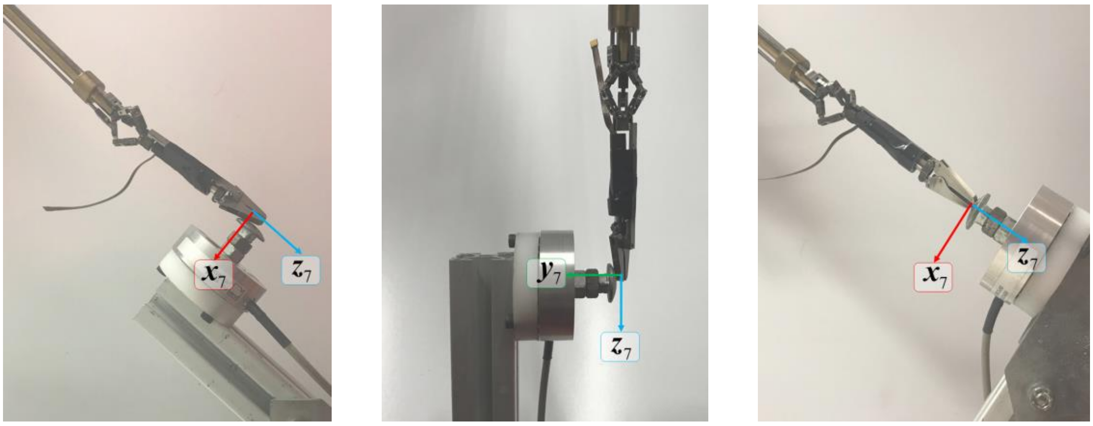

(a) (b) (c)

Figure 5.7. Experiment setup for force validations (a) Fx (b) Fy (c) Fz

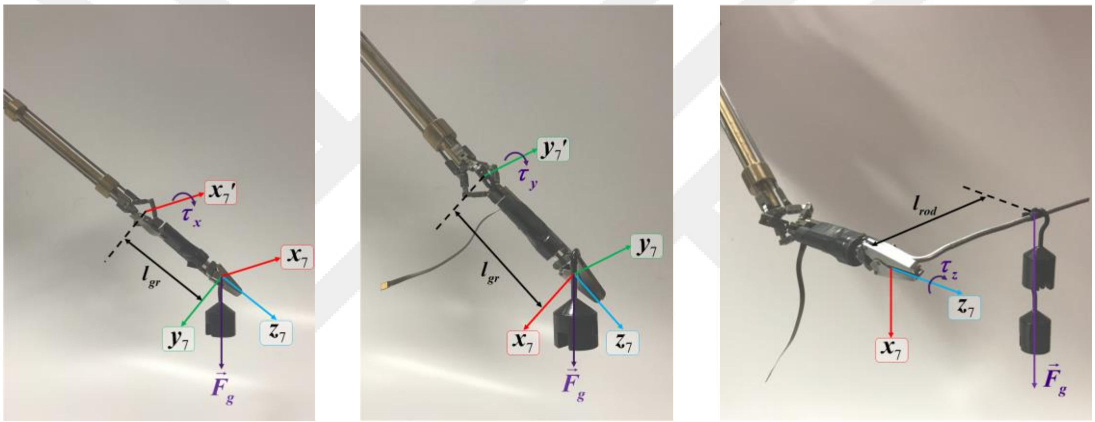

(a) (b) (c)

Figure 5.8. Experiment setup for torque validations (a) Nx (b) Ny (c) Nz

For the validation in z axis, a thin rod was mounded to the end-point of the robot and a 0.04kg mass was hanged at a distance of 7cm from the starting point of the rod as seen in Fig.5.8(c). Thus, it is provided that torque was generated as a result of this process in z axis and the estimated torque and the computed torque were compared.

Table 5.2 shows trocar robot joint variables regarding to robot position during validation experiments. As can be seen from experiment results, force and torque estimations are realized with overachievement (Fig.5.9). Root mean square of error values in force validations are less than 0.1N and in torque validations are less than 0.01Nm (Table 5.3).

Table 5.2. Trocar robot joint variables during experiments

Experiment	ϕ	ψ	ρ	γ	α	β
Fx	0^o	0^o	$0.083m$	0^o	0^o	0^o
Fy	0^o	0^o	$0.083m$	0^o	0^o	0^o
Fz	0^o	0^o	$0.083m$	0^o	0^o	0^o
Nx	0^o	0^o	$0.083m$	-90^o	0^o	0^o
Ny	0^o	0^o	$0.083m$	0^o	0^o	0^o
Nz	0^o	0^o	$0.083m$	0^o	0^o	-45^o

Table 5.3. RMS error values in force/torque validation experiments

Force/Torque	**Fx (N)**	**Fy (N)**	**Fz (N)**	**Nx (Nm)**	**Ny (Nm)**	**Nz (Nm)**
RMS error	0.0450	0.0083	0.0637	0.0009	0.0018	0.007

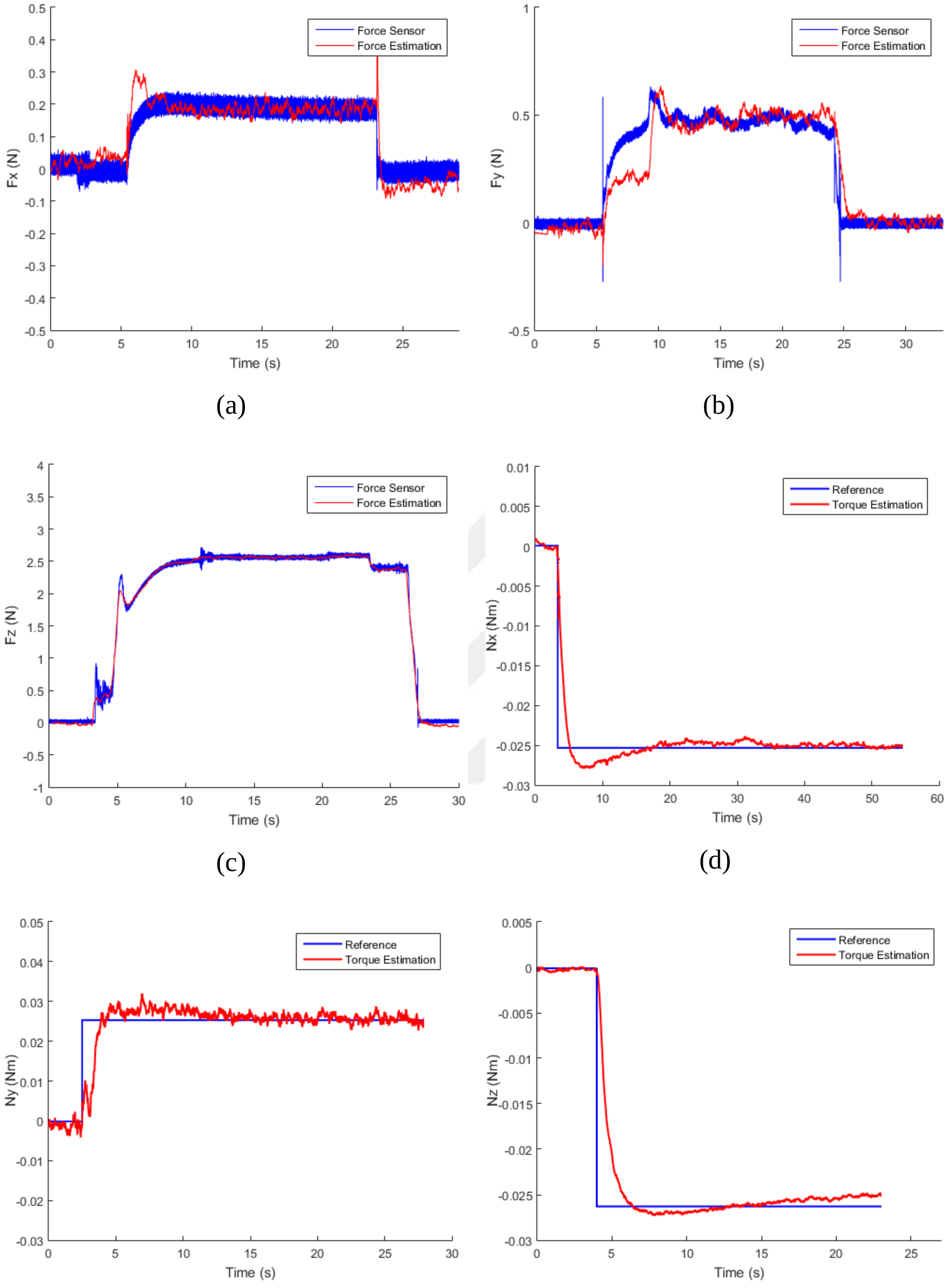

(a) (b)

(c) (d)

(e) (f)

Figure 5.9. Force/torque validation results (a) Fx (b) Fy (c) Fz (d) Nx (e) Ny (d) Nz

5.4.2. Palpation Experiment inside the Phantom

Using the experiment setup shown in Fig.5.1, palpation experiment was performed with an artificial organ which was located inside the phantom. The goal in this experiment is to observe end-effector forces and torques in each axis except gripping axis while the surgical robot touches to a point on the organ. The robot was moved with a small motion unilaterally and contacted with a point. In this experiment, estimated forces could not be validated due to the lack of the 6-DOF force sensor and only position and force changes are presented in Fig.5.10 during unilateral teleoperation. According to results, external force estimates are close to zero when there is no contact but it is observed that forces increase when the robot is in contact with an environment (Fig.5.10(c,d)). Also, it can be seen that translational and angular positions did not change during contact in Fig.5.10(a,b).

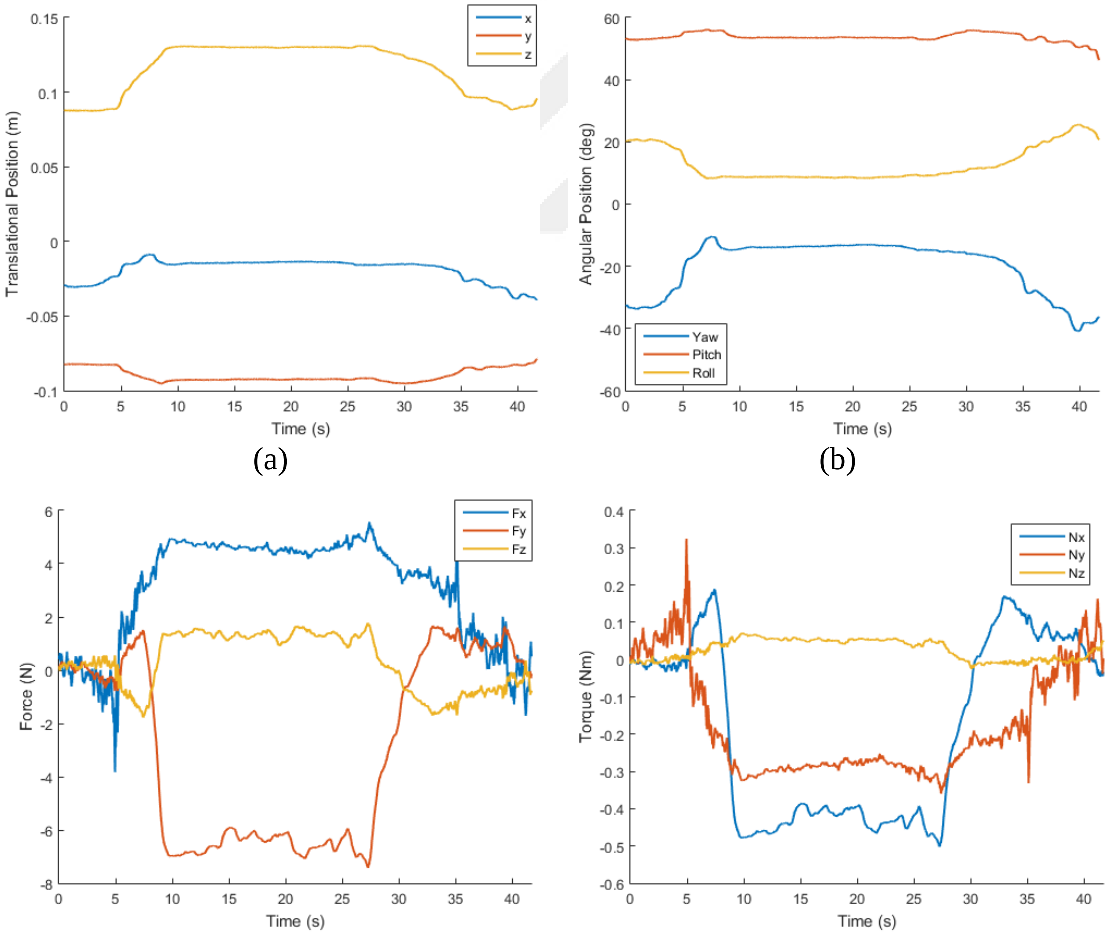

(a) (b)

(c) (d)

Figure 5.10. Force/torque validation results (a) Translational Position (b) Angular Position (c) Forces in x, y, z axes (d) Torques in x, y, z axes

5.4.3. Gripping Axis

In this experiment, the gripper mechanism was bilaterally teleoperated by the handgrip. Experiment setup is shown in Fig.5.11. In the beginning, the gripper was moved in free-space and it can be seen that external force is zero during this motion. Then, a pink foam was grasped between 6 and 11 seconds and in that period, external force increased up to the time when a pink foam was released. Position and force responses are seen in Fig.5.12. According to experiment results, position control of the gripper was achieved in free-motion. However, the estimate force reflected to the operator cannot be felt exactly because of the weakness of the spindle drive. For this reason, it is seen that gripper did not keep at the same position when operator tried to move handgrip during contact.

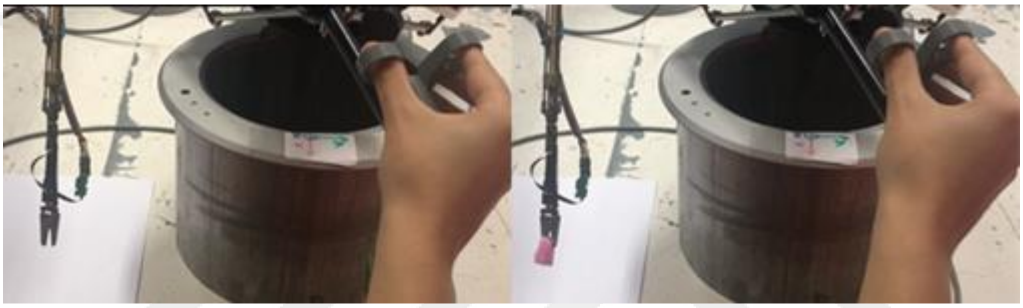

Figure 5.11. Palpation experiment setup in gripping axis

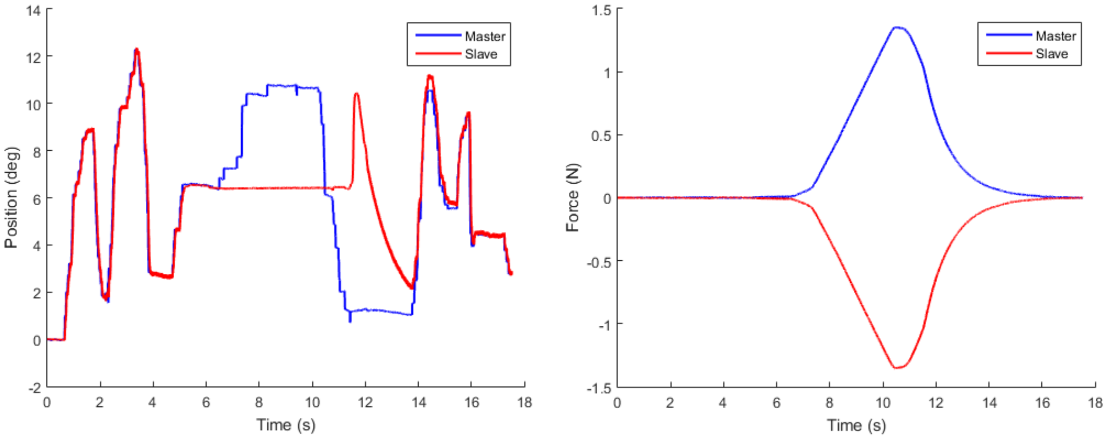

(a) (b)

Figure 5.12. Gripping axis (a) Position response (b) Force response

The force validation on this axis could not be done due to the lack of the proper force sensor but this experiment shows that it is possible to perform bilateral teleoperation with this setup.

6. BILATERAL TELEOPERATION SYSTEMS FOR ROBOTIC SURGERY

A bilateral teleoperation system consists of master and slave manipulators and controllers between these manipulators. A human operator controls a master manipulator to drive slave robot and a slave robot is in contact with an unknown environment. To provide haptic feedback to the operator, the important thing is that it is possible to realize sensorless teleoperation between manipulators using neural network based reaction force observer even if the system dynamics is unknown. In this study, bilateral teleoperation systems were designed using the proposed force estimation algorithm composed of DOBS, NN and RFOB and applied on Phantom Omni haptic device which can be used in minimally invasive surgery. Also, the same teleoperation system was designed by means of computed torque method which is composed of dynamic equations of the manipulators. At the end of this study, experiment results of both systems are compared to each other.

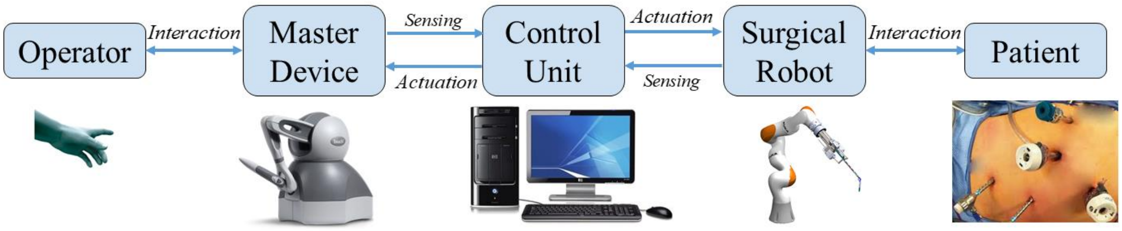

Figure 6.1. Bilateral teleoperation system for a surgical robot

6.1. Phantom Omni

2 Phantom Omni haptic devices as a master and slave robot are utilized to design teleoperation system with the haptic feedback. Phantom Omni mainly is a 6-DOF serial manipulator whereas the first 3 joints of this device are active and the last 3 wrist joints are passive. For this reason, the teleoperation system is realized using only active joints of the robots in this real-time study.

The communication system utilizes USB interface that allows real time programming via the OpenHaptics toolkit based on C++ and robots are able to be connected directly to OpenHaptics through predefined haptic Simulink library called as “PhanTorque” that uses S-functions. Therefore, kinematic analysis and developed control algorithms are implemented in Matlab/Simulink.

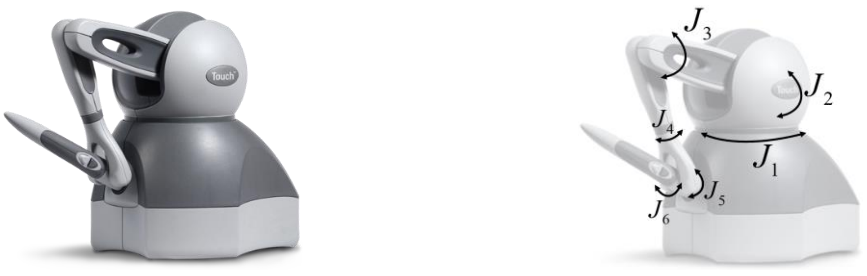

(a) (b)

Figure 6.2. Phantom Omni robot (a) General view (b) Representation of joints

6.1.1. Position and Velocity Kinematics

Forward kinematic equations are derived based on the joint angles using the modified DH-parameters that are given in Table 6.1 for the first 3 joint. In Table 6.1, θ_1^* means the first joint position reading in negative direction which is $\theta_1^* = -\theta_1$ and θ_3^* is defined as a function of 2nd and 3rd joint position readings from encoders which is $\theta_3^* = \frac{3\pi}{2} - \theta_2 + \theta_3$ with respect to reference frames on real robot. According to frame assignment as shown in Fig. 6.3., transformation matrix from base to end-effector frame has been found:

$$ {}^0_4T = \begin{bmatrix} c_{23}c_1 & -s_{23}c_1 & -s_1 & c_1\left(a_4c_{23}+a_3c_2\right) \\ -c_{23}s_1 & s_{23}s_1 & -c_1 & -s_1\left(a_4c_{23}+a_3c_2\right) \\ s_{23} & c_{23} & 0 & d_1+a_4s_{23}+a_3s_2 \\ 0 & 0 & 0 & 1 \end{bmatrix} \tag{6.1}$$

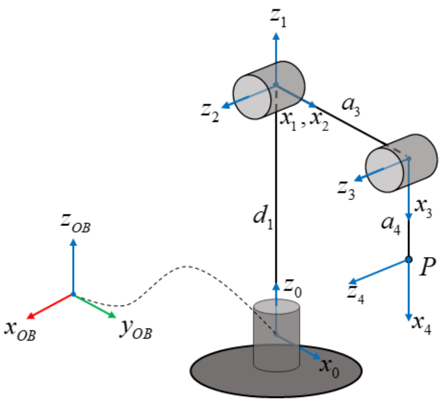

Figure 6.3. Representation of DH parameters of the first 3-DOF of Phantom Omni

However, the frame located at base is different in real robot so the chosen zeroth frame needs to be transformed to obtain the same position data in x, y, z axes from the ready Simulink blocks regarding to real robot. For this reason, (6.1) is premultiplied by $T_z\left(\pi/2\right)$ transformation matrix.

$$
{}^{OB}_{4}T = T_z\left(\pi/2\right){}^{0}_{4}T = \begin{bmatrix} c_{23}s_1 & -s_{23}s_1 & c_1 & s_1\left(a_4c_{23}+a_3c_2\right) \\ c_{23}c_1 & -s_{23}c_1 & -s_1 & c_1\left(a_4c_{23}+a_3c_2\right) \\ s_{23} & c_{23} & 0 & d_1+a_4s_{23}+a_3s_2 \\ 0 & 0 & 0 & 1 \end{bmatrix} \tag{6.2}
$$

Here, OB defines “Omni Base” of the real robot. Then, the final column of (6.2) gives the position components of the end-effector in x, y, z axis:

$$
\begin{aligned} P_x &= s_1\left(a_4c_{23}+a_3c_2\right) \\ P_y &= c_1\left(a_4c_{23}+a_3c_2\right) \\ P_z &= d_1+a_4s_{23}+a_3s_2 \end{aligned} \tag{6.3}
$$

Table 6.1. DH parameters of the first 3-DOF of Phantom Omni

i	θ_i	d_i	α_{i-1}	a_{i-1}
1	θ_1^*	d_1	0	0
2	θ_2	0	$\pi/2$	0
3	θ_3^*	0	0	a_3
4	0	0	0	a_4

In velocity kinematics, to transform force estimations in joint-space to Cartesian space, Jacobian that gives relations between velocities in JS and CS is required and it is found by differentiating (6.1):

$$
J = \begin{bmatrix} c_1\left(a_4c_{23}+a_3c_2\right) & -s_1\left(a_4s_{23}+a_3s_2\right) & -s_1a_4s_{23} \\ -s_1\left(a_4c_{23}+a_3c_2\right) & -c_1\left(a_4s_{23}+a_3s_2\right) & -c_1a_4s_{23} \\ 0 & a_4c_{23}+a_3c_2 & a_4c_{23} \end{bmatrix} \tag{6.4}
$$

6.1.2. Force Estimation Algorithms

a) Neural Network based Reaction Force Observer

As similar to Section 4, same methodology is applied on Phantom Omni robots to estimate external forces and the estimation algorithm is a combination of disturbance observer (DOBS), neural network (NN) and reaction force observer (RFOB).

i. Disturbance Observer

Joint-space disturbance observer is used to compensate total disturbances acting on the each joint and parameters used in the observer are already defined in Section 3.1.2 Differently from previous explanations, instead of using I^{ref} , τ^{ref} is written as a multiplication of I^{ref} and K_t, which is a desired torque since the information about joint motors is unknown and the motor parameters are not known exactly. Also, $M\left(q\right)$ represents the inertia matrix because of that all joints are revolute.

Table 6.2. Inertia and cut-off frequency values of each joint

	$\boldsymbol{J}_1$	$\boldsymbol{J}_2$	$\boldsymbol{J}_3$
$\boldsymbol{I}\ (\boldsymbol{kg.m}^2)$	5.208e-4	2.126e-4	3.276e-4
$\boldsymbol{g}_{dis}(\boldsymbol{rad.s}^{-1})$	10	10	5

ii. Inverse Dynamics Model by Neural Networks

To identify system dynamics, Neural Network is utilized using an optimization function called Levenberg-Marquard (LM). This analysis is performed separately for both Phantom Omni robots and the number of input neurons has been selected as 6 which are position and velocity measurements of motors for each robot, respectively. 3 output neurons have been selected whose outputs give the dynamic forces of each joint in output layer and 20 neurons have been chosen in hidden layer.

Before training, initial weights and biases have been randomly selected and by means of LM function, network is trained and weight and bias values are updated.

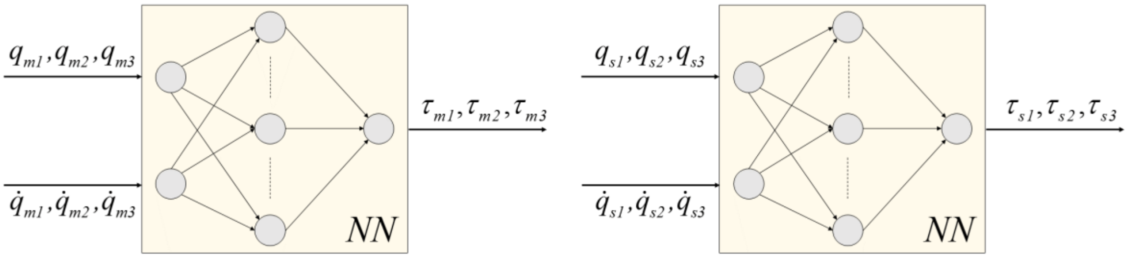
q_{m1}, q_{m2}, q_{m3}
$\dot{q}_{m1}, \dot{q}_{m2}, \dot{q}_{m3}$
$\tau_{m1}, \tau_{m2}, \tau_{m3}$
NN
q_{s1}, q_{s2}, q_{s3}
$\dot{q}_{s1}, \dot{q}_{s2}, \dot{q}_{s3}$
$\tau_{s1}, \tau_{s2}, \tau_{s3}$
NN

Figure 6.4. Neural Network model for master and slave robots

For creating training dataset, the slave manipulator is bilaterally tele-manipulated in position-position structure by the master manipulator by moving to all possible points inside the workspace to provide different pose references and velocities in free space and disturbance values are obtained for each joint in order to find a suitable network during this motion. The reason of gathering disturbances is that they are equal to internal dynamic forces of manipulators when there is no external torque acting on manipulators and τ represents the internal dynamic forces when τ_{ext} equals to 0 as in (4.1).

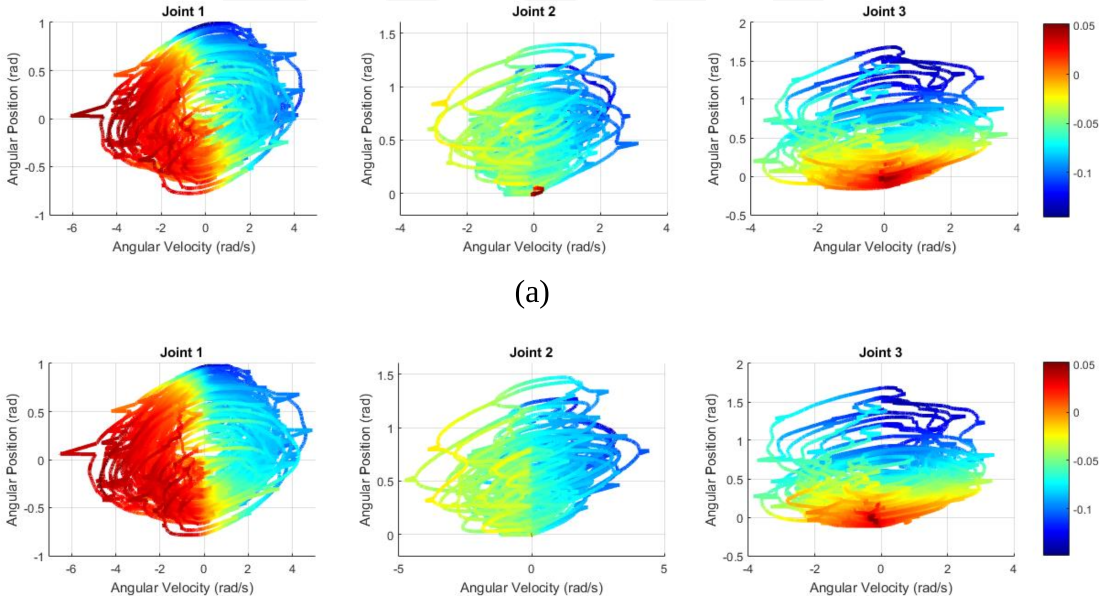

(a)

(b)

Figure 6.5. Disturbance force related to states for each joint of (a) master robot (b) slave robot

The states of the joints (motor positions and velocities) which are the inputs of the predictor model and disturbance torques which are the target outputs are recorded in real time with a sampling frequency of 1 kHz and the experiment duration for obtaining training dataset is approximately 180s. Figure 6.4 presents the general neural network model which shows inputs and outputs for master and slave Phantom Omni robots. The relationship between inputs and outputs can be seen as an unknown nonlinear function in Fig.6.5. In figure 6.5, x and y axes show velocity and position measurements, respectively and the color scale presents disturbance forces acting on the linear motors. Since the robots are serial manipulators, different torque values are exerted on each joints and it can be seen that robots are moved to different positions with different velocities inside their workspaces from Fig.6.5.

Training stopped at epoch 839 that gives best validation performance with mean square error of 0.00079584 as seen in Fig.6.6(a). At that epoch, the performance and error distribution of the network can be observed through histogram error graph that is presented in Fig.6.6(b). According to the graph, the most of the errors of instances is near to zero where blue, green and red show training, validation and test, respectively.

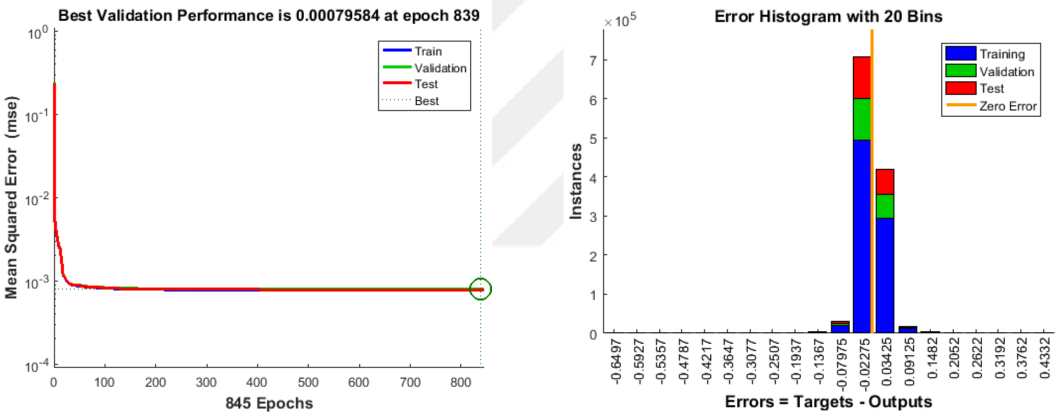

(a) (b)

Figure 6.6. Performance results of NN training (a) mean square error (b) Error histogram

In addition to error distribution, to check the performance of the network, linear regression provides a relationship between numerical input and output values that is modelled linearly and it minimizes the sum of squares of the distances between the fitted line and all of the data points. In Fig 6.7, R values for regression models illustrates how accurately observed responses of training, validation and test sets fit to regression line. It is clear that the fit is good for all data sets with R values that are close to 1 with respect to the calculated weights and biases of the network.

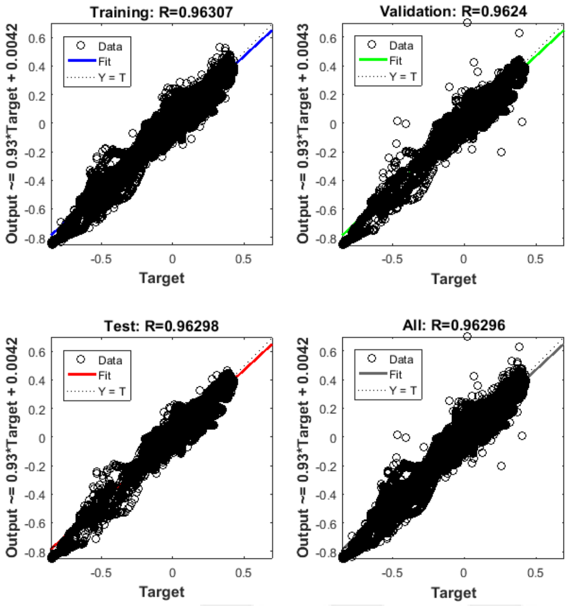

Figure 6.7. Linear regression results of NN training

iii. Reaction Force Observer

The main idea of reaction force observers (RFOB) is to isolate only external torques from disturbance forces. Instead of using inverse dynamic equations of the robot, neural network is utilized for more robust and accurate inverse dynamics compensation since the dynamic parameters of a robot manipulator changes during time and they have uncertainty. Therefore, in RFOB block, external torques are extracted from total disturbance torques which come from DOBS by subtracting dynamic torques calculated by Neural Networks that include friction, inertial, centrifugal, Coriolis and gravitational forces.

The structure of RFOB is same as in Section 4.2 and estimate external joint torques which are $\hat{\tau}_m^{ext}$ and $\hat{\tau}_s^{ext}$ are calculated as in (4.6). With the same procedure which is the premultiplication of joint torques by the inverse of the manipulator Jacobian transpose, the estimated external forces acting on the end-effector of the robot in Cartesian space are found.

Finally, the dynamics of both master and slave robots in Cartesian space can be expressed by premultiplying (4.1) by the inverse of the Jacobian transpose,

$$J^{-T}M\left(q\right)\ddot{q}+J^{-T}C\left(q,\dot{q}\right)+J^{-T}G\left(q\right)+F_{ext}=F \tag{6.5}$$

where q, $\dot{q}$, $\ddot{q}$ are the vectors of joint position, velocity and acceleration, respectively,

$M(q)$ is the inertia matrix, $C(q,\dot{q})$ is a vector of Coriolis and centrifugal forces, $G(q)$ denotes the gravity vector, F_{ext} is the vector of external forces and F represents the vector of forces exerted on the robot.

b) Computed Torque Method

Computed torque controller (CTC) is a powerful nonlinear controller which is widely used to control robot manipulators. The main idea of CTC is to implement feedback linearization so that it is also known as feedback linearization controller. In feedback linearization, a nonlinear system is transformed into an equivalent linear system by cancelling its nonlinear dynamics. Using the nonlinear feedback control law, the required torques are computed. The performance of this controller is quite high when all dynamic and physical parameters are known. However, the dynamic parameters of a robot manipulator changes during time and they have uncertainty, in this case the controller is not able to provide acceptable performance [38-39].

Generally, Lagrangian or Newton-Euler method is used to model robot’s dynamics and compute joint torques. Newton-Euler is an iterative method which includes the calculations using known mass matrix, centrifugal Coriolis and gravity vectors depending on the position, velocity and acceleration. Firstly, link velocities and accelerations are computed from first link to the last link in an iterative way and Newton-Euler equations are applied to each link. Then, interaction forces and torques and joint torques are computed recursively from the last link back to the first link. On the other hand, Lagrangian is energy based approach. Firstly, kinetic and potential energies of a manipulator are described as a function of position and velocity. Then, Lagrangian which is the difference between the kinetic and potential energy of the system is implemented. Equations derived in both methods are described with the form in (4.1).

In this study, Lagrangian method was used to derive equations of motion of Omni robots formulized in (6.6) [40]:

$$L(q,\dot{q}) = k(q,\dot{q}) - u(q) \tag{6.6}$$

where k is the total kinetic energy depending on the position and velocity and u is the total potential energy as a function of position of the manipulator. The equations of motion for the robot is described as in following formula:

$$\frac{d}{dt}\frac{\partial L}{d\dot{q}}-\frac{\partial L}{dq}=\tau \tag{6.7}$$

Here, τ is the actuator torque vector and the following equation is obtained substituting (6.6) into (6.7):

$$\frac{d}{dt}\frac{\partial k}{d\dot{q}}-\frac{\partial k}{dq}+\frac{\partial u}{dq}=\tau \tag{6.8}$$

Finally, $M(q)$, $C(q,\dot{q})$ and $G(q)$ can be obtained from (6.9) where each elements of these matrix and vectors is a complicated nonlinear functions depending on q and $\dot{q}$ in the following equation:

$$M(q)\ddot{q}+C(q,\dot{q})+G(q)=\tau \tag{6.9}$$

where $M(q)$ is the inertia matrix, $C(q,\dot{q})$ is the Coriolis and centrifugal forces vector, $G(q)$ is the gravity vector and τ is the control input torque. These matrix and vectors are computed by:

$$M(q)=\begin{bmatrix} M_{11} & M_{12} & M_{13} \\ M_{21} & M_{22} & M_{23} \\ M_{31} & M_{32} & M_{33} \end{bmatrix} \tag{6.10}$$

In (6.10), the elements of $M(q)$ are:

$$\begin{aligned}
M_{11} &= I_1+I_2+I_3+m_2a_{c_3}{}^2c_2{}^2+m_3a_3^2c_2{}^2+2m_3a_3a_{c_4}c_2c_{23}+m_3a_{c_4}{}^2c_{23}{}^2 \\
M_{12} &= I_2+I_3 \\
M_{13} &= I_3 \\
M_{21} &= I_2+I_3 \\
M_{22} &= I_2+I_3+m_2a_{c_3}{}^2+m_3a_3{}^2+m_3a_{c_4}{}^2+2m_3a_3^2a_{c_4}c_3 \\
M_{23} &= I_3+m_3a_{c_4}{}^2+m_3a_3a_{c_4}c_3 \\
M_{31} &= I_3 \\
M_{32} &= I_3+m_3a_{c_4}{}^2+m_3a_3a_{c_4}c_3 \\
M_{33} &= I_3+m_3a_{c_4}{}^2
\end{aligned} \tag{6.11}$$

where a_{c_i} is the distance from beginning to the center, I_i and m_i are the inertia and the mass values of each link.

Coriolis and centrifugal forces vector is:

$$C(q,\dot{q}) = \begin{bmatrix} -2\dot{q}_1\dot{q}_2\,\mathrm{s}_2\left(a_3{}^2 m_3 + a_3 l_3 m_3\,\mathrm{c}_{23} + l_2{}^2 m_2\right) - 4a_3 l_3 m_3 \dot{q}_1\,\mathrm{c}_{0.5q_2}{}^2\left(\dot{q}_2 + \dot{q}_3\right)\mathrm{s}_{23} \\ \dot{q}_1{}^2\,\mathrm{s}_2\,\mathrm{c}_2\left(a_3{}^2 m_3 + l_2{}^2 m_2\right) + l_3 m_3\left(\dot{q}_1{}^2\left(a_3 + 0.5 l_3\right)\mathrm{s}_{2(q_{23})} - a_3\dot{q}_3\,\mathrm{s}_3\left(2\dot{q}_2 + \dot{q}_3\right)\right) \\ l_3 m_3\left(\dot{q}_1{}^2\left(0.5a_3\,\mathrm{s}_{2q_2+q_3} + 0.5 l_3\,\mathrm{s}_{2(q_{23})}\right) + a_3\,\mathrm{s}_3\left(0.5\dot{q}_1{}^2 + \dot{q}_2{}^2\right)\right) \end{bmatrix} \quad (6.12)$$

Gravity vector is:

$$G(q) = \begin{bmatrix} 0 \\ (m_2 + m_3) l_2 g c_2 + m_3 g l_3 c_{23} \\ m_3 g l_3 c_{23} \end{bmatrix} \quad (6.13)$$

Using dynamic equations, a model-based manipulator control system was designed as seen in Fig.6.8.

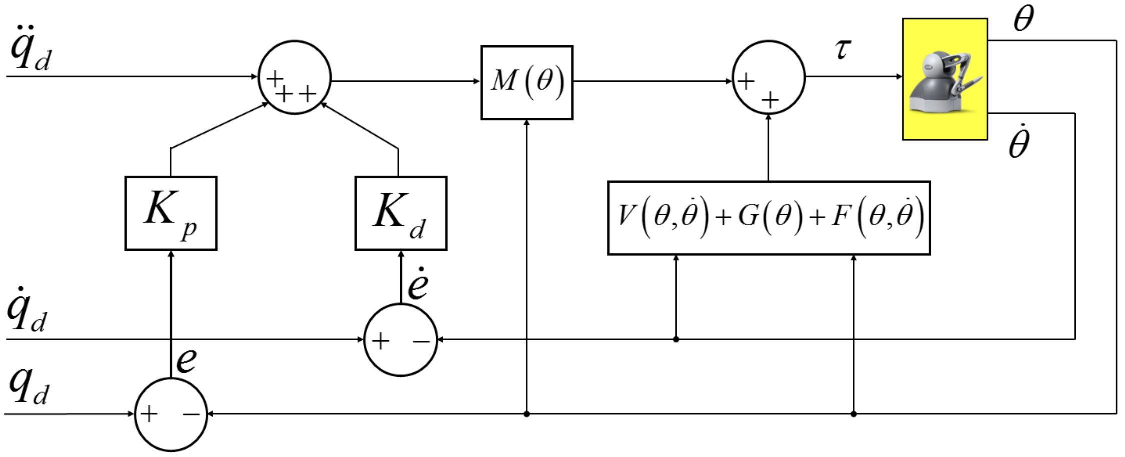

Figure 6.8. A model-based manipulator-control system

6.2. 4-Channel Bilateral Teleoperation System with NN based RFOB

A teleoperation system has to have some qualifications to provide good interaction between the master and slave robots and the system must be transparent. In this respect, an ideal bilateral teleoperation system would satisfy,

$$\begin{aligned} q_m - q_s &= 0 \\ \hat{\tau}_m^{ext} + \hat{\tau}_s^{ext} &= 0 \end{aligned} \quad (6.14)$$

where q defines joint position measurements of robots and $\hat{\tau}^{ext}$ represents external torque exerted on each joint. Superscript ext means external and subscripts m and s are abbreviations for master and slave, respectively.

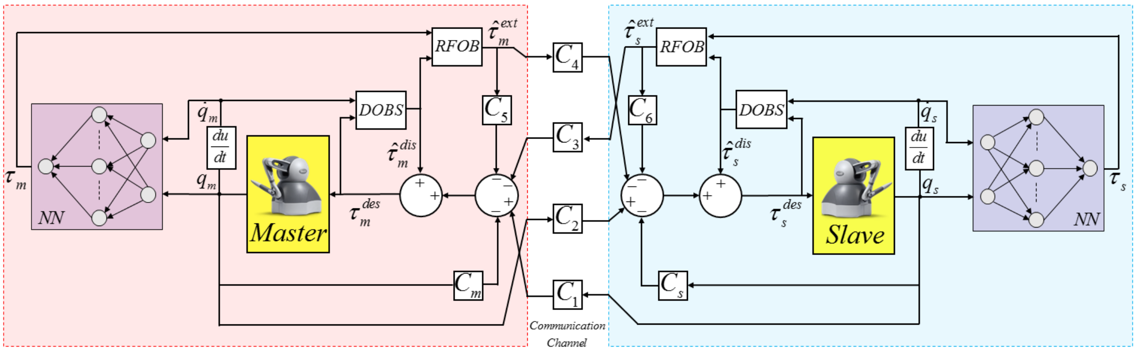
RFOB
$\hat{\tau}_m^{ext}$
DOBS
C_5
$\dot{q}_m$
$\frac{du}{dt}$
q_m
τ_m
NN
Master
$\hat{\tau}_m^{dis}$
τ_m^{des}
C_m
C_4
C_3
C_2
C_1
Communication Channel
$\hat{\tau}_s^{ext}$
RFOB
C_6
DOBS
$\hat{\tau}_s^{dis}$
τ_s^{des}
Slave
$\dot{q}_s$
$\frac{du}{dt}$
q_s
τ_s
NN
C_s

Figure 6.9. 4 channel teleoperation diagram based on Lawrence Architecture for Phantom Omni robots

4-channel Lawrence architecture consists of four communication channels between master and slave robots [41]. Two channels of them are used for exchanging of position measurements and others are for exchanging of force measurements between robots. The acceleration references of master and slave manipulators in 4-channel architecture can be written under no time delay based on general block diagram shown in Fig.6.9.,

$$\begin{aligned} \ddot{q}_m^{ref} &= C_1 q_s - C_m q_m - C_5 \hat{\tau}_m^{ext} - C_3 \hat{\tau}_s^{ext} \\ \ddot{q}_s^{ref} &= C_2 q_m - C_s q_s - C_4 \hat{\tau}_m^{ext} - C_6 \hat{\tau}_s^{ext} \end{aligned} \tag{6.15}$$

In (6.15), C_m , C_s are local position controllers, C_5 , C_6 are local force compensators, C_1 , C_2 are position, C_4 , C_5 are the force communication channels for master and slave robots, respectively.

The transparent four channel based teleoperation can be realized by choosing control parameters as:

$$\begin{aligned} C_1 = C_2 = C_m = C_s = C_P = K_p + K_d s \\ C_5 = C_3 = C_4 = C_6 = C_f = 1 \end{aligned} \tag{6.16}$$

Thus, (6.15) for each manipulator is transformed into,

$$\begin{aligned} \ddot{q}_m^{ref} &= C_P \left(q_s - q_m \right) - C_f \left(\hat{\tau}_m^{ext} + \hat{\tau}_s^{ext} \right) \\ \ddot{q}_s^{ref} &= C_P \left(q_m - q_s \right) - C_f \left(\hat{\tau}_m^{ext} + \hat{\tau}_s^{ext} \right) \end{aligned} \tag{6.17}$$

Here, C_P and C_f represent the position and force controllers, respectively. While C_P is a combination of K_p and K_d which are the PD coefficients, C_f is chosen as 1 which is a force control gain. The same controllers are used for both master and slave manipulators since they are identical and Controllers used in teleoperation system are given in Table 6.3 for each joint of robots.

Table 6.3. Position and force controllers for each joint of Phantom Omni

	J_1	J_2	J_3
K_P	6	3	2
K_d	0.08	0.12	0.03
C_f	1	1	1

6.3. Experiments and Results

The validity of the proposed reaction force observer was confirmed with experiments carried out using force sensor. The 4-channel teleoperation system was composed of two Phantom Omni haptic devices (Fig.6.10). The robots were connected to a computer through USB interface and the computer runs the control algorithm in real time in Matlab/Simulink with a sampling frequency of 1 KHz. Motor position measurements, disturbance observers and neural network based reaction force observers are utilized to suppress disturbances and estimate external forces. Computed torque method and the proposed force estimation algorithm based on Fig.6.10 have been implemented choosing controllers as mentioned in (6.16).

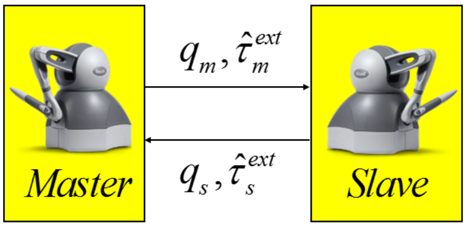

Figure 6.10. 4-channel teleoperation system between 2 haptic devices

In the experiments, the last 3 joints of the robots are fixed and their motion are restricted. Via its stylus, master robot is moved by an operator. It is allowed that a human operator can drive the slave robot that repeats movements of master robot and also contact forces are reflected to operator via master robot.

6.3.1. Validation using Force Sensor

Three experiments were performed in –x, –y, –z axes to validate the proposed estimation method by comparing its results with a force sensor during 4-channel joint-space bilateral teleoperation. To obtain actual force measurements in Cartesian space, a 1-DOF force sensor was fixed to a platform and this platform was located in –x, –y, –z axes separately as shown in Fig.6.11-13(a). All experiments were carried out three times to verify the method and in order: the master manipulator was moved in free-space and contacted with a force sensor.

- **-x axis**

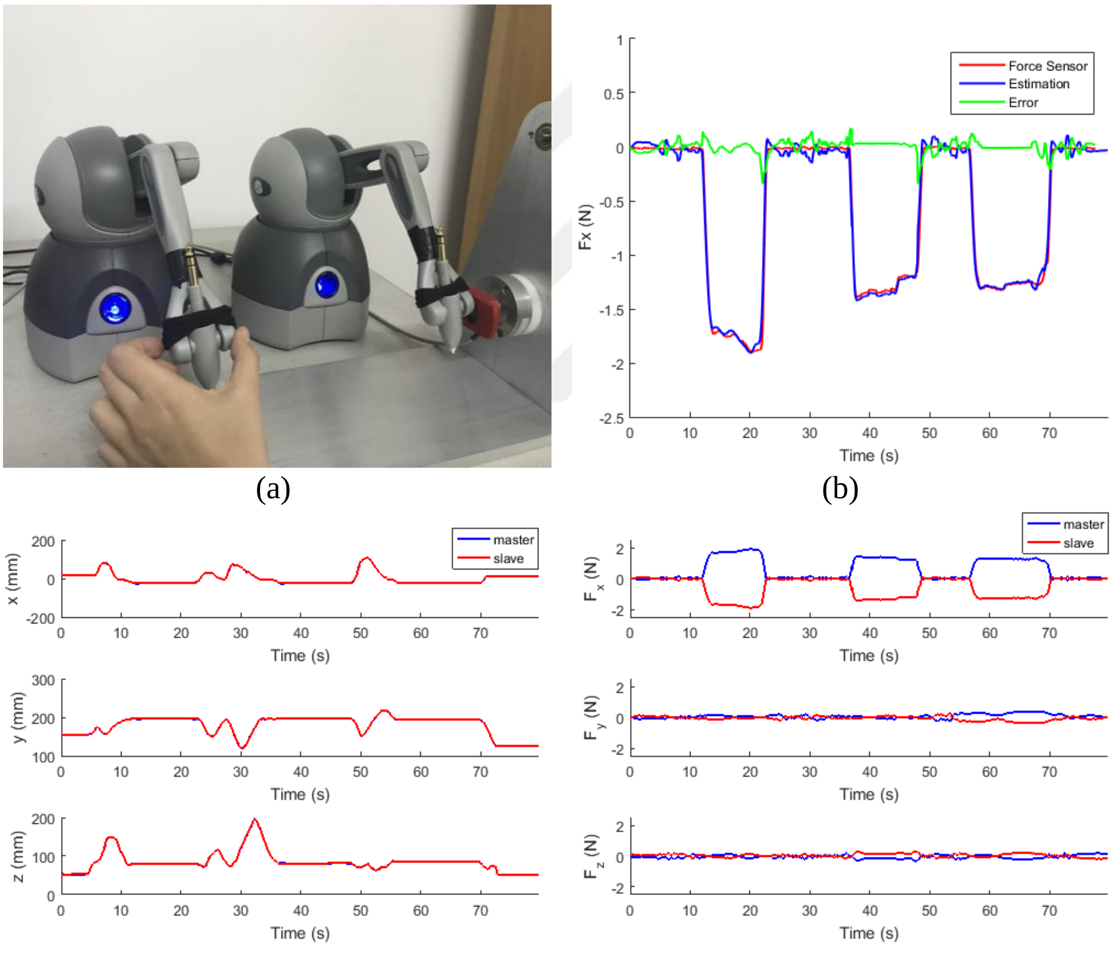

(a) (b)

(c) (d)

Figure 6.11. Bilateral teleoperation result in –x axis (a) Experiment setup (b) Comparison of estimated force and force sensor (c) Position tracking in CS (d) Force reflection in CS

Figure 6.11-13(b) shows the measured and estimated forces acting on the slave manipulator in each axis when the robot was in contact with the force sensor and it is obvious that the estimated forces which are obtained using the proposed estimation algorithm in teleoperation are almost equal to actual forces with RMS error values of 0.0597N in –x, 0.0648N in –y and 0.0720N in –z axis (Table 6.4). Besides, the slave robot followed commanded path by the master robot as desired in Cartesian space that can be seen in Fig 6.11-13(c). Also, as a result of bilateral teleoperation, external forces exerted on the slave robot were reflected directly to master robot Fig 6.11-13(d). With this result, it is achieved that the sum of the forces should be zero to confirm ideal force reflection case.

- **-y axis**

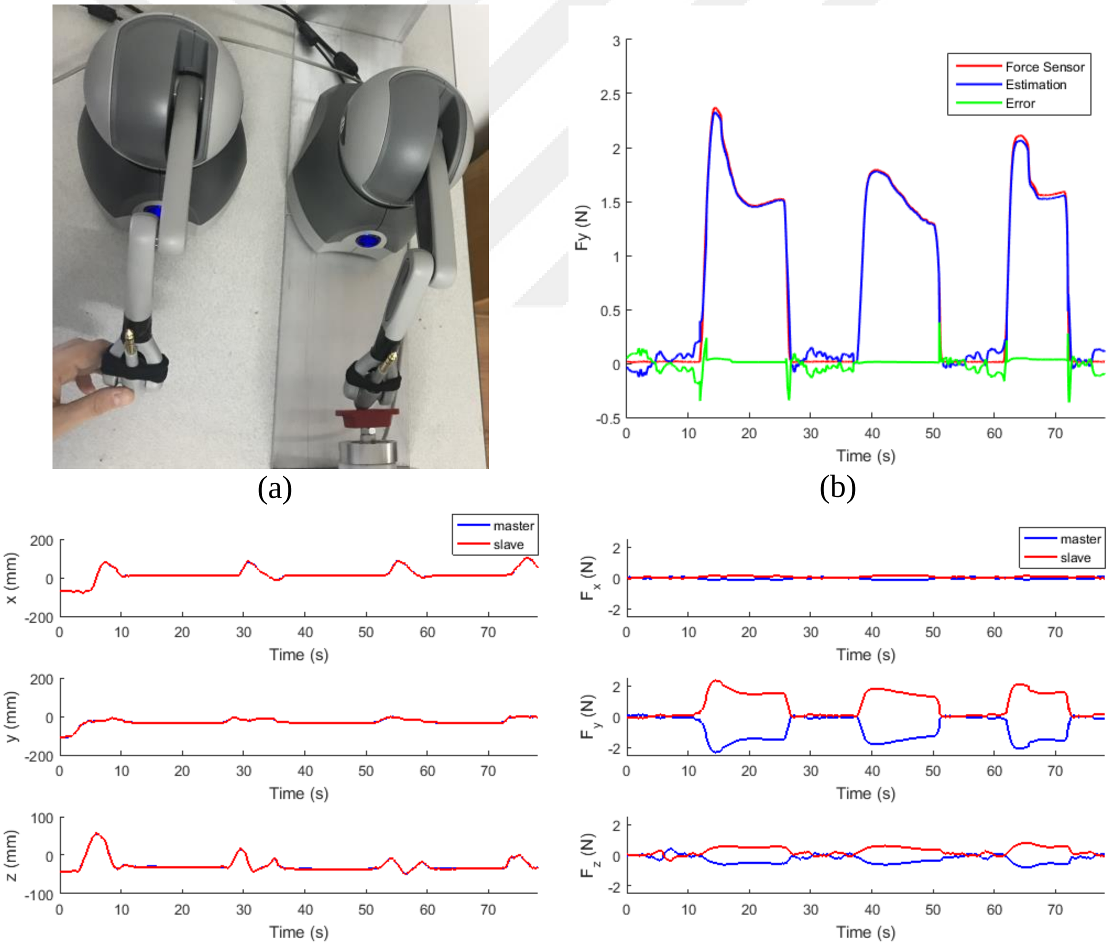

(a) (b)

(c) (d)

Figure 6.12. Bilateral teleoperation result in –y axis (a) Experiment setup (b) Comparison of estimated force and force sensor (c) Position tracking in CS (d) Force reflection in CS

- **-z axis**

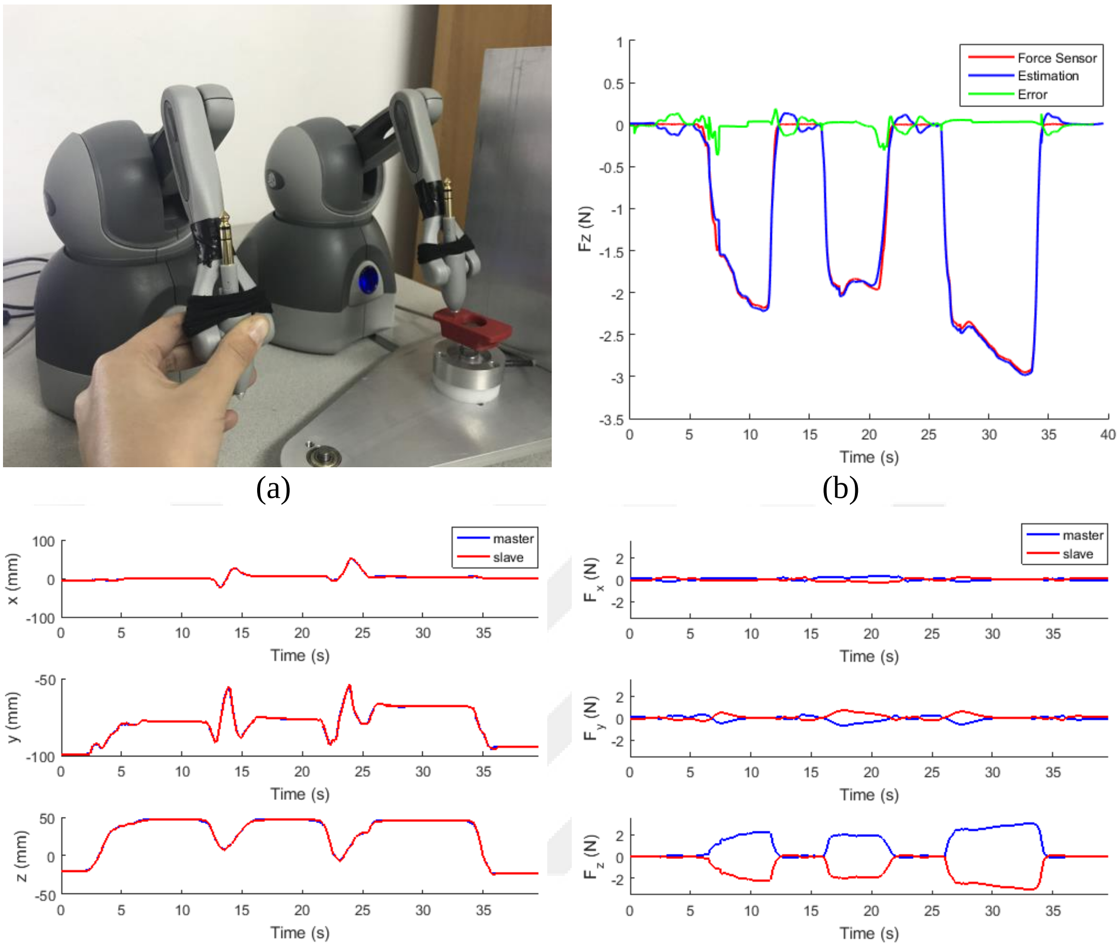

(a) (b)

(c) (d)

Figure 6.13. Bilateral teleoperation result in –z axis (a) Experiment setup (b) Comparison of estimated force and force sensor (c) Position tracking in CS (d) Force reflection in CS

Table 6.4. RMS error values in CS as a result of validation with a force sensor

RMS Error in x (N)	RMS Error in y (N)	RMS Error in z (N)
0.0597	0.0648	0.0720

6.3.2. Comparison of CTM and NNRFOB

To compare the Neural Network based Reaction Force Observer and Computed Torque Method (CTM), the slave manipulator was moved by the master robot around a specified path implementing computed torque method and the proposed method without any contact with the environment, separately and experiment setup is seen in Fig.6.14. Since there is no contact with the environment, the external force acting on the robot in Cartesian space and the external torque acting on each joint are expected to be zero. By comparing both methods, it is aimed to see which method computes dynamic forces of the robot more accurate. For this reason, the slave robot was moved in similar positions in both experiments in order to ensure that the robot has similar dynamics. Fig.6.15 shows the end-effector position outputs in x, y and z axes of the robot corresponds to experiments carried out using the proposed method and CTM.

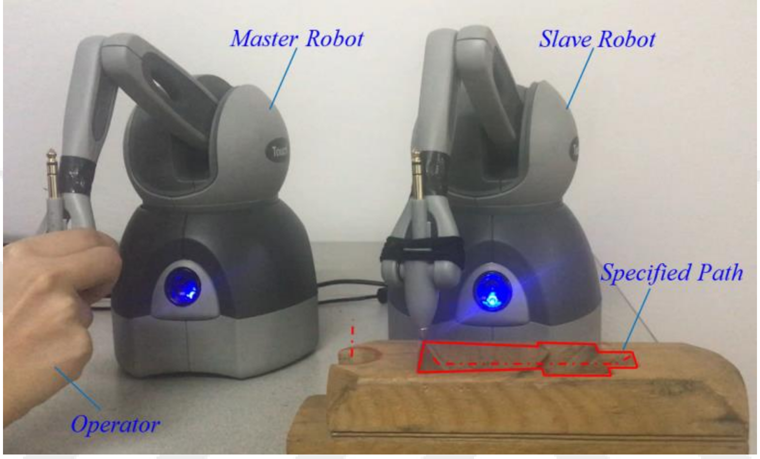

Figure 6.14. Experiment setup to compare RFOB and CTM

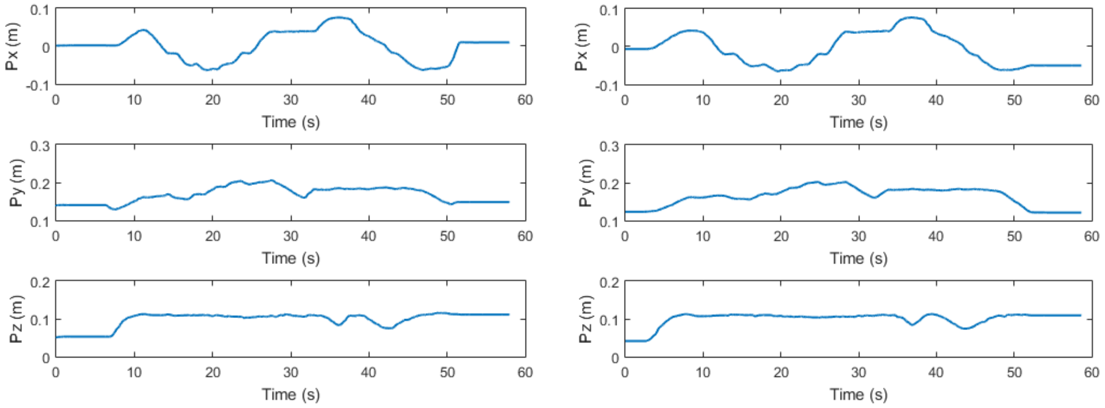

(a) (b)

Figure 6.15. Position response in CS during free-motion (a) CTM (b) NNRFOB

According to the results, although estimated external forces should ideally be zero, they are larger in the experiment done by using CTM than using the proposed method due to the friction and other uncertainties on the robot (Fig.6.16). In the experiment with the proposed method, disturbance observers compensate all effects and the neural network structure already includes them. Thus, it is observed that more accurate results are achieved by NNRFOB according to RMS error results as seen in Table.6.5.

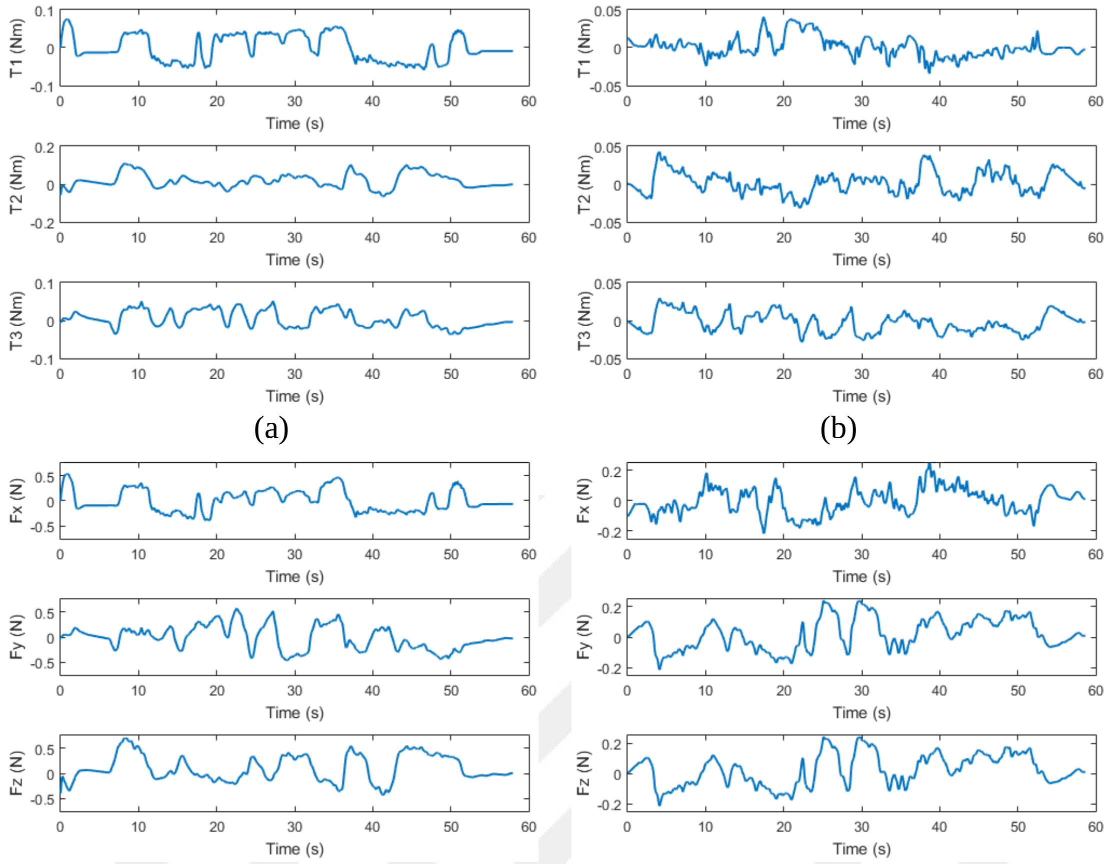

(a) (b)

(c) (d)

Figure 6.16. JS torque and CS force estimations (a,c) CTM (b,d) NNRFOB

Table 6.5. Comparison of RMS errors in experiments with CTM and NNRFOB

	RMS Error in τ_1 (Nm)	**RMS Error in τ_2 (Nm)**	**RMS Error in τ_3 (Nm)**
CTM	0.0352	0.0412	0.0224
NNRFOB	0.0131	0.0146	0.0133
	RMS Error in F_x (N)	**RMS Error in F_y (N)**	**RMS Error in F_z (N)**
CTM	0.2141	0.2327	0.2769
NNRFOB	0.0838	0.1056	0.1190

7. CONCLUSIONS

7.1. Accomplishments and Conclusions

This thesis presented the development of control systems and teleoperation algorithms that will solve the lack of force reflection during teleoperation for robotic minimally invasive surgery. Within this scope, a novel 4-DOF surgical forceps that makes possible the estimation of the forces inside the body has been designed. Alongside the position and velocity kinematics of this forceps, different control methods and force estimation algorithms were developed for this mechanism and their real implementations with experiments were provided.

For position control, 2 kinds of controllers were applied on the wrist mechanism with/out gripper: PID controller with disturbance observer (DOBS) and Sliding Mode Controller (SMC). Although good tracking performance was achieved with PID and DOBS when applying it on the wrist excluding gripper, the chosen controller did not compensate disturbances successfully caused by high nonlinearity and gripper weight and some oscillations occurred during motion at some points when there is a gripper on the wrist. However, SMC achieved good tracking in the sense of RMS error compared to PID with DOBS.

Moreover, because of nonlinear structure of the wrist and mechanical problems caused by manufacturing, a novel force estimation method (NNRFOB) that can overcome nonlinearity, instability, uncertainties, and disturbances was developed. Several experiments including tumor detection and palpation were performed on the manufactured prototype of the wrist mechanism and results validate the efficacy of the wrist and estimation method. Also, force estimation and teleoperation algorithms were extended to the 7-DOF system that enables force feedback in each degree of freedom and provides a surgeon with force feedback in all the degrees of freedom of the human hand. From experiment result, it can be seen that the prototype of 7-DOF surgical robot achieved accurate force estimations on all 6 axes. Force estimation on the gripping axis will be validated using a proper force sensor as a future work.

Bilateral teleoperation studies show that NNRFOB can be applied easily with high tracking and force reflection performances in teleoperations due to its practical structure.

Compared NNRFOB to Computed Torque Method (CTM), it was clear that NNRFOB successfully overcome nonlinearity, friction and uncertainties because the performance of CTM is limited in case of uncertainties and changes in dynamic model and it does not include friction estimation. In conclusion, it can be said that the proposed method can be used in all back-drivable rigid link mechanisms.

7.2. Future Work

Possible future work could include:

- The design of a 4-DOF surgical forceps mechanism can be further miniaturized with some modifications. Also, the wrist part of the forceps mechanism can be redesigned to prevent manufacturing problems, such as gaps on joints caused by wear over time.
- The gripper length can be shortened removing spindle-drive motor to increase motion capability of the forceps inside the body. For this purpose, a new mechanism that enables to transform thrust motion into gripping motion has been designed without using any gripper motor on the wrist. However, this is a novel mechanism and there is no study about its kinematic and dynamic analysis so that they must be derived.
- In force estimation algorithm, online training can be developed instead of offline training to reduce estimation error. Also, it may be more effective in case of non-stationary situations, such as bleeding in surgery since it learns faster and updates the networks depending on the environmental conditions in real time.
- The developed force estimation algorithm can be tested on the control system of Kuka IIWA LBR7 R800 to obtain a fully sensorless surgical system by removing the sensor which measures end-effector forces on it.
- Bilateral teleoperation systems that can guarantee stable operation in the presence of time delay can be developed for a 7-DOF surgical robot by providing a surgeon with force feedback in all the degrees of freedom of the human hand.

REFERENCES

[1] Sang H., Yun J, Monfaredi R., Wilson E., Fooladi H. *"External Force Estimation and Implementation in Robotically Assisted Minimally Invasive Surgery"*. The International Journal of Medical Robotics and Computer Assisted Surgery 13.2, 2017

[2] Arata J., Mitsuishi M., Warisawa S., Hashizume M. *"Development of a Dexterous Minimally- Invasive Surgical System with Augment Force Feedback Capability"*. IEEE/RSJ International Conference on Intelligent Robots and Systems, 2005 (IROS2005)

[3] Takahashi H., Warisawa S., Mitsuishi M., Arata J., Hashizume M. *"Development of High Dexterity Minimally Invasive Surgical System with Augment Force Feedback Capability"*. IEEE/RAS-EMBS International Conference on Biomedical Robotics and Biomechatronics, 2006 (BioRob 2006)

[4] Haidegger T., Benyo B., Kovacs L., Benyo Z. *"Force Sensing and Force Control for Surgical Robots"*. IFAC Symposium on Modelling and Control in Biomedical Systems, 2009

[5] Zhao B., Nelson C. A. *"Sensorless Force Sensing For Minimally Invasive Surgery"*. Journal of Medical Devices, 2015

[6] Kazancides P., Zuhars J., Mittelstadt B., Taylor R. H. *"Force Sensing and Control for a Surgical Robot"*. International Conference on Robotic and Automation, 1992

[7] Okamura A. M. *"Haptic Feedback in Robot-Assisted Minimally Invasive Surgery"*. Current Opinion in Urology, 2009

[8] Okamura A. M. *"Methods for Haptic Feedback in Teleoperated Robot-Assisted Surgery"*. Industrial Robot, 2005

[9] Kuebler B., Seibold U., Hirzinger G. *"Development of Actuated and Sensor Integrated Forceps for Minimally Invasive Surgery"*. The International Journal of Medical Robotics & Computer Assisted Surgery (MRCAS), 2005

[10] Kim U., Lee D. H., Yoon W. J., Hannaford B., Choi H. R. "*Force Sensor Integrated Surgical Forceps for Minimally Invasive Robotic Surgery*". IEEE Transactions on Robotics 31, no. 5 (2015): 1214-1224.

[11] Chan L., Nahdy F. Stirling D. *"Extended Active Observer for Force Estimation and Disturbance Rejection of Robotic Manipulator"*. Robotics and Autonomous Systems, 2013

[12] Lee M. C., Kim C. Y, Yao B., Peine W. J., Member, Song Y. E. *"Reaction Force Estimation of Surgical Robot Instrument Using Perturbation Observer with SMCSPO Algorithm"*. IEEE/ASME International Conference on Advanced Intelligent Mechatronics (AIM), 2010

[13] Tadano K., Kawashima K. *"Development of 4-DOFs Forceps with Force Sensing using Pneumatic Servo System"*. IEEE International Conference on Robotics and Automation, 2006 (ICRA 2006)

[14] Zhao B., Nelson C. A. *"Estimating Tool-Tissue Forces Using a 3-Degree-of-Freedom Robotic Surgical Tool"*. Journal of Mechanisms and Robotics, 2016

[15] Li X. *"Real-Time Prediction of Work Piece Errors for a CNC Turning Center, Part 3. Cutting Force Estimation Using Current Sensors"*. International Journal of Advanced Manufacturing Technology, 2001.

[16] Jeong Y. H., Cho D. W. *"Estimating Cutting Force from Rotating and Stationary Feed Motor Currents on a Milling Machine"*. International Journal of Machine Tools and Manufacture, 2002.

[17] Tholey, G., Pillarisetti, A., Green, W., Desai J. P., 2004*, "Design, Development, and Testing of an Automated Laparoscopic Grasper with 3-D Force Measurement Capability"*. Medical Simulation: International Symposium, 2004 (ISMS 2004)

[18] Bolgar D., Krogh S, Maric F., Silvani N. *"Teleoperation of a Surgical Robot using Force Feedback"*.

[19] Haghighipanah M., Miyasaka M., Hannaford B. "*Utilizing Elasticity of Cable-Driven Surgical Robot to Estimate Cable Tension and External Force*". IEEE Robotics and Automation Letters 2.3 (2017): 1593-1600.

[20] Murakami T., Yu F., Ohnishi K. *"Torque Sensorless Control in Multidegree-of-Freedom Manipulator"*. IEEE Transactions on Industrial Electronics, 1993

[21] Ohnishi K, Shibata M, Murakami T. *"Motion Control for Advanced Mechatronics"*. IEEE/ASME Transactions on Mechatronics, 1996

[22] Sariyildiz E., Ohnishi K. *"A Comparison Study for Force Sensor and Reaction Force Observer based Robust Force Control Systems"*. IEEE 23rd International Symposium on Industrial Electronics, 2014 (ISIE 2014)

[23] Chan L., Naghdy F., Stirling D., Field M. *"Nonlinear Bilateral Teleoperation Using Extended Active Observer for Force Estimation and Disturbance Suppression"*. Robotica, vol.33, (1) pp.61-86, 2014

[24] Mitsantisuk C., Ohishi K., Katsura S. *"Estimation of Action/Reaction Forces for the Bilateral Control Using Kalman Filter"*. IEEE Transactions on Industrial Electronics, 2012

[25] Azimifar F, Hassani K., Saveh A. H., Ghomshe F. T. *"Performance Analysis in Delayed Nonlinear Bilateral Teleoperation Systems by Force Estimation Algorithm"*. Transactions of the Institute of Measurement and Control, 2017

[26] Bazman M., **Yilmaz N**., Tumerdem U. "*Dexterous and Back-Drivable Parallel Robotic Forceps Wrist for Robotic Surgery"*, (2018, March) In Advanced Motion Control (AMC), 2018 IEEE 15th International Workshop on (pp. 153-159), Tokyo, Japan

[27] Alassi A., **Yilmaz N**., Bazman M., Gur B., Tumerdem U. "*Development and Kinematic Analysis of a Redundant, Modular and Backdrivable Laparoscopic Surgery Robot*" (2018, July) In 2018 IEEE/ASME International Conference on Advanced Intelligent Mechatronics (AIM), (pp. 213-219), Auckland, New Zealand

[28] Craig J.J. "*Adaptive Control of Mechanical Manipulators*". Ph.D. Thesis, UMI Dissertation Information Service, Ann Arbor 1986

[29] Schilling R. J. "*Fundametals of Robotics: Analysis and Control*", Prentice-Hall, Upper Saddle River 1989

[30] Sciavicco L., Siciliano B. "*Modeling and Control of Robot Manipulator*", McGraw-Hill, New York 1996

[31] Ang K. H., Chong G., Li Y., "*PID Control System Analysis, Design and Technology*", IEEE Transactions on Control Systems Technology, vol.13, no.4, July 2005

[32] Komada S., Ishida M., Ohnishi K., Hori T. "*Disturbance Observer-Based Motion Control of Direct Drive Motor*s", IEEE Transactions on Energy Conversion, Vol. 6, No. 3, September 1991

[33] Sariyildiz E., Ohnishi K. "*A Guide to Design Disturbance Observer based Motion Control Systems*". In Power Electronics Conference (IPEC-Hiroshima 2014-ECCE-ASIA), 2014 International (pp. 2483-2488). IEEE.

[34] Utkin V. "*Variable Structure Systems with Sliding Modes*", IEEE Transactions on Automatic control 22.2 (1977): 212-222.

[35] Széll K., Korondi P. "*Mathematical Basis of Sliding Mode Control of an Uninterruptible Power Supply*", Acta Polytechnica Hungarica 11.03 (2014): 87-106.

[36] **Yilmaz N.**, Bazman M., Tumerdem U. "*Extermal Force/Torque Estimation on a Dexterous Parallel Robotic Surgical Instrument Wrist"*, (2018, October) In 2018 IEEE/RSJ International Conference on Intelligent Robots and Systems (IROS), (pp.4396-4403), Madrid, Spain

[37] Gidaro S., Buscarini M., Ruiz E., Stark M., Labruzzo A. "*Telelap Alf-X: A Novel Telesurgical System for the 21st Century*", (2012) Surgical technology international, 22, 20-25.

[38] Toğuş F., Kaya C. A. "*Comparison and Development of Bilateral Teleoperation Systems in the Presence of Time Delay*", Undergraduation Project, Marmara University

[39] Farzin Piltan, H. Rezaie, B. Boroomand, Arman Jahed, "*Design Robust Back Stepping Online Tuning Feedback Linearization Control Applied to IC Engine*", International Journal of Advance Science and Technology, 42: 183-204, 2012.

[40] Jahed A., Piltan F., Rezaie H., Boroomand B., "*Design Computed Torque Controller with Parallel Fuzzy Inference System Compensator to Control of Robot Manipulator*", I.J. Information Engineering and Electronic Business, 2013, 3, 66-77

[41] Lawrence DA. "*Stability and Transparency in Bilateral Teleoperation*" IEEE Trans Robot Autom 1993; 9: 624-637.

CURRICULUM VITAE

PERSONAL INFORMATION

Name : Nural YILMAZ
Nationality : Turkish
Date of Birth : January 03, 1993
Place of Birth : Istanbul, Turkey
E-mail : nrlylmz@gmail.com
nural.yilmaz@marun.edu.tr

EDUCATION

June 2016	BSc Faculty of Engineering, Department of Mechanical Engineering Marmara University, Istanbul, Turkey

ACADEMIC EXPERIENCE

Researcher in a TUBITAK Project	*Project Title:* Design and Development of a Robotic Forceps with Force Feedback Capability for Minimally Invasive Surgery
Apr 2016-Sep 2018	*Funding Source:* The Scientific and Technological Research Council of Turkey (TUBİTAK) – 1003 Primary Subjects R&D Funding Program *Project ID:* 115E712
Student Assistant	CSE123- Introduction to Computing (Matlab & C Courses)
Sep 2014-Jun 2016	Marmara University, Istanbul, Turkey Faculty of Engineering, Department of Mechanical Engineering

PUBLICATIONS

- **Yilmaz N.**, Bazman M., Tumerdem U. "*External Force/Torque Estimation on a Dexterous Parallel Robotic Surgical Intrument Wrist*". (2018, October) In 2018 IEEE/RSJ International Conference on Intelligent Robots and Systems (IROS), Madrid, Spain (**DOI:** 10.1109/IROS.2018.8594326)

- Alassi A., **Yilmaz N.**, Bazman M., Gur B., Tumerdem U. "*Development and Kinematic Analysis of a Redundant, Modular and Backdrivable Laparoscopic Surgery Robot*". (2018, July) In 2018 IEEE/ASME International Conference on Advanced Intelligent Mechatronics (AIM), Auckland, New Zealand (**DOI:** 10.1109/AIM.2018.8452712)

- Bazman M., **Yilmaz N.**, Tumerdem U. "*Dexterous and Back-drivable Parallel Robotic Forceps Wrist for Robotic Surgery*". (2018, March) In Advanced Motion Control (AMC), 2018 IEEE 15th International Workshop on (pp. 153-159), Tokyo, Japan (**DOI:** 10.1109/AMC.2019.8371079)